Cours/Lecture Series

1990–1991 ACADEMIC TRAINING PROGRAMME
LECTURE SERIES FOR POSTGRADUATE STUDENTS

QCD and Collider Physics

W. J. Stirling
Departments of Physics and Mathematical Sciences
University of Durham, Durham DH1 3LE, England

ABSTRACT

The lectures will provide an elementary introduction to perturbative QCD. Particular attention will be paid to those aspects of the theory which are particularly relevant for present and future high-energy experiments. The first two lectures will focus on such theoretical issues as the running coupling constant and renormalisation scheme dependence. The remaining lectures will examine in detail the phenomenologicgal aspects of QCD which are relevant for electron-positron, lepton-hadron and hadron-hadron collisions. The course will finish with a discussion of the current status of the theory and a review of precision measurements of the coupling constant.

SIS/H/346

Fermi National Accelerator Laboratory

FERMILAB-Conf-90/164-T

August 14, 1990

QCD and Collider Physics [1]

R. K. Ellis

Fermi National Accelerator Laboratory

P. O. Box 500, Batavia, Illinois 60510, USA

and

W. J. Stirling

Departments of Physics and Mathematical Sciences

University of Durham, Durham DH1 3LE, England

An introduction to perturbative Quantum Chromodynamics and collider physics is given.

[1] Based on lectures given at the CERN and CERN-JINR Schools of Physics.

Operated by Universities Research Association Inc. under contract with the United States Department of Energy

Contents

1. Fundamentals of Perturbative QCD

In this set of lectures we shall describe the use of perturbative methods to investigate the behaviour of strong interactions at short distances. Perturbative methods are applicable because of the property of asymptotic freedom which will be described in the first lecture. Subsequent lectures describe how short distance cross sections are calculated, and how the results of these calculations compare with experiment.

The treatment of perturbative QCD is developed in analogy with perturbative QED, and an understanding of perturbative QED is therefore a prerequisite for this course.

1.1 Lagrangian of QCD

We begin with a brief description of the QCD Lagrangian and the Feynman rules which can be derived from it. This is a practical guide which does little more than introduce notation and certainly does not do justice to the elegant structure of quantum field theory. For more details, the reader is referred to the standard texts [1,2]. Introductions to perturbative QCD can be found in refs.[3,4,5,6,7].

Just as in Quantum Electrodynamics, the perturbative calculation of any process requires the use of Feynman rules describing the interactions of quarks and gluons. The Feynman rules required for a perturbative analysis of QCD can be derived from an effective Lagrangian density which is given by

$$\mathcal{L} = -\frac{1}{4}F^A_{\alpha\beta}F^{\alpha\beta}_A + \sum_{\text{flavours}} \bar{q}_a(i\hat{D} - m)_{ab}q_b + \mathcal{L}_{\text{gauge-fixing}} + \mathcal{L}_{\text{ghost}}. \qquad (1.1)$$

This Lagrangian density describes the interaction of spin-1/2 quarks of mass m and massless spin-1 gluons. $F^A_{\alpha\beta}$ is the field strength tensor derived from the gluon field $\mathcal{A}^A_\alpha$,

$$F^A_{\alpha\beta} = \left[\partial_\alpha \mathcal{A}^A_\beta - \partial_\beta \mathcal{A}^A_\alpha - g f^{ABC}\mathcal{A}^B_\alpha \mathcal{A}^C_\beta\right] \qquad (1.2)$$

and the indices A, B, C run over the eight colour degrees of freedom of the gluon field. It is the third 'non-Abelian' term on the right-hand-side of Eq.(1.2) which distinguishes QCD from QED, giving rise to triplet and quartic gluon self-interactions and ultimately to the property of asymptotic freedom.

The sum over the flavours runs over the n_f different flavours of quarks, g is the coupling constant which determines the strength of the interaction between coloured quanta, and f^{ABC} $(A,B,C = 1,...,8)$ are the structure constants of the $SU(3)$ colour group. The quark fields q_a are in the triplet representation of the colour group, $(a = 1,2,3)$ and D is the covariant derivative. Acting on triplet and octet fields the covariant derivative takes the form

$$(D_\alpha)_{ab} = \partial_\alpha \delta_{ab} + ig\left(t^C \mathcal{A}^C_\alpha\right)_{ab}, \quad (D_\alpha)_{AB} = \partial_\alpha \delta_{AB} + ig(T^C \mathcal{A}^C_\alpha)_{AB}, \tag{1.3}$$

where t and T are matrices in the fundamental and adjoint representations of $SU(3)$ respectively:

$$[t^A, t^B] = if^{ABC}t^C, \;\; [T^A, T^B] = if^{ABC}T^C, \;\; (T^A)_{BC} = -if^{ABC}. \tag{1.4}$$

$\hat{D}$ in Eq.(1.1) is a symbolic notation for $\gamma_\mu D^\mu$ and the spinor indices of γ_μ and q_a have been suppressed. Otherwise we follow the notation of Bjorken and Drell [1] with metric given by $g^{\alpha\beta}$ = diag(1,-1,-1,-1) and set $\hbar = c = 1$. By convention the normalisation of the $SU(N)$ matrices is chosen to be,

$$\mathrm{Tr}\; t^A t^B = T_R\, \delta^{AB}, \;\; T_R = \frac{1}{2}. \tag{1.5}$$

With this choice the $SU(N)$ colour matrices obey the following relations,

$$\sum_A t^A_{ab} t^A_{bc} \;=\; C_F\, \delta_{ac}, \;\; C_F = \frac{N^2-1}{2N} = \frac{4}{3}, \;\; (N=3) \tag{1.6}$$

$$\mathrm{Tr}\; T^C T^D \;=\; \sum_{A,B} f^{ABC} f^{ABD} = C_A\, \delta^{CD}, \;\; C_A = N = 3. \tag{1.7}$$

We cannot perform perturbation theory with the Lagrangian of Eq.(1.1) without the gauge fixing term. It is impossible to define the propagator for the gluon field without making a choice of gauge. The choice,

$$\mathcal{L}_{\mathbf{gauge-fixing}} = -\frac{1}{2\,\lambda}\left(\partial^\alpha \mathcal{A}^A_\alpha\right)^2, \tag{1.8}$$

fixes the class of *covariant gauges* and λ is the gauge parameter. In a non-Abelian theory such as QCD this covariant gauge-fixing term must be supplemented by a ghost Lagrangian, which is given by

$$\mathcal{L}_{\mathbf{ghost}} = \partial_\alpha \eta^{A\,\dagger}\left(D^\alpha_{AB}\eta^B\right). \tag{1.9}$$

Here η^A is a complex scalar field which obeys Fermi statistics. The derivation of the form of the ghost Lagrangian is best provided by the path integral formalism [8] and the procedures due to Fadeev and Popov [9]. The ghost fields cancel unphysical degrees of freedom which would otherwise propagate in covariant gauges. For an explanation of the physical role played by ghost fields, the reader is referred to ref. [10].

1.2 Feynman rules

Eqs.(1.1), (1.8) and (1.9) are sufficient to derive the Feynman rules which should be used in weak coupling perturbation theory in a covariant gauge. The Feynman rules are defined from the action operator $\Phi = i\int \mathcal{L}\, d^4x$ rather than from the Lagrangian density. We can separate the effective lagrangian into a free piece $\mathcal{L}_0$, which normally contains all the terms bilinear in the fields, and an interaction piece, $\mathcal{L}_I$, which contains all the rest:

$$\begin{aligned} \Phi &= \Phi_0 + \Phi_I \\ \Phi_0 &= i\int d^4x \mathcal{L}_0(x), \quad \Phi_I = i\int d^4x \mathcal{L}_I(x). \end{aligned} \tag{1.10}$$

The practical recipe to determine the Feynman rules is that the inverse propagator is derived from $-\Phi_0$, whereas the Feynman rules for the interacting parts of the theory which are treated as perturbations are derived from Φ_I.

This recipe (including the extra minus sign) can be understood [11] by considering the following two different approaches to the quantisation of a theory. For simplicity, consider a theory which contains only a complex scalar field ϕ and an action which contains only bilinear terms, $\Phi = \phi^*(K + K')\phi$. In the first approach, both K and K' are included in the free Lagrangian, $\Phi_0 = \phi^*(K + K')\phi$. Using the above rule the propagator Δ for the ϕ field is given by

$$\Delta = \frac{-1}{K + K'}. \tag{1.11}$$

In the second approach K is regarded as the free Lagrangian, $\Phi_0 = \phi^* K \phi$, and K' as the interaction Lagrangian, $\Phi_I = \phi^* K' \phi$. Now Φ_I is included to all orders in perturbation theory by inserting the interaction term an infinite number of times:

$$\Delta = \frac{-1}{K} + \left(\frac{-1}{K}\right)K'\left(\frac{-1}{K}\right) + \left(\frac{-1}{K}\right)K'\left(\frac{-1}{K}\right)K'\left(\frac{-1}{K}\right) + \cdots = \frac{-1}{K + K'} \tag{1.12}$$

Note that with the choice of signs described above the full propagator of the ϕ field is the same in both approaches, demonstrating the internal consistency of the recipe.

Using the free piece $\mathcal{L}_0$ of the QCD Lagrangian given in Eq.(1.1) one can readily obtain the quark and gluon propagators. Thus, for example, the inverse fermion propagator in momentum space can be obtained by making the identification $\partial^\alpha = -ip^\alpha$ for an incoming field. In momentum space the two point function of the quark field depends on a single momentum p. It is found to be

$$\Gamma^{(2)}_{ab}(p) = -i\delta_{ab}\,(\hat{p} - m), \tag{1.13}$$

which is the inverse of the propagator given in Table 1. The $i\varepsilon$ prescription for the pole of the propagator is added to preserve causality, in exactly the same way as in QED[1]. Similarly the inverse propagator of the gluon field is found to be

$$\Gamma^{(2)}_{\{AB,\,\alpha\beta\}}(p) = i\delta_{AB}\,\left[p^2 g_{\alpha\beta} - (1 - \frac{1}{\lambda})p_\alpha p_\beta\right]. \tag{1.14}$$

It is straightforward to check that without the gauge fixing term this function would have no inverse. The result for the gluon propagator Δ is as given in Table 1:

$$\Gamma^{(2)}_{\{AB,\,\alpha\beta\}}(p)\;\Delta^{(2)\;\{BC,\,\beta\gamma\}}(p) = \delta^C_A g^\gamma_\alpha \tag{1.15}$$

$$\Delta^{(2)}_{\{BC,\,\beta\gamma\}}(p) = \delta_{BC}\frac{i}{p^2}\left[-g_{\beta\gamma} + (1-\lambda)\frac{p_\beta p_\gamma}{p^2}\right]. \tag{1.16}$$

Replacing derivatives with the appropriate momenta, Eqs.(1.1), (1.8) and (1.9) can be used to derive all the rules in Table 1.

1.3 The running coupling constant

In order to introduce the concept of the running coupling, consider as an example a dimensionless physical observable R which depends on a single energy scale Q. By assumption the scale Q is much bigger than all other dimensionful parameters such as masses. We shall therefore set the masses to zero. (This step requires the additional assumption that R has a sensible zero mass limit.) Naive scaling would suggest that because there is a single large scale, R should have a constant value independent of Q. This result is not however true in a renormalisable quantum field theory. When we

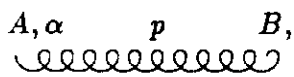	$\delta^{AB}\left[-g^{\alpha\beta}+(1-\lambda)\frac{p^\alpha p^\beta}{p^2+i\epsilon}\right]\frac{i}{p^2+i\epsilon}$
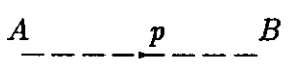	$\delta^{AB}\frac{i}{p^2+i\epsilon}$
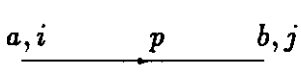	$\delta^{ab}\frac{i}{(\hat{p}-m+i\epsilon)_{ji}}$
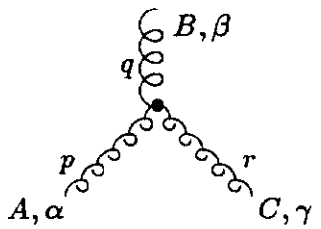	$-gf^{ABC}\left[g^{\alpha\beta}(p-q)^\gamma+g^{\beta\gamma}(q-r)^\alpha+g^{\gamma\alpha}(r-p)^\beta\right]$ (all momenta incoming)
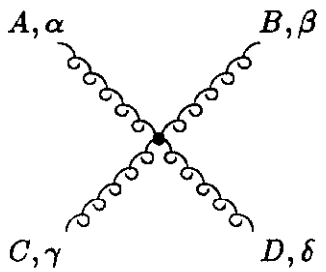	$-ig^2 f^{XAC}f^{XBD}(g_{\alpha\beta}g_{\gamma\delta}-g_{\alpha\delta}g_{\beta\gamma})$ $-ig^2 f^{XAD}f^{XBC}(g_{\alpha\beta}g_{\gamma\delta}-g_{\alpha\gamma}g_{\beta\delta})$ $-ig^2 f^{XAB}f^{XCD}(g_{\alpha\gamma}g_{\beta\delta}-g_{\alpha\delta}g_{\beta\gamma})$
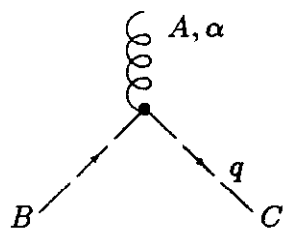	$gf^{ABC}q^\alpha$
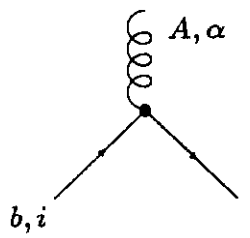	$-ig\left(t^A\right)_{cb}(\gamma^\alpha)_{ji}$

Table 1: Feynman rules for QCD in a covariant gauge

calculate R as a perturbation series in the coupling $\alpha_S = g^2/4\pi$, (defined in analogy with the fine structure constant of QED), the perturbation series requires renormalisation to remove ultra-violet divergences. Because this renormalisation procedure introduces a second mass scale μ – the point at which the subtractions which remove the ultra-violet divergences are performed – R depends in general on the ratio Q/μ and is not therefore constant. It follows also that the renormalised coupling α_S depends on the choice made for the subtraction point μ.

However μ is an arbitrary parameter. The Lagrangian of QCD makes no mention of the scale μ, even though a choice of μ is required to define the theory at the quantum level. Therefore, if we hold the bare coupling fixed, physical quantities such as R cannot depend on the choice made for μ. Since R is dimensionless, it can only depend on the ratio Q^2/μ^2 and the renormalised coupling α_S. Mathematically, the μ dependence of R may be quantified by

$$\mu^2 \frac{d}{d\mu^2} R(\frac{Q^2}{\mu^2}, \alpha_S) \equiv \left[\mu^2 \frac{\partial}{\partial \mu^2} + \mu^2 \frac{\partial \alpha_S}{\partial \mu^2} \frac{\partial}{\partial \alpha_S} \right] R = 0. \tag{1.17}$$

To rewrite this equation in a more compact form we introduce the notations

$$t = \ln(\frac{Q^2}{\mu^2}), \quad \beta(\alpha_S) = \mu^2 \frac{\partial \alpha_S}{\partial \mu^2}, \tag{1.18}$$

and rewrite Eq.(1.17) as

$$\left[-\frac{\partial}{\partial t} + \beta(\alpha_S) \frac{\partial}{\partial \alpha_S} \right] R = 0. \tag{1.19}$$

This first order partial differential equation is solved by implicitly defining a new function – the running coupling $\alpha_S(Q)$ – as follows:

$$t = \int_{\alpha_S}^{\alpha_S(Q)} \frac{dx}{\beta(x)}, \quad \alpha_S(\mu) \equiv \alpha_S. \tag{1.20}$$

By differentiating Eq.(1.20) we can show that

$$\frac{\partial \alpha_S(Q)}{\partial t} = \beta(\alpha_S(Q)), \quad \frac{\partial \alpha_S(Q)}{\partial \alpha_S} = \frac{\beta(\alpha_S(Q))}{\beta(\alpha_S)}. \tag{1.21}$$

and hence that $R(1, \alpha_S(Q))$ is a solution of Eq.(1.19). The above analysis shows that all of the scale dependence in R enters through the running of the coupling constant

$\alpha_S(Q)$. It follows that knowledge of the quantity $R(1,\alpha_S)$, calculated in fixed order perturbation theory, allows us to predict the variation of R with Q if we can solve Eq.(1.20). In the next section, we shall show that QCD is an *asymptotically free* theory. This means that $\alpha_S(Q)$ becomes smaller as the scale Q increases. For sufficiently large Q, therefore, we can always solve Eq.(1.20) using perturbation theory.

1.4 The beta function and the Λ parameter in QCD

The running of the coupling constant α_S is determined by the renormalisation group equation. In QCD, the β function has the perturbative expansion

$$\begin{aligned}\beta(\alpha_S) &= -b\alpha_S^2(1+b'\alpha_S+O(\alpha_S^2))\\ b &= \frac{(33-2n_f)}{12\pi},\quad b' = \frac{(153-19n_f)}{2\pi(33-2n_f)},\end{aligned} \tag{1.22}$$

where n_f is the number of active light flavours. An alternative notation which is sometimes used is

$$\begin{aligned}\beta(\alpha_S) &= -\alpha_S\sum_{n=0}^{\infty}\beta_n\left(\frac{\alpha_S}{4\pi}\right)^{(n+1)}\\ \beta_0 = 4\pi b &= 11-\frac{2}{3}n_f,\quad \beta_1 = 16\pi^2 bb' = 102-\frac{38}{3}n_f,\quad \ldots\end{aligned} \tag{1.23}$$

The β function coefficients can be extracted from the higher order (loop) corrections to the bare vertices of the theory, as in QED. Here we see for the first time the effect of the non-Abelian interactions in QCD. In QED (with one fermion flavour) the β function is

$$\beta_{QED}(\alpha) = \frac{1}{3\pi}\alpha^2+\ldots \tag{1.24}$$

and thus the b coefficients in QED and QCD have the opposite sign.

From Eq.(1.21) we may write,

$$\frac{\partial\alpha_S(Q)}{\partial t} = -b\alpha_S^2(Q)\Big[1+b'\alpha_S(Q)+O(\alpha_S^2(Q))\Big]. \tag{1.25}$$

If both $\alpha_S(\mu)$ and $\alpha_S(Q)$ are in the perturbative region it makes sense to truncate the series on the right-hand-side and solve the resulting differential equation for $\alpha_S(Q)$.

For example, neglecting the b' and higher coefficients in Eq.(1.25) gives the solution

$$\alpha_S(Q) = \frac{\alpha_S(\mu)}{1+\alpha_S(\mu)bt}, \quad t = \ln(\frac{Q^2}{\mu^2}). \tag{1.26}$$

This gives the relation between $\alpha_S(Q)$ and $\alpha_S(\mu)$, if both are in the perturbative region. Evidently as t becomes very large, the running coupling $\alpha_S(Q)$ decreases to zero. This is the property of *asymptotic freedom*. The approach to zero is rather slow since α_S only decreases like an inverse power of $\log Q^2$. Notice that the sign of b is crucial. With the opposite sign of b the coupling would *increase* at large Q^2, as it does in QED.

It is relatively straightforward to show that including the next-to-leading order coefficient b' yields the solution

$$\frac{1}{\alpha_S(Q)} - \frac{1}{\alpha_S(\mu)} + b'\ln\Big(\frac{\alpha_S(Q)}{(1+b'\alpha_S(Q)}\Big) - b'\ln\Big(\frac{\alpha_S(\mu)}{(1+b'\alpha_S(\mu)}\Big) = bt. \tag{1.27}$$

Note that this is now an implicit equation for $\alpha_S(Q)$ as a function of t and $\alpha_S(\mu)$. In practice, given values for these parameters, $\alpha_S(Q)$ can easily be obtained numerically to any desired accuracy.

Returning to the physical quantity R, we can now demonstrate the type of terms which the renormalisation group resums. Assume that in perturbation theory R has the expansion

$$R = \alpha_S + \ldots \tag{1.28}$$

where $\ldots$ represents terms of order α_S^2 and higher. The solution $R(1,\alpha_S(Q))$ – for the special choice of R given by Eq.(1.28) – can be re-expressed in terms of $\alpha_S(\mu)$ using Eq.(1.26):

$$R(1,\alpha_S(Q)) = \alpha_S(\mu)\sum_{j=1}^{\infty}(-1)^j(\alpha_S(\mu)bt)^j = \alpha_S(\mu)\Big[1-\alpha_S(\mu)bt+\alpha_S^2(\mu)(bt)^2+\ldots\Big] \tag{1.29}$$

Thus order by order in perturbation theory there are logarithms of Q^2/μ^2 which are automatically resummed by using the running coupling. Higher order terms in R – represented by the dots in Eq.(1.28) – when expanded give terms with fewer logarithms per power of α_S. An explicit example of how this works in practice will be discussed in the next chapter.

Perturbative QCD tells us how the coupling constant varies with the scale, not the absolute value itself. The latter has to be obtained from experiment. Thus we can choose as 'the' fundamental parameter of the theory the value of the coupling constant at a convenient reference scale which is large enough to be in the perturbative domain, M_Z for example. An alternative approach - which was adopted historically and is now the de facto standard for specifying the strength of the strong interaction – is to introduce a dimensionful parameter directly into the definition of $\alpha_S(Q)$. By convention this parameter is called Λ and is a constant of integration defined by

$$\ln \frac{Q^2}{\Lambda^2} = -\int_{\alpha_S(Q)}^{\infty} \frac{dx}{\beta(x)} = \int_{\alpha_S(Q)}^{\infty} \frac{dx}{bx^2(1+b'x+\ldots)}. \tag{1.30}$$

In effect, Λ represents the scale at which the coupling $\alpha_S(Q)$ becomes strong. The arbitrariness of the integration constant is reflected in the fact that replacing Λ by $\Lambda\times$ constant in Eq.(1.30) still gives a solution to the differential equation for $\alpha_S(Q)$.

The introduction of Λ allows us to write the correct asymptotic solution for α_S. In leading order (LO), i.e. retaining only the b coefficient in the β function, we can perform the integral in Eq.(1.30) to obtain

$$\alpha_S(Q) = \frac{1}{b\ln(Q^2/\Lambda^2)}. \tag{1.31}$$

Note that for large Q this solution agrees with Eq.(1.26) as it must. The definition of Λ is extended to next-to-leading order (NLO) by including also the b' coefficient in the integral:

$$\frac{1}{\alpha_S(Q)} + b'\ln\Big(\frac{b'\alpha_S(Q)}{1+b'\alpha_S(Q)}\Big) = b\ln\Big(\frac{Q^2}{\Lambda^2}\Big). \tag{1.32}$$

Again, this allows a numerical determination of $\alpha_S(Q)$ for a given value of Λ. Alternatively, we can obtain an approximate solution of Eq.(1.32) in terms of inverse powers of $\log(Q^2/\Lambda^2)$:

$$\alpha_S(Q) = \frac{1}{b\ln(Q^2/\Lambda^2)}\left[1 - \frac{b'}{b}\frac{\ln\ln(Q^2/\Lambda^2)}{\ln(Q^2/\Lambda^2)} + \ldots\right]. \tag{1.33}$$

Note, however, that this expression corresponds to a slightly different definition of Λ to Eq.(1.32). The *true* expansion of $\alpha_S(Q)$ in inverse powers of $\log(Q^2/\Lambda^2)$ would contain a term of order constant/$\log^2$. However the freedom to multiply Λ by a constant can be used to remove this term. Specifically, if we call Eqs.(1.32) and

	4 flavours	5 flavours
LO	0.234	0.255
NLO	0.184	0.206

Table 2: $\alpha_S(Q)$ for $Q = 5$ GeV and $\Lambda = 200$ MeV

(1.33) definitions 1 and 2 respectively, then for the *same* value of $\alpha_S(Q)$ the two Λ's are related by

$$\Lambda_1 = \left(\frac{b}{b'}\right)^{\frac{b'}{2b}} \Lambda_2 \equiv 1.148\Lambda_2, \ (n_f = 5). \tag{1.34}$$

It will be clear from the above discussion that the use of the parameter Λ as the fundamental parameter of QCD presents a number of traps which can ensnare the unwary. First, Λ can be defined to leading or next-to-leading order and in each case multiplying Λ by a constant gives an equally acceptable definition. The differences induced in $\alpha_S(Q)$ are one order higher in perturbation theory. Nowadays, all precision QCD phenomenology is performed at next-to-leading order. Either Eq.(1.32) or Eq.(1.33) can be used to define Λ in this case, and both definitions are used in the literature. Since in practice it is usually α_S which is measured experimentally, it is important when comparing Λ values to check that the same equation has been used to determine Λ from the coupling constant. Differences between the results obtained using different conventions – although small – can be comparable to present-day measurement errors.

A second difficulty with the above definitions is that Λ depends on the number of active flavours. Values of Λ for different numbers of flavours are defined by imposing the continuity of α_S at the scale $\mu = m$, where m is the mass of the heavy quark [12]. This is illustrated in Table 2 where the LO and NLO couplings are calculated using Eqs.(1.31) and (1.33) respectively. The correct matching prescription is determined by the conditions that for all values of the momenta the coupling constant must be both a solution of the renormalisation group equation and also a continuous function. From Eq.(1.33) for $\mu > m_b$ we have,

$$\alpha_S(\mu, 5) = \frac{1}{b(5)\ln(\mu^2/\Lambda(5)^2)}\left[1 - \ldots\right]. \tag{1.35}$$

For $m_c < \mu < m_b$, the coupling evolves with four active flavours, and the correct form

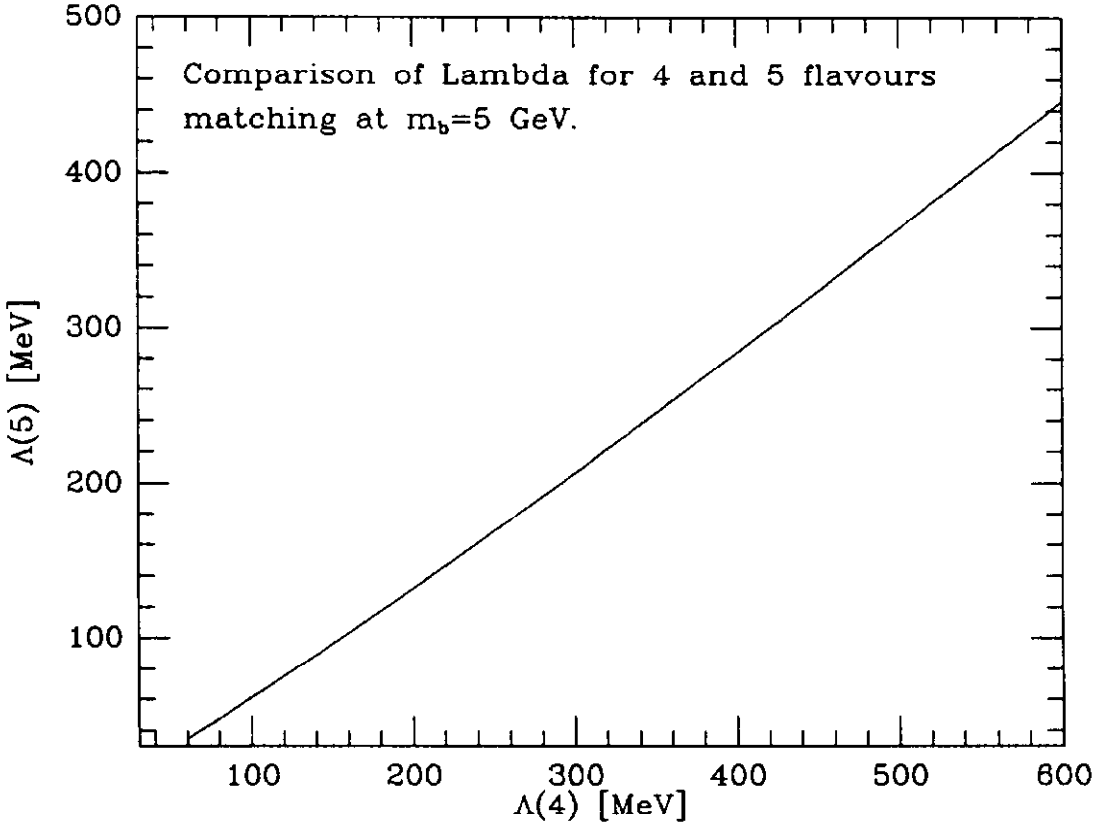

Figure 1: Comparison of Λ for 4 and 5 light quark flavours, with matching at $m_b = 5$ GeV.

to use is

$$\frac{1}{\alpha_S(\mu,4)} = \frac{b(4)\ln(\mu^2/\Lambda(5)^2)}{\left[1-\ldots\right]} + \text{constant} \tag{1.36}$$

where the square bracket is the same as in Eq.(1.35). The constant is fixed by the continuity condition,

$$\alpha_S(m_b,4) = \alpha_S(m_b,5). \tag{1.37}$$

Using the next-to-leading order form for $\alpha_S(Q)$ one can show then that

$$\Lambda(4) \approx \Lambda(5)\left(\frac{m_b}{\Lambda(5)}\right)^{\frac{2}{25}}\left[\ln\left(\frac{m_b^2}{\Lambda(5)^2}\right)\right]^{\frac{963}{14375}}. \tag{1.38}$$

Fig.(1) illustrates the relation between $\Lambda(4)$ and $\Lambda(5)$ graphically. In summary, it is

important when comparing different Λ values to establish the number of light quark flavours assumed and also whether the LO or NLO expressions have been used. This is illustrated in Table 2.

The third troubling property of Λ is that it depends on the renormalisation scheme. Consider two calculations of the renormalised coupling constant which start from the same bare parameters.

$$\alpha_S^A = Z^A \alpha_S^0$$
$$\alpha_S^B = Z^B \alpha_S^0 \tag{1.39}$$

The two schemes start from the same bare coupling α_S^0. The infinite parts of the renormalisation constants Z^A and Z^B must be the same in all orders of perturbation theory. Therefore the two renormalised coupling constants must be related by a finite renormalisation:

$$\alpha_S^B = \alpha_S^A(1 + c_1\alpha_S^A + \ldots). \tag{1.40}$$

Note that the first two coefficients of the β function, b and b', are unchanged by such a transformation. They are therefore independent of the renormalisation scheme. From Eq.(1.30) we see that the two values of Λ are related by,

$$\log \frac{\Lambda^B}{\Lambda^A} = \frac{1}{2}\int_{\alpha_S^A(Q)}^{\alpha_S^B(Q)} \frac{dx}{bx^2(1+\ldots)} = \frac{c_1}{2b}. \tag{1.41}$$

The last equality follows from taking the limit $Q \to \infty$, because the relation must be true for all values of Q^2. Therefore relations between different definitions of Λ are always determined by the one loop calculation which fixes c_1:

$$\Lambda^B = \Lambda^A \exp\frac{c_1}{2b} \tag{1.42}$$

Nowadays, most calculations in fixed order QCD perturbation theory are performed in the *modified minimal subtraction* renormalisation scheme. In this approach, ultraviolet loop divergences are regulated by reducing the number of space-time dimensions to $n < 4$:

$$\frac{\mathrm{d}^4k}{(2\pi)^4} \longrightarrow (\mu)^{2\epsilon}\frac{\mathrm{d}^{4-2\epsilon}k}{(2\pi)^{4-2\epsilon}} \tag{1.43}$$

where $\epsilon = 2 - \frac{n}{2}$. Note that the renormalisation scale μ preserves the dimensions of the couplings and the fields. Loop integrals of the form $\mathrm{d}^nk/[k^2+m^2]^2$ then lead to

poles at $\epsilon = 0$. The *minimal subtraction* renormalisation prescription is to subtract off these poles and to replace the bare coupling by the renormalised coupling $\alpha_S(\mu)$. In practice the poles always appear in the combination

$$\frac{1}{\epsilon} + \ln(4\pi) - \gamma_E, \tag{1.44}$$

(γ_E is Euler's constant) and in the *modified minimal subtraction* scheme these additional constants are subtracted off as well. These two schemes are therefore examples of schemes A and B introduced above, and it is straightforward to show using Eqs.(1.40) and (1.42) that

$$\Lambda^2_{\overline{\rm MS}} = \Lambda^2_{\rm MS} e^{(\ln(4\pi)-\gamma_E)}. \tag{1.45}$$

Lastly, the expression of the experimentally measured coupling α_S in terms of Λ leads to an error which is both exponentially magnified and asymmetric. This is mathematically correct but depressing for an experimenter since most experiments actually measure α_S. A partial compilation of measurements is shown in Fig.(2). The errors in Fig.(2) are too large to conclude that α_S has a logarithmic fall-off with μ, but analysis of jet data in e^+e^- annihilation demonstrates that α_S does decrease with scale (see later).

Guided by Fig.(2), for the phenomenological predictions made in the following lectures we shall assume

$$100 \text{ MeV} < \Lambda_{\overline{\rm MS}}(5) < 250 \text{ MeV}. \tag{1.46}$$

This corresponds to about a 20% uncertainty at the mass of the Z: $0.10 < \alpha_S(M_Z) < 0.12$. Lack of knowledge of α_S directly translates into an uncertainty in the prediction of the size of QCD cross sections. Thus we should expect errors in the prediction of cross sections which begin in order α_S of about 20%.

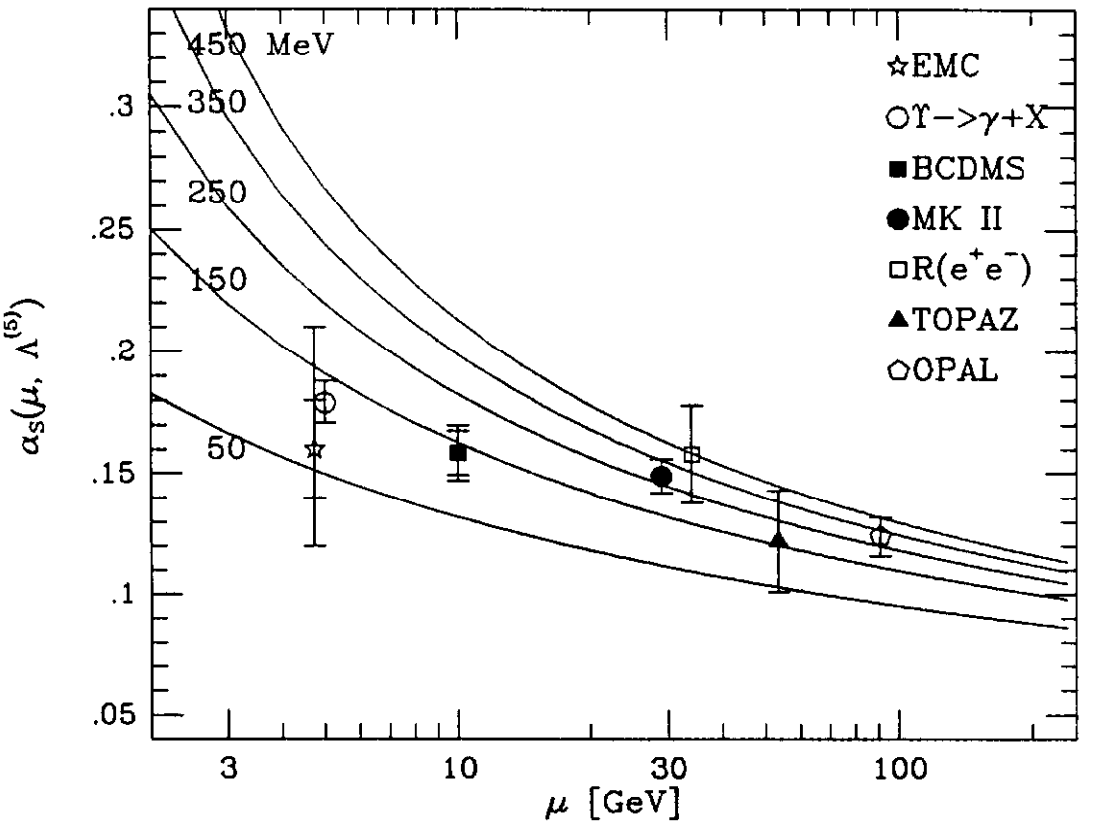

Figure 2: Measurements of α_S compared with predictions for various values of $\Lambda(5)$.

2. QCD in $e^+e^- \to$ Hadrons

Many of the basic ideas and properties of perturbative QCD can be illustrated by considering the process $e^+e^- \to$ hadrons. We begin by discussing the total cross section. We show how the order α_S corrections are calculated, and how renormalisation scheme dependence enters at order α_S^2. The total hadronic cross section also provides one of the most precise measurements of the strong coupling, and we quote the latest experimental results.

Perturbative QCD also predicts a rich 'jet' structure for the final state hadrons. We show how jet cross sections can be defined, and how the predictions compare with experiment. The property of colour coherence is also discussed.

2.1 The total cross section for $e^+e^- \to$ hadrons

One of the theoretically cleanest predictions of perturbative QCD is $R^{e^+e^-}$, the ratio of the total e^+e^- hadronic cross section to the muon pair production cross section. We begin by considering the high energy $2 \to 2$ process $e^+e^- \to f\bar{f}$ with f a light charged fermion, $f \neq e$. In lowest order the process is mediated by either a virtual photon or a Z^0 in the $s-$channel. Denoting the centre-of-mass scattering angle of the final state pair by θ, the differential cross section is:

$$\begin{aligned}\frac{d\sigma}{d\cos\theta} &= \frac{\pi\alpha^2}{2s}\Big[(1+\cos^2\theta)(Q_f^2 - 2Q_f V_e V_f \chi_1(s) + (A_e^2+V_e^2)(A_f^2+V_f^2)\chi_2(s)) \\ &\quad + \cos\theta(-4Q_f A_e A_f \chi_1(s) + 8A_e V_e A_f V_f \chi_2(s))\Big] \qquad (2.1)\end{aligned}$$

where

$$\begin{aligned}\chi_1(s) &= \kappa \frac{s(s-M_Z^2)}{(s-M_Z^2)^2+\Gamma_Z^2 M_Z^2} \\ \chi_2(s) &= \kappa^2 \frac{s^2}{(s-M_Z^2)^2+\Gamma_Z^2 M_Z^2} \\ \kappa &= \left(\frac{\sqrt{2}G_F M_Z^2}{4\pi\alpha}\right) \qquad (2.2)\end{aligned}$$

and (V_f, A_f) are the vector and axial couplings of the fermions to the Z given explicitly in Eq.(6.11). The χ_2 term comes from the square of the Z-exchange amplitude and the

χ_1 term from the photon-Z interference. Now at centre-of-mass scattering energies $\sqrt{s}$ far below the Z peak, the ratio s/M_Z^2 is small and so $1 \gg \chi_1 \gg \chi_2$. This means that the weak effects – manifest in the terms involving the vector and axial couplings – are small and can be neglected. Eq.(2.1) then reduces to

$$\frac{d\sigma}{d\cos\theta} = \frac{\pi\alpha^2 Q_f^2}{2s}(1+\cos^2\theta) \equiv \frac{\pi\alpha^2 Q_f^2}{s}\frac{t^2+u^2}{s^2}. \tag{2.3}$$

The Mandelstam variables are denoted as usual by s, t and u. Integrating over θ and setting $Q_f = -1$ gives the total cross section for $e^+e^- \to \mu^+\mu^-$:

$$\sigma_0 = \frac{4\pi\alpha^2}{3s} \tag{2.4}$$

where $\sqrt{s}$ is the total centre-of-mass energy.

When an electron and a positron annihilate they can also produce hadrons in the final state. Although the formation of the observed final state hadrons is not governed by perturbation theory the total cross section for the production of hadrons can be calculated using perturbative methods. Why would one expect perturbation theory to give an accurate description of the total hadronic production cross section? The answer can be understood by visualising the event in space-time. The electron and positron form a photon of virtuality $Q = \sqrt{s}$ which fluctuates into a quark and an antiquark. By the uncertainty principle this fluctuation occurs in a space time volume $1/Q$, and if Q is large the production rate should be predicted by perturbation theory. Subsequently the quarks and gluons form themselves into hadrons. This happens at a later time characterised by the scale $1/\Lambda$, where Λ is the typical mass scale of the strong interactions. The interactions which change quarks and gluons into hadrons modify the outgoing state, but they occur too late to modify the probability for an event to happen.

In leading order perturbation theory, therefore, the total hadronic cross section is obtained by simply summing over all kinematically accessible flavours and colours of quarks:

$$R^{QPM} = \frac{\sum_q \sigma(e^+e^- \to q\bar{q})}{\sigma(e^+e^- \to \mu^+\mu^-)} = 3\sum_q Q_q^2. \tag{2.5}$$

With $q = u, d, s, c, b$ we obtain $R^{QPM} = 11/3 = 3.67$. At $\sqrt{s} = 34$ GeV the measured value is about 3.9. Even allowing for the Z contribution ($\Delta R_Z \simeq 0.05$), this result

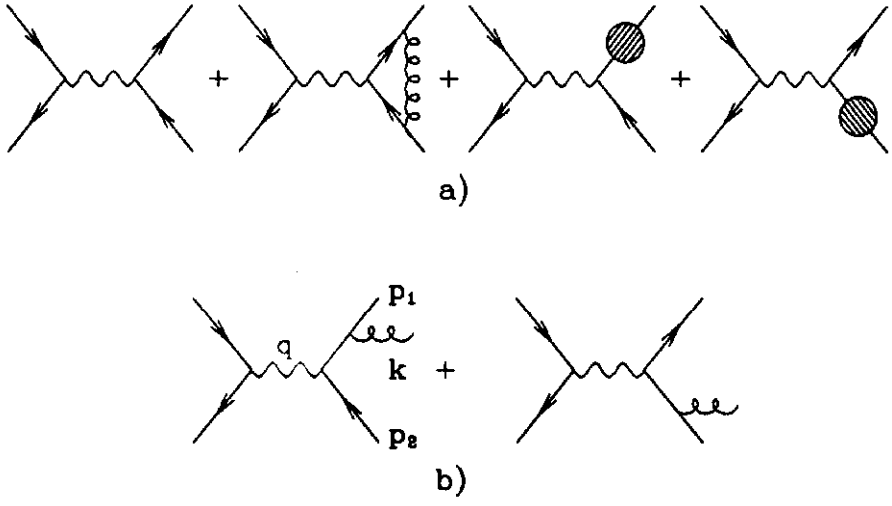

Figure 3: Feynman diagrams for the $O(\alpha_S)$ corrections to the total hadronic cross section in e^+e^- annihilation

is some 5% higher than the lowest order prediction. It turns out that the difference is due to higher order QCD corrections, and in fact the comparison between theory and experiment gives one of the most precise determinations of the strong coupling constant.

The $O(\alpha_S)$ corrections to the total hadronic cross section are calculated from the real and virtual gluon diagrams shown in Fig.(3). For the real gluon emission diagrams shown in Fig.(3b) it is convenient to write the three-body phase space integration as

$$\begin{aligned} d\Phi_3 &= \frac{1}{(2\pi)^5}\frac{d^3p_1}{2E_1}\frac{d^3p_2}{2E_2}\frac{d^3k}{2E_k}\delta^4(q-p_1-p_2-k) \\ &= \frac{s}{2^{10}\pi^5}d\phi_1 d\cos\theta_1 d\phi_{12} dx_1 dx_2 \end{aligned} \tag{2.6}$$

where $\phi_1, \theta_1, \phi_{12}$ are Euler angles, and $x_1 = 2E_1/\sqrt{s}$ and $x_2 = 2E_2/\sqrt{s}$ are the energy fractions of the final state quark and antiquark. Integrating out the Euler angles gives a matrix element which depends only on x_1 and x_2 and the contribution to the total cross section is

$$\sigma^{q\bar{q}g} = \sigma_0 \, 3 \sum_q Q_q^2 \int dx_1 dx_2 \, \frac{2\alpha_S}{3\pi} \, \frac{x_1^2 + x_2^2}{(1-x_1)(1-x_2)} \tag{2.7}$$

where the integration region is: $0 \leq x_1, x_2 \leq 1$, $x_1 + x_2 \geq 1$. Unfortunately, we see that the integrals are divergent at $x_i = 1$. These singularities come from regions of phase space where the gluon is *collinear* with either quark, $\theta_{qg} \to 0$, or where the gluon is *soft*, $E_g \to 0$. Evidently we require some sort of regularisation procedure – to render the integrals finite – before the calculation can be completed. A variety of methods are suitable. One can give the gluon a small mass, or take the final state quark and antiquark off-mass-shell by a small amount. In each case the singularities are then manifest as logarithms of the regulating mass.

A more elegant procedure is to use dimensional regularisation, with the number of space-time dimensions now $n > 4$. With the three-body phase space integrals now cast in n dimensions, the soft and collinear singularities appear as *poles* at $n = 4$. Details of how the calculation proceeds can be found for example in ref.[4]. The result is that the cross section of Eq.(2.7) becomes

$$\sigma^{q\bar{q}g} = \sigma_0 \, 3 \sum_q Q_q^2 \, \frac{2\alpha_S}{3\pi} \, H(\epsilon) \left[\frac{2}{\epsilon^2} - \frac{3}{\epsilon} + \frac{19}{2} + O(\epsilon) \right], \tag{2.8}$$

where $H(\epsilon) = 1 + O(\epsilon)$.

The virtual gluon contributions shown in Fig.(3a) can be calculated in a similar fashion, with dimensional regularisation again used to render finite the infra-red divergences in the loops. The result is

$$\sigma^{q\bar{q}(g)} = \sigma_0 \, 3 \sum_q Q_q^2 \, \frac{2\alpha_S}{3\pi} \, H(\epsilon) \left[-\frac{2}{\epsilon^2} + \frac{3}{\epsilon} - 8 + O(\epsilon) \right]. \tag{2.9}$$

When the two contributions Eqs.(2.8) and (2.9) are added together the poles exactly cancel and the result is *finite* in the limit $\epsilon \to 0$:

$$R^{e^+e^-} = 3 \sum_q Q_q^2 \left\{ 1 + \frac{\alpha_S}{\pi} + O(\alpha_S^2) \right\}. \tag{2.10}$$

Note that the next-to-leading order correction is positive, and with a value for α_S of about 0.15, can accommodate the experimental measurement at $\sqrt{s} = 34$ GeV. In contrast, the corresponding correction is negative for a scalar gluon.

The cancellation of the soft and collinear singularities between the real and virtual gluon diagrams is not accidental. Indeed there are theorems – the Bloch, Nordsieck [13] and Kinoshita, Lee, Nauenberg [14] theorems – which state that suitably defined inclusive quantities will be free of singularities in the massless limit. The total hadronic cross section is an example of such a quantity, whereas the cross section for the exclusive $q\bar{q}$ final state, i.e. $\sigma(e^+e^- \to q\bar{q})$ is not.

The $O(\alpha_S^2)$ corrections to $R^{e^+e^-}$ are also known. At this order we encounter the ultra-violet divergences associated with the renormalisation of the strong coupling. After renormalisation, in the $\overline{MS}$ scheme for example, the $O(\alpha_S^2)$ coefficient depends on the renormalisation scale μ:

$$\begin{aligned} R^{e^+e^-} &= 3\sum_q Q_q^2 \left\{1 + \frac{\alpha_S(\mu)}{\pi} + \left[\frac{33-2n_f}{12}\ln\frac{\mu^2}{s} + \frac{365}{24}\right.\right. \\ &- \left.\left. 11\zeta(3) + (\frac{2}{3}\zeta(3) - \frac{11}{12})n_f\right]\left(\frac{\alpha_S(\mu)}{\pi}\right)^2 + \ldots\right\}, \end{aligned} \tag{2.11}$$

and $\zeta(3) = 1.2021$. Note that the μ-dependence of the second order coefficient is exactly as specified by the renormalisation group equation, i.e. the coefficient of $\ln(\mu^2/s)$ is exactly $b\pi$, where b is the β function coefficient defined in Eq.(1.22). Specialising to the case of $\mu = \sqrt{s}$ and $n_f = 5$, Eq.(2.11) becomes

$$R^{e^+e^-} = 3\sum_q Q_q^2 \left\{1 + \frac{\alpha_S(\sqrt{s})}{\pi} + 1.411\left(\frac{\alpha_S(\sqrt{s})}{\pi}\right)^2 + \ldots\right\}. \tag{2.12}$$

What can one say of the higher order terms in this perturbation series? Before performing an explicit calculation all we can say is that they will be of $O(\alpha_S^3)$. A calculation of the third order coefficient in this perturbation series has been performed [15], but the results are now known to be in error [16].

In general the coefficients of any QCD perturbative expansion depend on the choice made for the renormalisation scale μ. As μ is varied, the change in the coefficients exactly compensates the change in the coupling $\alpha_S(\mu)$ in such a way that the physical predictions are independent of μ. However this μ-independence breaks down whenever

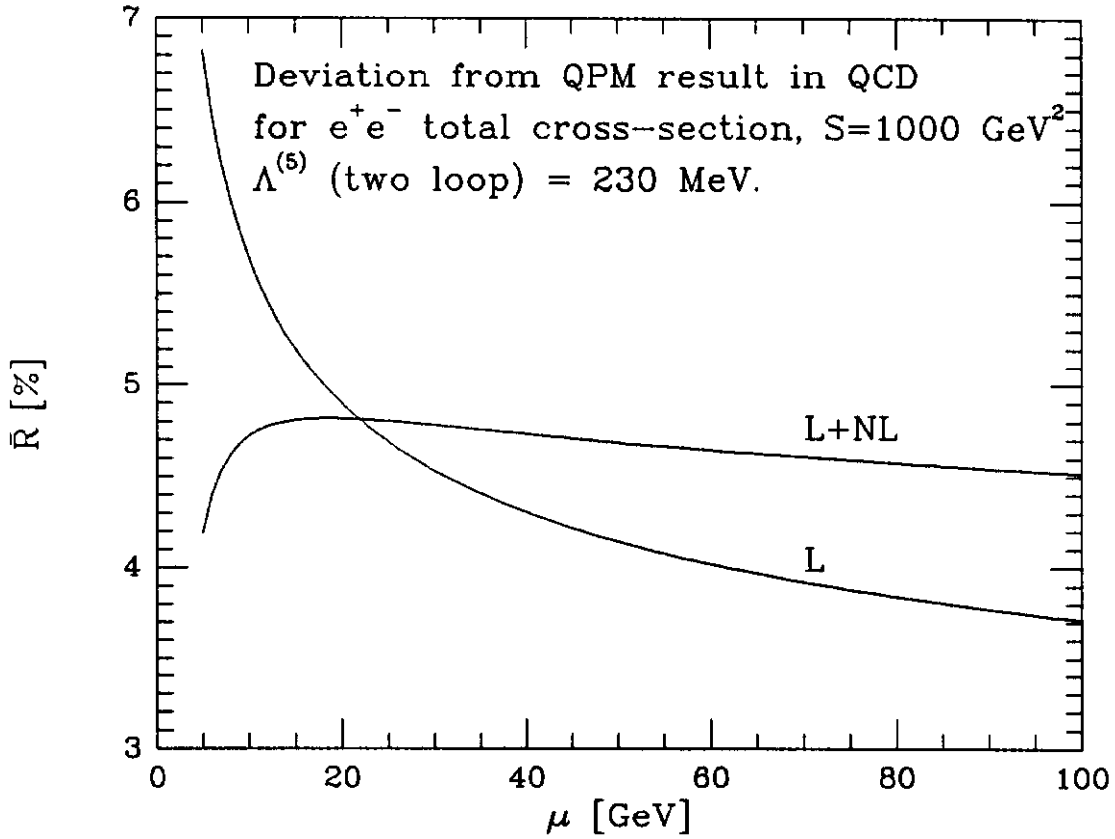

Figure 4: The quantity $\overline{R} = [R^{(j)}/R^{\rm QPM} - 1]$ as a function of the scale μ, where $R^{(j)}$ denotes the QCD prediction for $R^{e^+e^-}$ truncated at $O(\alpha_S^j)$

the series is *truncated*. One can show in fact that changing the scale in a physical quantity such as $R^{e^+e^-}$ – which has been calculated to $O(\alpha_S^n)$ – induces changes of $O(\alpha_S^{n+1})$.

The dependence of $R^{e^+e^-}$ on the scale μ retaining only the first or second terms is shown in Fig.4. As expected, the inclusion of higher order terms leads to a more definite prediction. In the absence of higher order corrections, one can try to guess the 'best' choice of scale, defined as the scale which makes the truncated and all-orders predictions equal. In the literature, two such choices have been advocated in particular. In the *fastest apparent convergence* approach [17], one chooses the scale

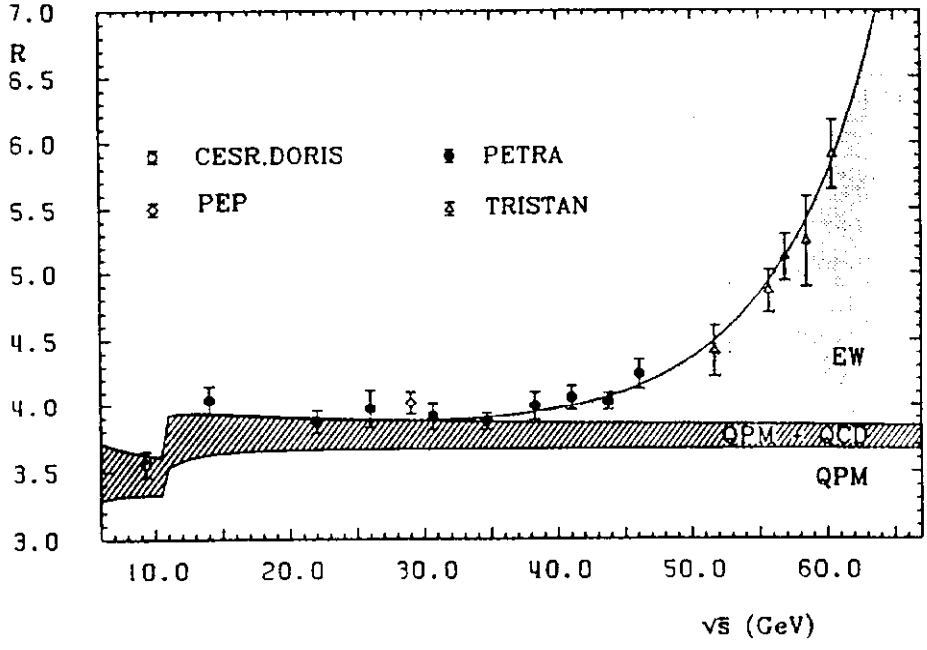

Figure 5: Combined QCD-electroweak fit to $R^{e^+e^-}$, from reference[19]

$\mu = \mu_{FAC}$, where

$$R^{(1)}(\mu_{FAC}) = R^{(2)}(\mu_{FAC}). \tag{2.13}$$

On the other hand, the *principle of minimal sensitivity* [18] suggests a scale choice $\mu = \mu_{PMS}$, where

$$\mu \frac{d}{d\mu} R^{(2)}(\mu)\Big|_{\mu_{PMS}} = 0. \tag{2.14}$$

These two special scales can be identified in Fig.4. It is important to remember that there are no theorems that prove that any of these schemes are correct. All one can say is that the theoretical error on a quantity calculated to $O(\alpha_S^n)$ is $O(\alpha_S^{n+1})$. Varying the scale is simply one way of quantifying this uncertainty.

Finally, Fig.5 shows a recent fit [19] to data on $R^{e^+e^-}$ over a broad energy range. The weak and QCD contributions are displayed. The fitted value of α_S, in the $\overline{MS}$ scheme and using the second order QCD prediction, is

$$\alpha_S(34 \text{ GeV}) = 0.158 \pm 0.020 \tag{2.15}$$

which corresponds to

$$\Lambda_{\overline{MS}}^{(5)} = 440 \, ^{+320}_{-220} \text{ MeV}. \tag{2.16}$$

2.2 Jet cross sections

The expression given for the total hadronic cross section in the previous section is very concise, but it tells us nothing about the kinematic *distribution* of hadrons in the final state. If the hadronic fragments of a fast moving quark have limited transverse momentum relative to the quark momentum, then the lowest order contribution, $(e^+e^- \to q\bar{q})$, can naively be interpreted as the production of two back-to-back jets. In this section we investigate how higher order perturbative corrections modify this picture.

Consider first the next-to-leading process $e^+e^- \to q\bar{q}g$. From Eq.(2.7) in the previous section, we have

$$\frac{1}{\sigma}\frac{d^2\sigma}{dx_1 dx_2} = \frac{2\alpha_S}{3\pi}\frac{x_1^2 + x_2^2}{(1-x_1)(1-x_2)}. \tag{2.17}$$

Recall that the cross section becomes infinitely large when either (a) the gluon is collinear with one of the outgoing quarks, or (b) the gluon momentum goes to zero. This corresponds to (a) only one and (b) both of the x_i approaching 1 respectively. In other words the gluon prefers to be soft and/or collinear with the quarks. If the gluon is *required* to be well-separated in phase space from the quarks – a configuration corresponding to a 'three jet event' – then the cross section is suppressed relative to lowest order by one power of α_S. It would appear, therefore, that the two jet nature of the final state is maintained to next-to-leading order, since both the preferred configurations give a final state indistinguishable (after parton fragmentation to hadrons) from that at lowest order. This qualitative result holds in fact to *all* orders of perturbation theory. Multigluon emission leads to a final state which is predominantly 'two-jet-like', with a smaller probability (determined by α_S) for three or more distinguishable jets. A more complete discussion can be found in reference [20].

To quantify this statement we need to introduce the concept of a *jet measure*, i.e. a procedure for classifying a final state of hadrons (experimentally) or quarks and gluons

(theoretically) according to the number of jets. To be useful, a jet measure should be free of soft and collinear singularities when calculated in perturbative QCD, and should also be relatively insensitive to the non-perturbative fragmentation of quarks and gluons into hadrons.

One of the most widely used jet measures is the 'minimum invariant mass' algorithm. Consider a $q\bar{q}g$ final state. A three jet event is defined as one in which the invariant masses of the parton pairs are all larger than some fixed fraction y of the overall centre-of-mass energy:

$$(p_i + p_j)^2 > ys, \qquad i,j = q,\bar{q},g. \tag{2.18}$$

It is immediately clear that this region of phase space avoids the soft and collinear singularities of the matrix element. In fact in terms of the energy fractions, Eq.(2.18) is equivalent to

$$0 < x_1, x_2 < 1-y, \qquad x_1 + x_2 > 1 + y. \tag{2.19}$$

If we define R_2 and R_3 to be the two and three jet fractions then to $O(\alpha_S)$ we obtain

$$\begin{aligned} R_3 &= \frac{2\alpha_S}{3\pi}\left[(3-6y)\ln\left(\frac{y}{1-2y}\right) + 2\ln^2\left(\frac{y}{1-y}\right) + \frac{5}{2} - 6y - \frac{9}{2}y^2\right. \\ &+ \left. 4\mathrm{Li}_2\left(\frac{y}{1-y}\right) - \frac{\pi^2}{3}\right], \quad \mathrm{Li}_2(y) = -\int_0^y \frac{dz}{1-z}\ln(z). \\ R_2 &= 1 - R_3 \end{aligned} \tag{2.20}$$

Note that the soft and collinear singularities reappear as large logarithms in the limit $y \to 0$. Clearly the result only makes sense for y values large enough such that $R_2 \gg R_3$, so that the $O(\alpha_S)$ correction to R_2 is perturbatively small.

The generalisation to multi-jet fractions is straightforward. Starting from an n-parton final state, identify the pair with the lowest invariant mass squared. If this is greater than ys then the number of jets is n. If not, combine the lowest pair into a single 'cluster'. Then repeat for the $(n-1)$-parton/cluster final state, and so on until all parton/clusters have a relative invariant mass squared greater than ys. The number of clusters remaining is then by definition the number of jets in the final state. Note that an n-parton final state can give any number of jets between n (all

partons well-separated) and 2 (for example, two hard quarks accompanied by soft and collinear gluons).

Since a soft or collinear gluon emitted from a quark line does not change the multiplicity of jets, the cancellation of soft and collinear singularities that was evident in the total cross section calculation can still take place, and the jet fractions defined this way are free of such singularities to all orders in perturbation theory.

Now in general we have

$$R_{i+2}(\sqrt{s},y) = \left(\frac{\alpha_S(\sqrt{s})}{\pi}\right)^i \sum_{j=0}^{\infty} C_{ij}(y)\left(\frac{\alpha_S(\sqrt{s})}{\pi}\right)^j, \quad i \geq 0,$$

$$\sum_{n=2}^{\infty} R_n = 1. \tag{2.21}$$

Note that since the jet fraction criterion y is dimensionless all the energy dependence of the jet fractions is contained in the coupling $\alpha_S(\sqrt{s})$. One can therefore exhibit, at least in principle, the *running* of the strong coupling by measuring a decrease in R_3 as $\sqrt{s}$ increases. The effect is clearly visible in Fig.(6). Note that experimentally the algorithm is applied to final state *hadrons* rather than *partons*. However studies using parton shower/fragmentation Monte Carlos have shown that – at least at high energy – the fragmentation corrections are small and therefore the QCD parton-level predictions can be reliably compared with the experimental data [21]. An example of such a comparison is shown in Fig.(7).

2.3 Colour coherence

For the case of three jet events in e^+e^- annihilation the coherence of the radiation from the hard partons leads to the *string effect* [23,24]. In the language of perturbative QCD, the string effect is a result of constructive and destructive interference. Of course, it is entirely unremarkable that such interference effects should be observed in quantum field theory. However, it is interesting to note that the experimental evidence indicates that such interference effects survive the hadronisation process, a phenomenon which the authors of ref.[24] call *local parton-hadron duality*.

At sufficiently high energy, the colour structure of the hard final state partons will determine the pattern of associated radiation. Because the distribution of this radia-

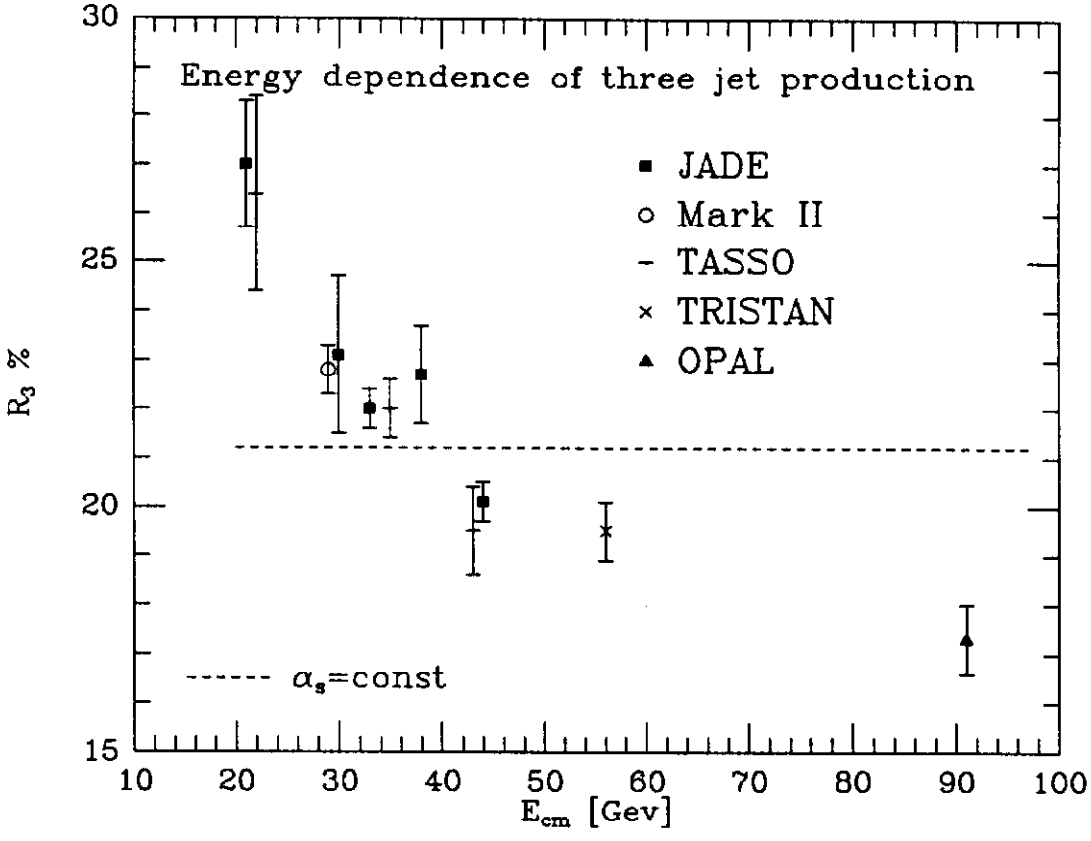

Figure 6: The energy dependence of three jet production[22]

tion is not significantly altered by hadronisation the observed pattern of the hadrons which lie between the jets will depend on the colour of the partons participating in the hard scatter.

We illustrate the derivation of the angle ordered approximation in the process $e^+e^- \rightarrow q\bar{q}g$. Soft gluons are emitted only inside certain angular regions around the directions of the hard partons q, $\bar{q}$ and g. We introduce the angular variables $\zeta_i = 1 - \cos\theta_i$, where θ_i is the angle between the soft gluon and the hard parton i, and $\zeta_{ij} = 1 - \cos\theta_{ij}$ where θ_{ij} is the angle between hard partons i and j. In terms of these variables the eikonal factor which describes the emission of soft radiation may be written,

$$[ij] = g^2 \frac{p_i.p_j}{p_i.k k.p_j} = \frac{g^2}{|k|^2} \frac{\zeta_{ij}}{\zeta_i \zeta_j} = \left(\frac{g^2}{2|k|^2}\left\{\frac{\zeta_{ij}}{\zeta_i\zeta_j} + \frac{1}{\zeta_i} - \frac{1}{\zeta_j}\right\}\right) + \left(i \leftrightarrow j\right) \qquad (2.22)$$

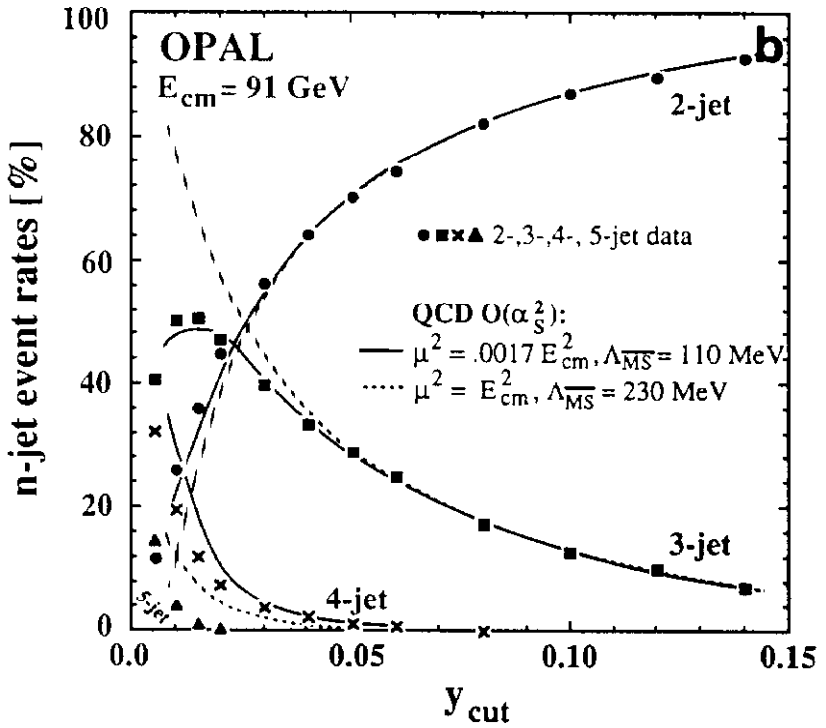

Figure 7: Jet fractions from the OPAL collaboration at LEP [22]. Perturbative QCD fits with different choices for the renormalisation scale μ are shown

where $|k|$ represents the energy of the soft gluon. The lines i and j are colour connected. The eikonal factor in Eq.(2.22) is the same as the factor obtained in the soft photon approximation in QED[1]. The expression in braces contains the collinear pole at $\zeta_i = 0$ but not that at $\zeta_j = 0$. Furthermore, when averaged over the azimuthal angle ϕ_i around the direction of hard parton i, it vanishes outside the cone $\zeta_i = \zeta_{ij}$. In fact [25,24],

$$\int \frac{d\phi_i}{2\pi} \left\{ \frac{\zeta_{ij}}{\zeta_i \zeta_j} + \frac{1}{\zeta_i} - \frac{1}{\zeta_j} \right\} = \frac{2}{\zeta_i} \Theta(\zeta_{ij} - \zeta_i). \tag{2.23}$$

Hence, averaging each term with respect to azimuth around its direction of singularity, we may write,

$$[ij] = \frac{g^2}{|k|^2 \zeta_i} \Theta(\zeta_{ij} - \zeta_i) + \frac{g^2}{|k|^2 \zeta_j} \Theta(\zeta_{ij} - \zeta_j). \tag{2.24}$$

Eq.(2.24) has the same form as the incoherent radiation emission result but with a dynamically imposed angular constraint on the phase space.

An elegant way to examine the pattern of soft radiation associated with a hard scattering event is to compare e^+e^- annihilation into three jets with annihilation into

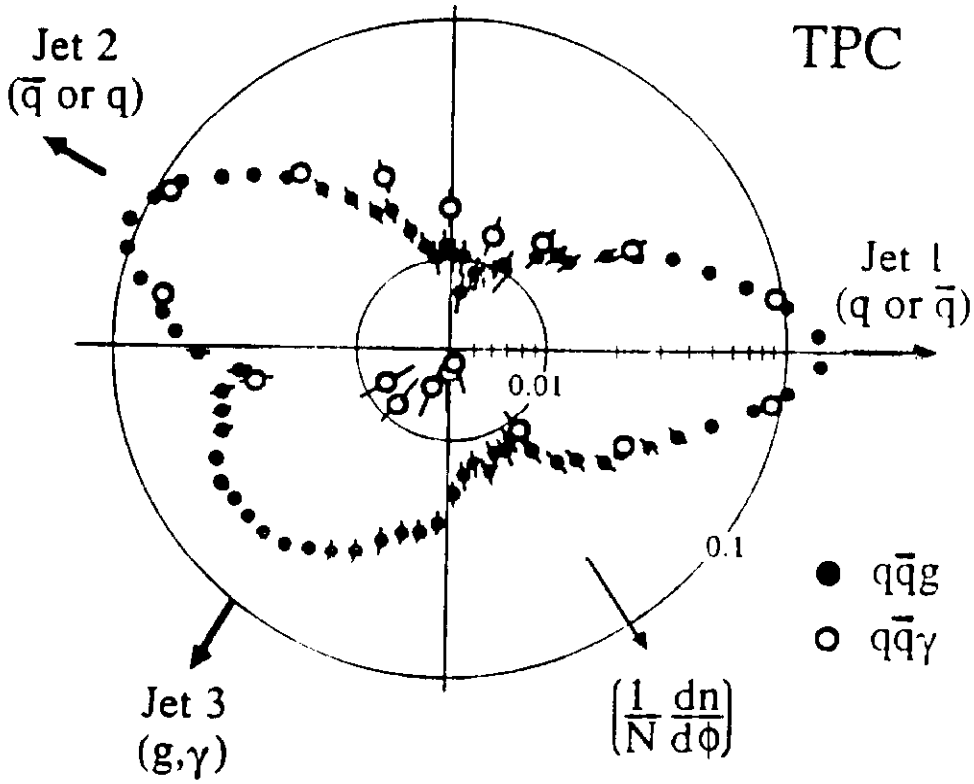

Figure 8: Particle flow as a function of angle in the plane of the event

two jets and a photon. The parton final states are $q\bar{q}g$ and $q\bar{q}\gamma$. From Eq.(2.24) we deduce that the soft radiation (and hence the particle flow) is dynamically constrained by angular ordering to lie between the colour connected lines. For the purposes of this argument the colour degrees of freedom of the gluon can be approximately regarded as a $q\bar{q}$ system, with the quark part connected to the outgoing antiquark line and the antiquark part connected to the outgoing quark line. The soft radiation in the $q\bar{q}g$ event is then expected to lie predominantly between the gluon and the quark and the gluon and the antiquark. In contrast for the $q\bar{q}\gamma$ event the radiation occurs predominantly between the quark and the antiquark. Data from the TPC collaboration [27] are shown in Fig.(8). The jets are ordered in energy $E_1 > E_2 > E_3$ and the third jet is assumed to be the gluon. In the angular regions near the cores of jets 1 and 2, the distributions of the $q\bar{q}g$ and $q\bar{q}\gamma$ events agree very well. In the region between jets 1 and 2, opposite the gluon jet or the photon, the data show a

depletion in particle production in $q\bar{q}g$ compared to $q\bar{q}\gamma$.

A heuristic explanation of the reason for angular ordering can be obtained [26] using a simple uncertainty principle argument. Consider an incoming virtual photon which decays into an electron-positron pair. An additional soft photon of momentum k is subsequently radiated from the electron-positron pair. The virtual state consisting of an electron and a positron differs in energy from the final state containing an electron, a positron and a soft photon by an energy ΔE,

$$\begin{aligned} \Delta E &= (E_i + E_j + E_k) - (E_{i+k} + E_j) \\ &= \sqrt{|\vec{p}_i|^2 + m^2} + |\vec{k}| - \sqrt{\left(\vec{p}_i + \vec{k}\right)^2 + m^2}. \end{aligned} \tag{2.25}$$

In the limit of very large $\vec{p}_i$ and small θ_{ik} this becomes,

$$\Delta E \sim |\vec{k}|\theta_{ik}^2. \tag{2.26}$$

By the uncertainty principle the virtual electron state lives for a time Δt which is approximately given by

$$\Delta t \sim \frac{1}{|\vec{k}|\theta_{ik}^2} \sim \frac{\lambda_T}{\theta_{ik}}, \tag{2.27}$$

where $\lambda_T \sim 1/k_T \sim 1/(k\theta_{ik})$ is the transverse wavelength of the emitted soft photon. In this interval of time Δt the electron and positron separate a transverse distance given by

$$\Delta d = \Delta t \theta_{ij} = \frac{\lambda_T \theta_{ij}}{\theta_{ik}}. \tag{2.28}$$

If $\theta_{ik} > \theta_{ij}$, the separation of the electron and positron is less than the transverse wavelength of the emitted soft photon. The emitted soft photon perceives the electron-positron pair as an unresolved charge neutral object and no radiation occurs. If, on the other hand, the emitted photon lies within the cone described by the electron positron pair, $\theta_{ik} < \theta_{ij}$, the radiation is uninhibited.

This example indicates the reason for angular ordering in QED. The generalisation of this argument to QCD is complicated by the fact that the gluons themselves carry colour charge, but the angular ordering result persists.

It is an interesting property of the theory that the emission of gluons in the final state can, to a good approximation, be represented by a semi-classical parton

'branching' or 'cascade' picture, i.e. the quarks emit gluons which in turn emit more gluons etc. This property is evident for example in Eq.(2.24) where it is shown that the eikonal factor obtained from the interference of Feynman diagrams can be approximately represented as a sum of probabilities. The quarks produced at the photon vertex after an e^+e^- annihilation have 'virtuality' (i.e. are off mass shell) of the order of the total centre-of-mass energy. Parton branching then takes place, reducing the virtualities, until all the final state partons have virtualities of the order of the hadronic mass scale ($O(1$ GeV)). This part of the fragmentation can be described in terms of QCD perturbation theory. Finally, the partons 'hadronise' to give final states made up of pions, kaons and other hadrons. The hadronisation of the partons cannot be described perturbatively, but instead can be *modelled*, the parameters being determined by fitting to the data. In this way jet fragmentation Monte Carlos are constructed. Different ways of performing the non-perturbative hadronisation lead to different models [28] which can be compared with experimental data.

3. Deep Inelastic Scattering and Parton Distributions

The original, and still the most powerful, test of perturbative QCD is the breaking of Bjorken scaling in deep inelastic lepton-hadron scattering. Nowadays, deep inelastic structure function analyses not only provide some of the most precise tests of the theory but also determine the momentum distributions of partons in hadrons for use as input in predicting cross sections in high energy hadron collisions. In this lecture we begin by discussing deep inelastic scattering and the 'naive' parton model. We then show how QCD modifies the simple Bjorken scaling property of the parton model, and discuss how these 'scaling violations' can be calculated in perturbation theory. We compare the theoretical predictions with experimental data, and calculate the asymptotic behaviour of the parton distributions at small x. Finally, we describe the generalisation of the parton picture for general hard scattering processes involving quarks and gluons.

3.1 Deep inelastic scattering and the parton model

Consider the scattering of a high energy charged lepton off a hadron target. If we label the incoming and outgoing lepton four-momenta by k^μ and k'^μ respectively, the momentum of the target hadron (assumed hereafter to be a proton) by p^μ and the momentum transfer by $q^\mu = k^\mu - k'^\mu$, then the standard deep inelastic variables are defined by:

$$\begin{aligned} Q^2 &= -q^2, \qquad p^2 = M^2 \\ x &= \frac{Q^2}{2p\cdot q} = \frac{Q^2}{2M(E-E')} \\ y &= \frac{q\cdot p}{k\cdot p} = 1 - E'/E \ , \end{aligned} \tag{3.1}$$

where the energy variables refer to the target rest frame. If the lepton is an electron or muon, then the scattering is mediated by the exchange of a virtual photon, Fig.(9).

The *structure functions* $F_i(x,Q^2)$ – which parametrise the structure of the target as 'seen' by the virtual photon – are then defined in terms of the lepton scattering

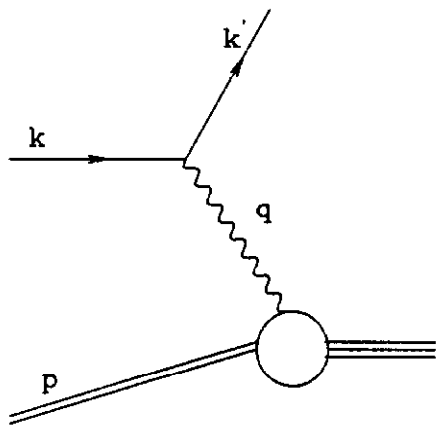

Figure 9: Deep inelastic charged lepton-proton scattering

cross sections. For charged lepton scattering, $lp \to lX$,

$$\frac{d^2\sigma^{em}}{dxdy} = \frac{8\pi\alpha^2 ME}{Q^4}\left[\left(\frac{1+(1-y)^2}{2}\right)2xF_1^{em} + (1-y)(F_2^{em} - 2xF_1^{em}) - (M/2E)xyF_2^{em}\right], \tag{3.2}$$

and for neutrino (antineutrino) scattering, $\nu p \to lX$,

$$\frac{d^2\sigma^{\nu(\bar{\nu})}}{dxdy} = \frac{G_F^2 ME}{\pi}\left[(1-y-\frac{M}{2E}xy)F_2^{\nu(\bar{\nu})} + y^2xF_1^{\nu(\bar{\nu})} + (-)\, y(1-y/2)xF_3^{\nu(\bar{\nu})}\right]. \tag{3.3}$$

The *Bjorken limit* is defined as $Q^2, p\cdot q \to \infty$ with x fixed. In this limit the structure functions obey an approximate *scaling* law, i.e. they depend only on the dimensionless variable x:

$$F_i(x,Q^2) \longrightarrow F_i(x). \tag{3.4}$$

This is illustrated in Fig.(10), where data on the electromagnetic structure function

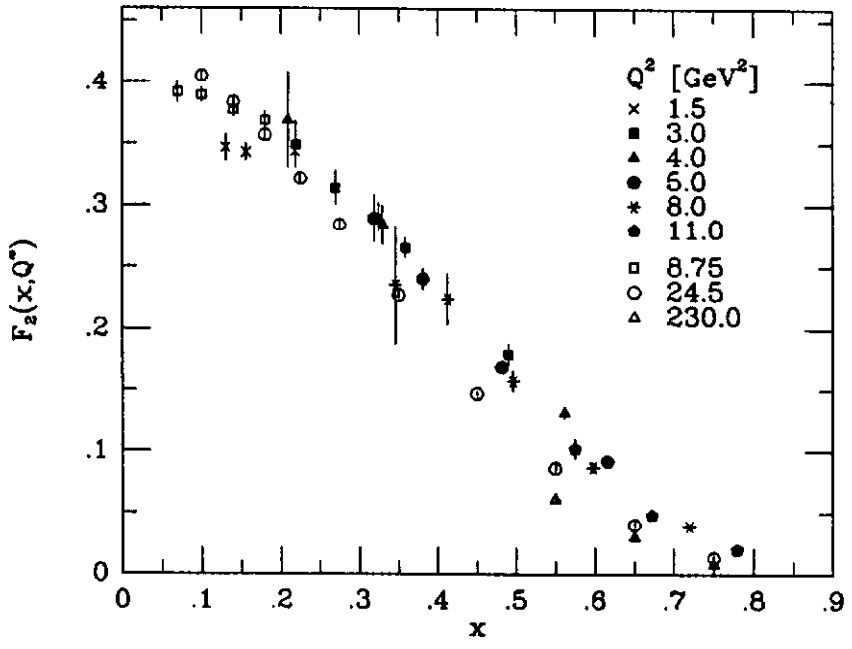

Figure 10: The F_2 structure function from the SLAC-MIT and BCDMS collaborations

F_2, measured with a proton target, are displayed. The data span nearly two decades of experiments, from the original SLAC-MIT measurements [29] to the most recent measurements from the BCDMS collaboration [30]. Only a representative sample of data points is shown. Note that even though the Q^2 values vary by two orders of magnitude, to a good approximation the data lie on a universal curve.

Bjorken scaling implies that the virtual photon scatters off *pointlike constituents*, since otherwise the dimensionless structure functions would depend on the ratio Q/Q_0, with $1/Q_0$ some length scale characterizing the size of the constituents. The 'parton model' picture of deep inelastic scattering is most easily formulated in a frame in which the proton is moving very fast – the *infinite momentum frame*. In this frame, we consider a simple model where the photon scatters off a pointlike quark which carries a fraction ξ of the proton's momentum. Setting $M^2 = 0$, we can rewrite Eq.(3.2) as

$$\frac{d^2\sigma}{dxdQ^2} = \frac{4\pi\alpha^2}{Q^4}\left[[1+(1-y)^2]F_1 + \frac{(1-y)}{x}(F_2 - 2xF_1)\right]. \qquad (3.5)$$

Now the spin-averaged matrix element squared for massless $eq \to eq$ scattering is

obtained simply by crossing the corresponding matrix element for $e^+e^- \to q\bar{q}$ considered in the previous lecture, *cf.*Eq.(2.3). In terms of the usual Mandelstam variables $\hat{s}, \hat{t}, \hat{u}$ we have

$$\overline{\sum}|M|^2 = 2e_q^2 e^4 \frac{\hat{s}^2 + \hat{u}^2}{\hat{t}^2}. \tag{3.6}$$

The notation $\overline{\sum}$ denotes the average (sum) over initial (final) colours and spins. Using Eq.(3.1) we can substitute for the deep inelastic variables: $\hat{t} = -Q^2$, $\hat{u} = \hat{s}(y-1)$ and $\hat{s} = Q^2/xy$. The differential cross section for the quark scattering process is therefore

$$\frac{d^2\hat{\sigma}}{dxdQ^2} = \frac{4\pi\alpha^2}{Q^4}[1 + (1-y)^2]\frac{1}{2}e_q^2\delta(x-\xi). \tag{3.7}$$

Comparing Eqs.(3.5) and (3.7) gives us the structure functions in this simple model:

$$\hat{F}_2 = xe_q^2\delta(x-\xi) = 2x\hat{F}_1. \tag{3.8}$$

This result suggests that the structure function $F_2(x)$ 'probes' a quark constituent with momentum fraction x. Now clearly the measured structure function is a distribution in x rather than a delta function, suggesting that the quark constituents carry a range of momentum fractions.

The above ideas are incorporated in what is now known as the 'naive parton model' [31]:

- $q(\xi)d\xi$ represents the probability that a quark q carries momentum fraction between ξ and $\xi + d\xi$
- the virtual photon scatters incoherently off the quark constituents

Thus

$$\begin{aligned} F_2(x) &= \sum_q \int_0^1 d\xi\ q(\xi)\ xe_q^2\delta(x-\xi) \\ &= \sum_q e_q^2 x q(x). \end{aligned} \tag{3.9}$$

and so for the scattering of a charged lepton off a proton target,

$$F_2^{em}(x) = x\left[\frac{4}{9}u(x) + \frac{1}{9}d(x) + \frac{1}{9}s(x) + \frac{4}{9}\bar{u}(x) + \ldots\right]. \tag{3.10}$$

For neutrino scattering - $\nu p \to lX$ - the virtual W^+ probe measures the quark distributions weighted by the *weak* charge:

$$F_2^\nu(x) = 2x\Big[d(x) + s(x) + \bar{u}(x) + \bar{c}(x) + \ldots\Big]. \tag{3.11}$$

A complete list of the most commonly encountered structure functions is given below.

$$\begin{aligned}
F_2^\nu &= 2x[d + s + \bar{u} + \bar{c}] \\
xF_3^\nu &= 2x[d + s - \bar{u} - \bar{c}] \\
F_2^{\bar{\nu}} &= 2x[u + c + \bar{d} + \bar{s}] \\
xF_3^{\bar{\nu}} &= 2x[u + c - \bar{d} - \bar{s}] \\
F_2^{em} &= x[\frac{4}{9}(u + u + c + \bar{c}) + \frac{1}{9}(d + \bar{d} + s + \bar{s})] \\
2xF_1 &= F_2.
\end{aligned} \tag{3.12}$$

This last result evident in Eq.(3.8) follows from the spin-$\frac{1}{2}$ property of the quarks.

With sufficient number of measured structure functions, the above relations can be inverted to give the quark distribution functions themselves. From such an analysis, the following picture emerges. The proton consists of three *valence* quarks (uud) which carry the electric charge and baryon quantum numbers of the proton, and an infinite *sea* of light $q\bar{q}$ pairs. When probed at scale Q, the sea contains all quark flavours with $m_q \ll Q$. Thus at a scale of $O(1\text{ GeV})$ we have

$$\begin{aligned}
u(x) &= u_V(x) + S(x) \\
d(x) &= d_V(x) + S(x) \\
\bar{u}(x) &= \bar{d}(x) = S(x).
\end{aligned} \tag{3.13}$$

with the sum rules

$$\begin{aligned}
\int_0^1 dx\, u_V(x) &= 2, \quad \int_0^1 dx\, d_V(x) = 1 \\
\sum_q \int_0^1 dx\, x(q(x) + \bar{q}(x)) &\simeq 0.5.
\end{aligned} \tag{3.14}$$

The last of these is an experimental result. It indicates that the quarks only carry about 50% of the proton's momentum. The rest is attributed to *gluon* constituents.

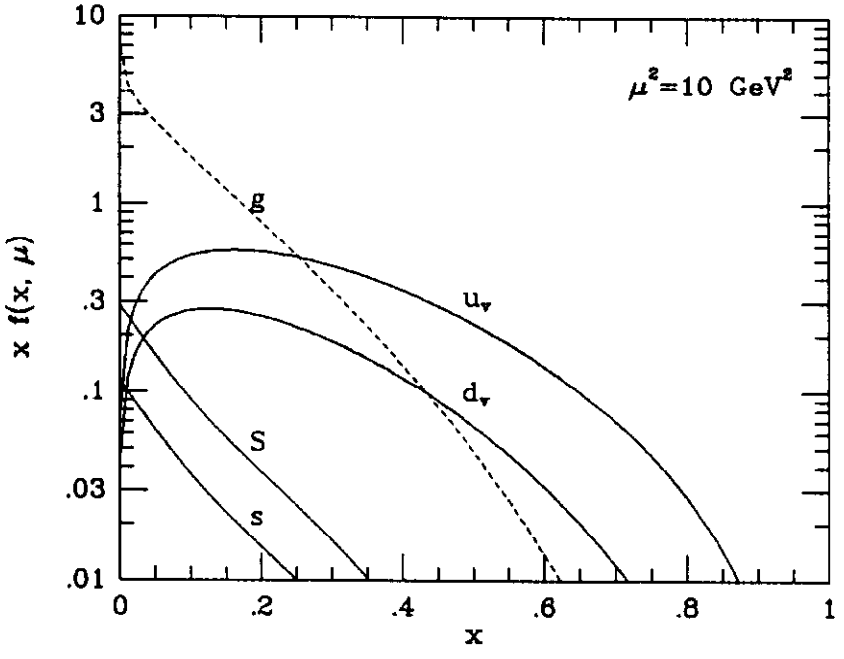

Figure 11: Quark and gluon distribution functions at $Q^2 = 10$ GeV^2

Although the gluons are not directly measured in deep inelastic lepton hadron scattering, their presence is evident in other hard scattering processes such as large transverse momentum jet and prompt photon production (see later). Fig.(11) shows a typical set of quark and gluon distributions extracted from fits to deep inelastic data, at $\mu^2 = 10$ GeV^2.

Closer examination of Fig.(10) reveals a systematic deviation from exact Bjorken scaling: the structure function decreases with increasing Q^2 at large x and has the opposite behaviour at small x. In the following section, we discuss how these scaling violations are understood in perturbative QCD.

3.2 Scaling violations and the Altarelli-Parisi equations

In the 'naive' parton model the structure functions *scale*, i.e. $F(x, Q^2) \to F(x)$ in the asymptotic (Bjorken) limit: $Q^2 \to \infty$, x fixed. In QCD, this scaling is *broken* by logarithms of Q. To see how this Q^2 dependence arises, consider the $O(\alpha_S)$ corrections to the $eq \to eq$ scattering process considered in the previous section. An explicit

calculation gives

$$\frac{1}{x}\hat{F}_2(x,Q^2) = e_q^2\Big[\delta(x-\xi)+\frac{\alpha_S}{2\pi}\frac{1}{\xi}\theta(\xi-x) \Big\{P(\frac{x}{\xi})\ln\frac{Q^2}{\kappa^2}+C(\frac{x}{\xi})\Big\}+\ldots\Big], \tag{3.15}$$

where P, C are calculable functions and κ is a regulator (for example, the quark virtuality $\kappa^2 = -p_q^2$) which is introduced to control the collinear divergence which arises when the gluon is emitted parallel to the incoming quark. This divergence is not subject to the theorems for cancellation of singularities discussed in the second lecture, because the virtual photon *can* resolve a quark and a collinear quark-gluon pair carrying the same overall momentum.

If we again integrate the above result with the quark distribution function $q(\xi)$ and choose to define Q^2-*dependent* quark distributions by

$$F_2(x,Q^2) = \sum_q e_q^2 x q(x,Q), \tag{3.16}$$

then we find to $O(\alpha_S)$,

$$q(x,\mu) = q(x)+\frac{\alpha_S}{2\pi}\int_x^1\frac{d\xi}{\xi}q(\xi)\Big\{P(\frac{x}{\xi})\ln\frac{\mu^2}{\kappa^2}+C(\frac{x}{\xi})\Big\}+\ldots. \tag{3.17}$$

How can we interpret the limit $\kappa^2 \to 0$? Exactly as for the renormalisation of the coupling constant, we can regard $q(x)$ as an unmeasureable, *bare* distribution. The collinear singularities are absorbed into this bare distribution at a 'factorisation scale' μ_0, which plays a similar role to the renormalisation scale. There is therefore no absolute prediction for the 'renormalised' distribution $q(x,\mu)$. What the theory does tell us, however, is how the distribution varies with μ^2. Thus if we define $t = \ln(\mu^2/\mu_0^2)$ and take the t-derivative of Eq.(3.17) we obtain

$$\frac{d}{dt}q(x,t) = \frac{\alpha_S(t)}{2\pi}\int_x^1\frac{d\xi}{\xi}q(\xi,t)P(\frac{x}{\xi}). \tag{3.18}$$

This equation – known as the Altarelli-Parisi equation – is the analogue of the β function equation describing the variation of $\alpha_S(t)$ with t.

The above derivation is rather heuristic, but a more complete treatment confirms and extends the result. The full prediction of the theory is most easily cast in terms

of the *moments* (Mellin transforms) of the distributions:

$$q(j,t) = \int_0^1 dx\, x^{j-1}\, q(x,t). \tag{3.19}$$

In terms of these moments, the t dependence of the quark distribution function is given by

$$\frac{dq(j,t)}{dt} = \gamma_{qq}\left(j, \alpha_S(t)\right) q\left(j,t\right). \tag{3.20}$$

We next define P_{qq} as the inverse Mellin transform of γ_{qq},

$$\frac{\alpha_S}{2\pi}\, P_{qq}\left(x, \alpha_S\right) = \frac{1}{2\pi i} \int dj\, x^{-j}\, \gamma_{qq}(j, \alpha_S), \tag{3.21}$$

where the integration contour in the complex j plane is parallel to the imaginary axis and to the right of all singularities of the integrand. Taking the inverse Mellin transform of Eq.(3.20), we obtain in x space,

$$\begin{aligned} \frac{dq(x,t)}{dt} &= \frac{\alpha_S(t)}{2\pi} \int_0^1 d\xi \int_0^1 dz\, \delta(x - \xi z) P_{qq}(z, \alpha_S(t)) q(\xi, t) \\ &= \frac{\alpha_S(t)}{2\pi} \int_x^1 \frac{d\xi}{\xi}\, P_{qq}\Big(\frac{x}{\xi}, \alpha_S(t)\Big) q(\xi, t). \end{aligned} \tag{3.22}$$

P_{qq} has a perturbative expansion in the running coupling,

$$P_{qq}(z, \alpha_S) = P_{qq}^{(0)}(z) + \frac{\alpha_S}{2\pi} P_{qq}^{(1)}(z) + \ldots \tag{3.23}$$

Retaining only the first term in this expansion gives precisely the result in Eq.(3.18), with $P \equiv P_{qq}^{(0)}$.

In fact the above derivations are strictly only correct for *differences* between quark distributions, $q = q_i - q_j$. In general, the Altarelli-Parisi (AP) equation is a matrix equation,

$$\frac{d}{dt} \begin{pmatrix} q(x,t) \\ g(x,t) \end{pmatrix} = \frac{\alpha_S(t)}{2\pi} \int_x^1 \frac{d\xi}{\xi} \begin{pmatrix} P_{qq}\left(\frac{x}{\xi}, \alpha_S(t)\right) & P_{qg}\left(\frac{x}{\xi}, \alpha_S(t)\right) \\ P_{gq}\left(\frac{x}{\xi}, \alpha_S(t)\right) & P_{gg}\left(\frac{x}{\xi}, \alpha_S(t)\right) \end{pmatrix} \begin{pmatrix} q(\xi,t) \\ g(\xi,t) \end{pmatrix}. \tag{3.24}$$

The AP kernels $P_{ij}^{(0)}(x)$ have an attractive physical interpretation as the probability of finding parton i in a parton of type j with a fraction x of the longitudinal momentum of the parent parton and a transverse momentum much less than μ. The interpretation

as probabilities implies that the AP kernels are positive definite for $x < 1$. They satisfy the following relations:

$$\begin{aligned}
&\int_0^1 dx P_{qq}^{(0)}(x) = 0 \\
&\int_0^1 dx\, x\left[P_{qq}^{(0)}(x) + P_{gq}^{(0)}(x)\right] = 0 \\
&\int_0^1 dx\, x\left[2n_f P_{qg}^{(0)}(x) + P_{gg}^{(0)}(x)\right] = 0.
\end{aligned} \tag{3.25}$$

These equations correspond to quark number conservation and momentum conservation in the splittings of quarks and gluons.

The kernels of the AP equations are calculable as a power series in the strong coupling α_S. Both the lowest order terms [32] and the first correction [33] to the evolution kernels have been calculated. The lowest order approximations to the evolution kernels are:

$$\begin{aligned}
P_{qq}^{(0)}(x) &= C_F\left[\frac{1+x^2}{(1-x)_+} + \frac{3}{2}\delta(1-x)\right], \\
P_{qg}^{(0)}(x) &= T_R\left[x^2 + (1-x)^2\right], \quad T_R = \frac{n_f}{2}, \\
P_{gq}^{(0)}(x) &= C_F\left[\frac{1+(1-x)^2}{x}\right], \\
P_{gg}^{(0)}(x) &= 2N\left[\frac{x}{(1-x)_+} + \frac{1-x}{x} + x(1-x)\right] + \delta(1-x)\frac{(11N - 4n_f T_R)}{6}.
\end{aligned} \tag{3.26}$$

The 'plus prescription' on the singular parts of the kernels is defined as

$$\int_0^1 dx\, f(x)[g(x)]_+ = \int_0^1 dx\, \left(f(x) - f(1)\right) g(x). \tag{3.27}$$

In terms of moments these four evolution kernels take the form

$$\begin{aligned}
\gamma_{qq}^{(0)}(j) &= C_F\left[-\frac{1}{2} + \frac{1}{j(j+1)} - 2\sum_{k=2}^{j}\frac{1}{k}\right], \\
\gamma_{qg}^{(0)}(j) &= T_R\left[\frac{(2+j+j^2)}{j(j+1)(j+2)}\right],
\end{aligned}$$

$$\begin{aligned}\gamma_{gq}^{(0)}(j) &= C_F\left[\frac{(2+j+j^2)}{j(j^2-1)}\right], \\ \gamma_{gg}^{(0)}(j) &= 2N\left[-\frac{1}{12}+\frac{1}{j(j-1)}+\frac{1}{(j+1)(j+2)}-\sum_{k=2}^{j}\frac{1}{k}\right]-\frac{2}{3}n_f T_R.\end{aligned} \tag{3.28}$$

In general the AP equation is a $(2n_f+1)$ dimensional matrix equation in the space of quarks, antiquarks and gluons. However not all of the evolution kernels are distinct so the matrix equation can be considerably simplified. Because of charge conjugation we have that,

$$P_{qq} = P_{\bar{q}\bar{q}}, \quad P_{qg} = P_{\bar{q}g}. \tag{3.29}$$

At lowest order we have in addition the following relations,

$$P_{\bar{q}q}^{(0)} = 0, \quad P_{q_iq_j}^{(0)} = 0 \quad (i \neq j). \tag{3.30}$$

The solution of the AP equation is simplified by considering combinations which are non-singlet (in flavour space) such as $q_i - \bar{q}_i$ or $q_i - q_j$. In this combination the mixing with the flavour singlet gluons drops out and we have, $(V = q_i - q_j)$,

$$\frac{d}{dt}V(x,t) = \frac{\alpha_S(t)}{2\pi}\left[P_{qq}(\xi) \otimes V(z,t)\right], \tag{3.31}$$

where $\otimes$ is a shorthand notation for the convolution integral of Eq.(3.22). Taking moments, this equation becomes

$$\frac{dV(j,t)}{dt} = \frac{\alpha_S(t)}{2\pi}\gamma_{qq}^{(0)}(j)\, V(j,t). \tag{3.32}$$

Inserting the lowest order form for the running coupling, we find the solution

$$V(j,t) = V(j,0)\left(\frac{\alpha_S(0)}{\alpha_S(t)}\right)^{d_{qq}(j)}, \quad d_{qq}(j) = \frac{\gamma_{qq}^{(0)}(j)}{2\pi b}. \tag{3.33}$$

It is straightforward to show that $d_{qq}(1) = 0$ and that $d_{qq}(j) < 0$ for $j \geq 2$. This in turn implies that as μ increases the distribution function *decreases* at large x and *increases* at small x. Physically, this can be understood as an increase in the

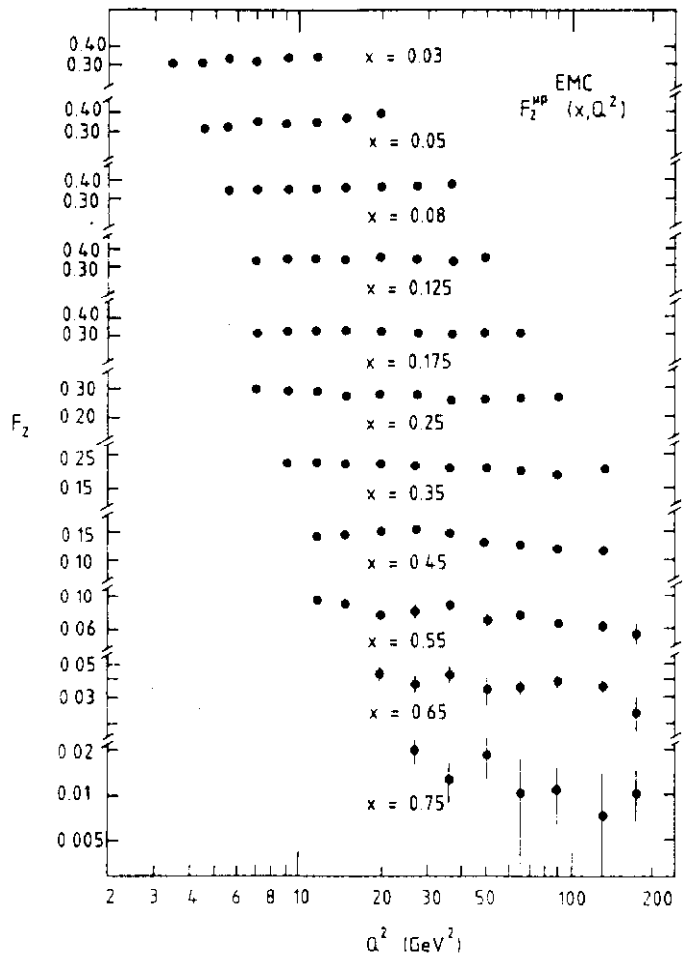

Figure 12: The structure function F_2 measured in high energy muon-proton scattering by the EMC

phase space for gluon emission by the quarks as μ increases, with a corresponding degradation in momentum. The trend is clearly visible in the data. Fig.(12) shows data on the structure function $F_2^{\mu p}$ measured by the EMC [34].

We now turn to the flavour singlet combination of moments. Define the sum over all quark flavours to be given by Σ,

$$\Sigma = \sum_i (q_i + \bar{q}_i). \tag{3.34}$$

From Eq.(3.24), which holds for all flavours of quarks, we derive the equation for the

flavour singlet combination of parton distributions,

$$\begin{aligned}\frac{d\Sigma}{dt} &= \frac{\alpha_S(t)}{2\pi}\left[P_{qq}^{(0)}\otimes\Sigma + 2n_f P_{qg}^{(0)}\otimes g\right] + O\left(\alpha_S^2(t)\right)\\ \frac{dg}{dt} &= \frac{\alpha_S(t)}{2\pi}\left[P_{gq}^{(0}\otimes\Sigma + P_{gg}^{(0)}\otimes g\right] + O\left(\alpha_S^2(t)\right).\end{aligned} \tag{3.35}$$

This equation is most easily solved by direct numerical integration in x space starting with an input distribution obtained from data.

We can illustrate some simple properties of the distributions using the moments. Taking the second ($j = 2$) moment of Eq.(3.35) we find that

$$\frac{d}{dt}\begin{pmatrix}\Sigma(2)\\ g(2)\end{pmatrix} = \frac{\alpha_S(t)}{2\pi}\begin{pmatrix}-C_F\frac{4}{3} & \frac{n_f}{3}\\ C_F\frac{4}{3} & \frac{-n_f}{3}\end{pmatrix}\begin{pmatrix}\Sigma(2)\\ g(2)\end{pmatrix}. \tag{3.36}$$

The eigenvectors and corresponding eigenvalues of this system of equations are

$$\begin{aligned}O^+(2) &= \Sigma(2) + g(2) \qquad \text{Eigenvalue : } 0\\ O^-(2) &= \Sigma(2) - \frac{n_f}{4C_F}g(2) \qquad \text{Eigenvalue : } -\left(\frac{4}{3}C_F + \frac{n_f}{3}\right).\end{aligned} \tag{3.37}$$

Note that the combination O^+, which corresponds to the total momentum carried by the quarks and gluons, is independent of t. The eigenvector O^- vanishes at asymptotic t:

$$O^-(2) = \left(\frac{\alpha_S(0)}{\alpha_S(t)}\right)^{d^-(2)} \to 0, \quad d^-(2) = \frac{-(\frac{4}{3}C_F + \frac{n_f}{3})}{2\pi b} \tag{3.38}$$

So that asymptotically we have

$$\frac{\Sigma(2)}{g(2)} = \frac{n_f}{4C_F} = \frac{Nn_f}{2(N^2-1)}. \tag{3.39}$$

The momentum fractions carried by the quarks and gluons in the $\mu \to \infty$ limit are therefore

$$\Sigma(2)\Big|_{t=\infty} = \left(\frac{n_f}{4C_F + n_f}\right), \quad g(2)\Big|_{t=\infty} = \left(\frac{4C_F}{4C_F + n_f}\right). \tag{3.40}$$

Note, however, that the approach to the asymptotic limit is controlled by $t \sim \ln\mu^2$ and is therefore quite slow. For a tabulation of the eigenvectors and eigenvalues of

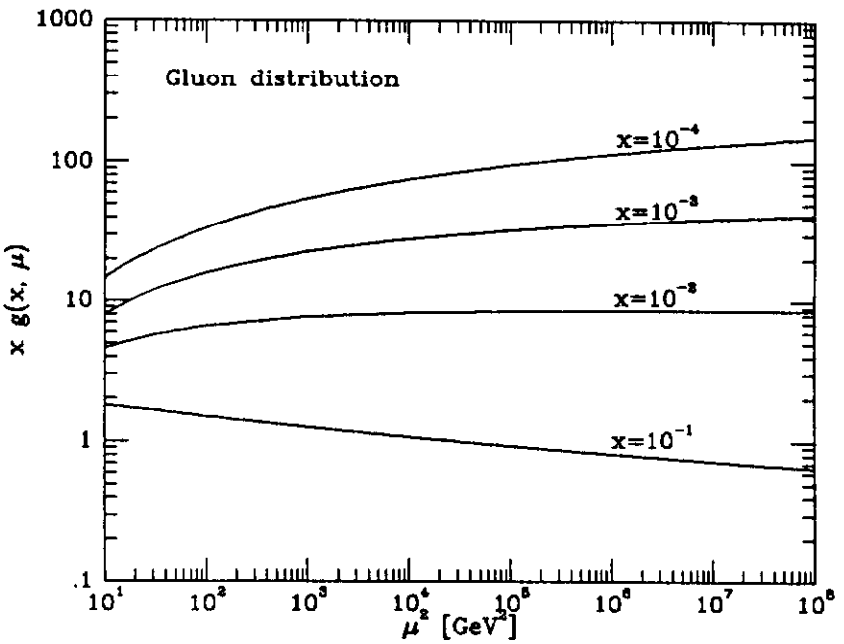

Figure 13: The scale dependence of the gluon distribution

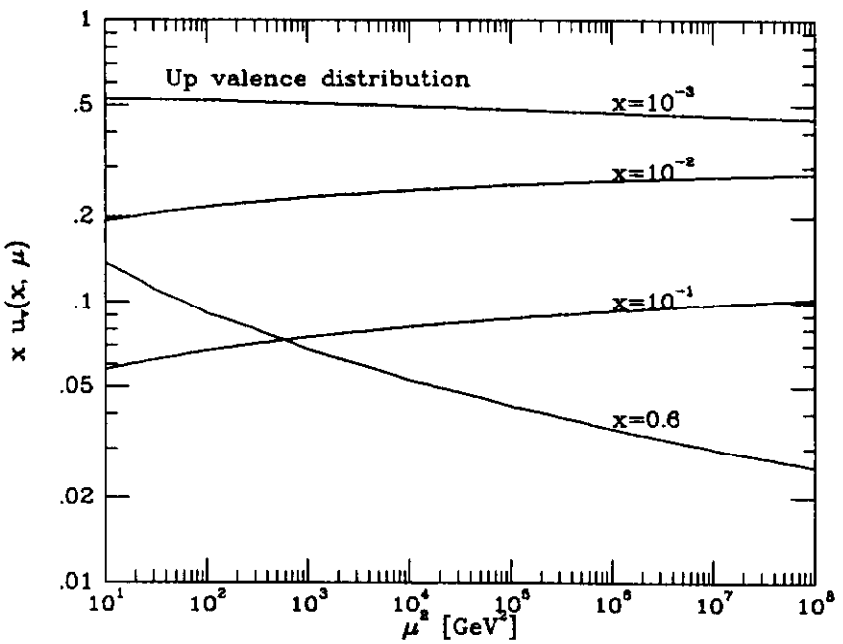

Figure 14: The scale dependence of the valence up distribution

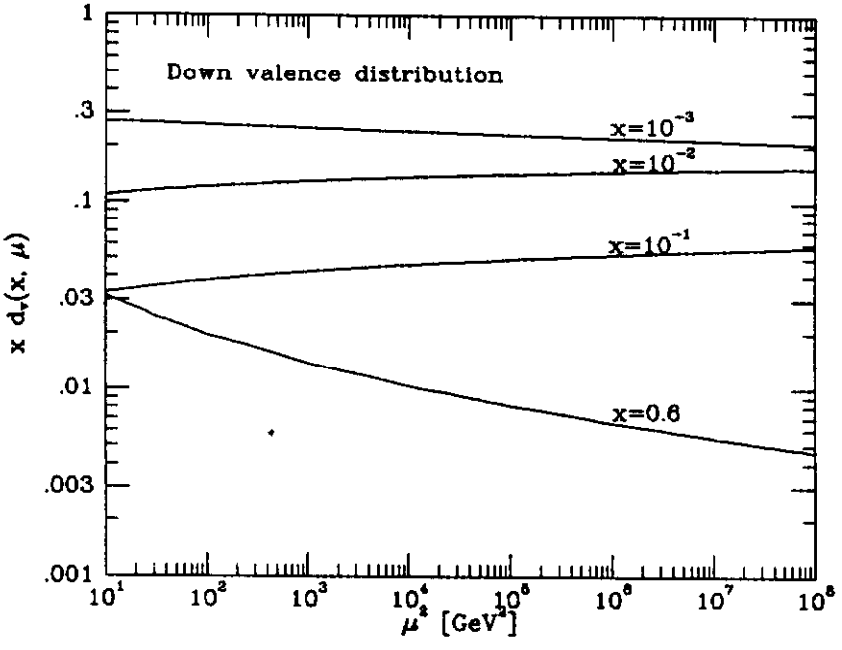

Figure 15: The scale dependence of the valence down distribution

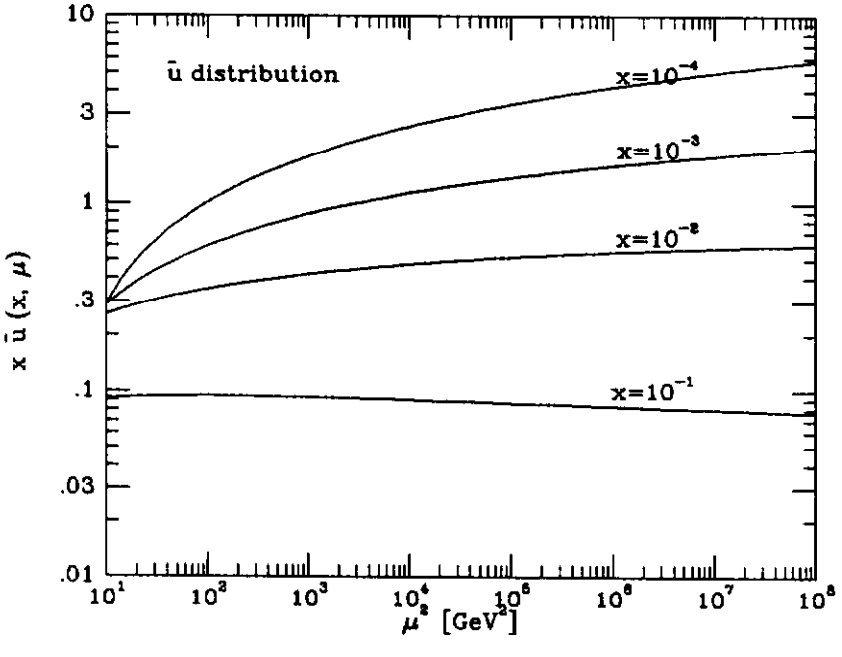

Figure 16: The scale dependence of the anti-up quark distribution

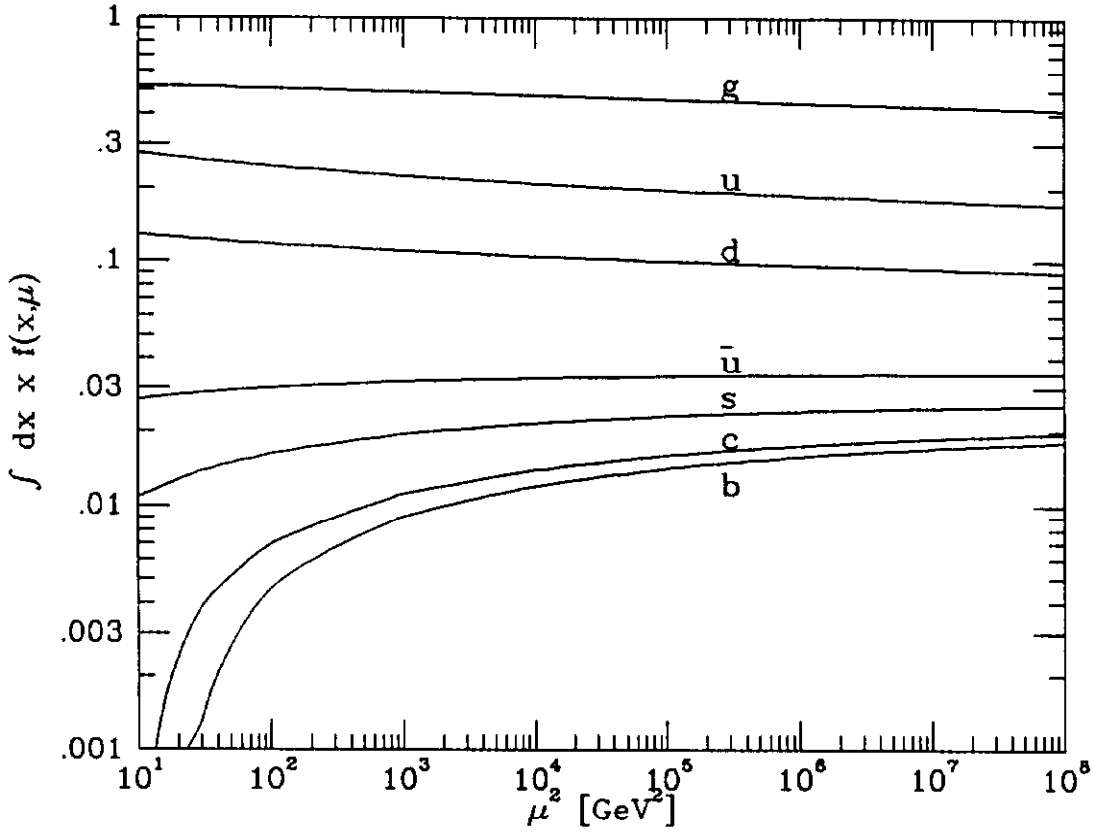

Figure 17: Momentum fractions carried by the quarks and gluons as functions of the scale

the moments of Eq.(3.35) we refer the reader to reference [5]. Figs.(13) - (17) show the scale dependence of the quark and gluon distributions.

3.3 QCD fits to deep inelastic data

In the the previous section we saw that perturbative QCD predicts the Q^2 *evolution* of the structure functions, rather than the size and shape of the functions themselves. Quantitatively, the variation with Q^2 is controlled by $\alpha_S(Q)$ and hence by the QCD scale parameter Λ. Deep inelastic scattering data of the type shown in Fig.(12), therefore, provide one of the 'precision' tests of QCD and, arguably, the most accurate determination of $\Lambda_{\overline{\rm MS}}$.

Although the theoretical predictions appear simplest when expressed in terms of structure function moments, it is very difficult to extract such moments from the data. This is because the measurements do not extend to very large and very small x, and some form of *ad hoc* extrapolation is required to construct the moment integrals. A more practical and accurate method is to choose a reference value Q_0 and parametrise the parton distributions at that value, e.g. $q(x,Q_0) = Ax^a(1-x)^b$. These distributions are then evolved numerically, using the Altarelli-Parisi equations, to obtain values for the $F_i(x,Q^2)$ in the kinematic regions where they are measured. Note that in this approach the rate of change with Q^2 of the structure function at a given x depends only on the structure function evaluated at $\xi > x$, c.f. Eq.(3.24). Finally, a global numerical fit is performed to determine the 'best' values for the parameters, including Λ. The extent to which the measured value of Λ depends on the other parameters can also be quantified and used to derive a systematic error.

The above procedure is not, however, without problems. The most serious of these are:

- In QCD, the structure functions have 'higher twist' power corrections, which are much more difficult to estimate quantitatively:

$$F(x,Q^2) \;=\; F^{(2)}(x,Q^2) \;+\; \frac{F^{(4)}(x,Q^2)}{Q^2} \;+\; \ldots, \qquad (3.41)$$

  where the superscripts on the right-hand-side refer to the 'twist' = (dimension − spin) of the contributing operators. To avoid these complications, the analysis must be performed at large Q^2 where the power suppressed terms are negligible.

- The structure function F_2 can be decomposed into singlet and non-singlet ('sea quark' and 'valence quark') parts, which dominate at small and large x respectively. Hence, except at large x, the Q^2 dependence of F_2 is sensitive to the *a priori* unknown gluon distribution and there is potentially a strong Λ-gluon correlation.

- Non-singlet structure functions do not suffer from the gluon correlation problem (see Eq.(3.31)), but these are only measurable experimentally by constructing differences between cross sections, e.g. $\sigma^{\mu p} - \sigma^{\mu n}$. This inevitably introduces additional systematic and statistical uncertainties.

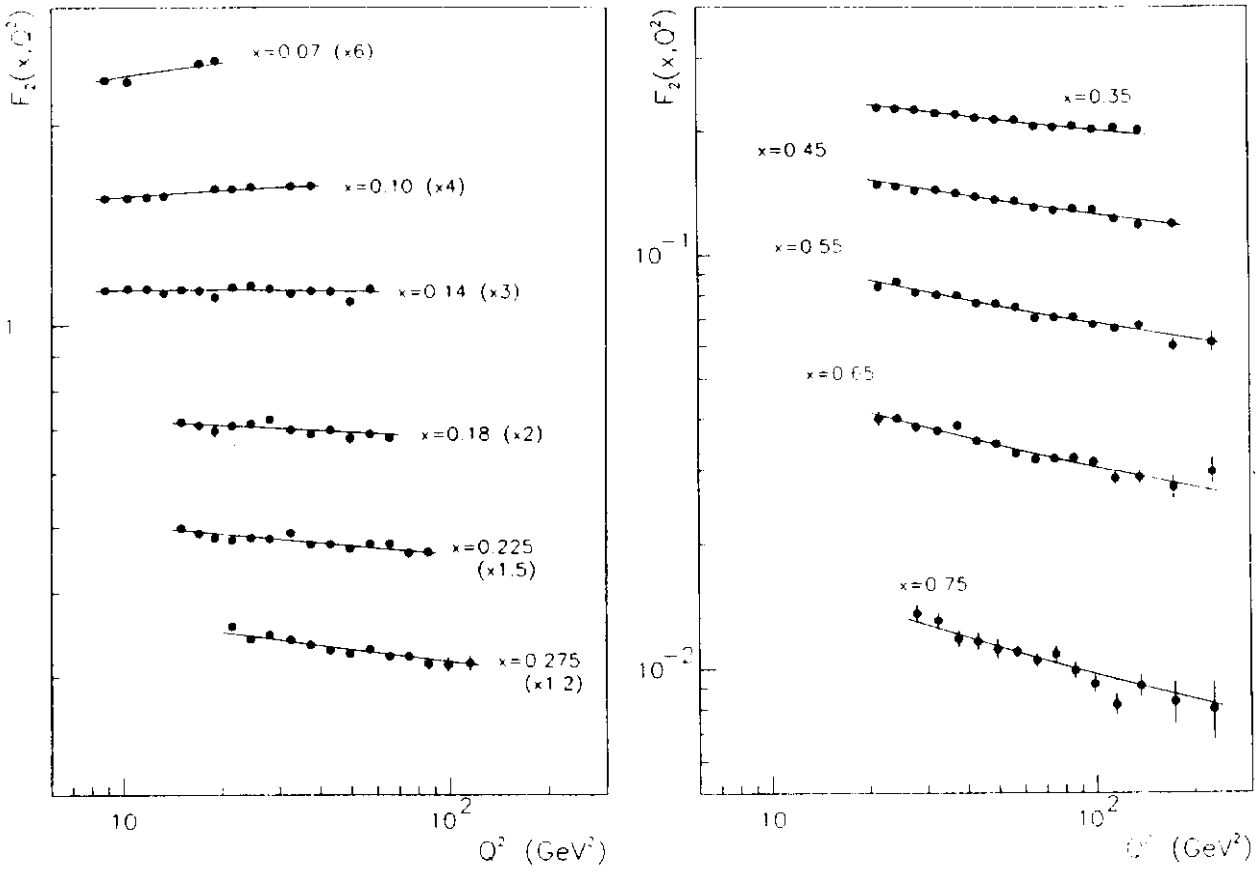

Figure 18: Data on the structure function F_2 in muon-hydrogen scattering, from BCDMS

The most recent generation of deep inelastic experiments partially solve these problems by collecting high statistics data at large x and Q^2. In fact the precision of contemporary data demands that the next-to-leading order QCD predictions are used in the fits. Beyond leading order a specific renormalisation scheme must be chosen, and in practice this is usually the $\overline{MS}$ scheme. For this reason the results quoted in the literature almost always refer to $\Lambda_{\overline{\rm MS}}$.

Some of the most precise recent data comes from the BCDMS collaboration [30,35]. As an example, Fig.(18) shows the structure function F_2 measured in deep inelastic muon-hydrogen scattering. The measurements extend up to x values of 0.75 and Q^2 values of several hundred GeV^2. Fig.(19) shows the corresponding logarithmic Q^2 derivative of $\log F_2$ as a function of x. Note that the derivatives in this region are negative, consistent with a structure function which decreases with increasing Q^2. Also shown are the predictions of next-to-leading order QCD for three different values

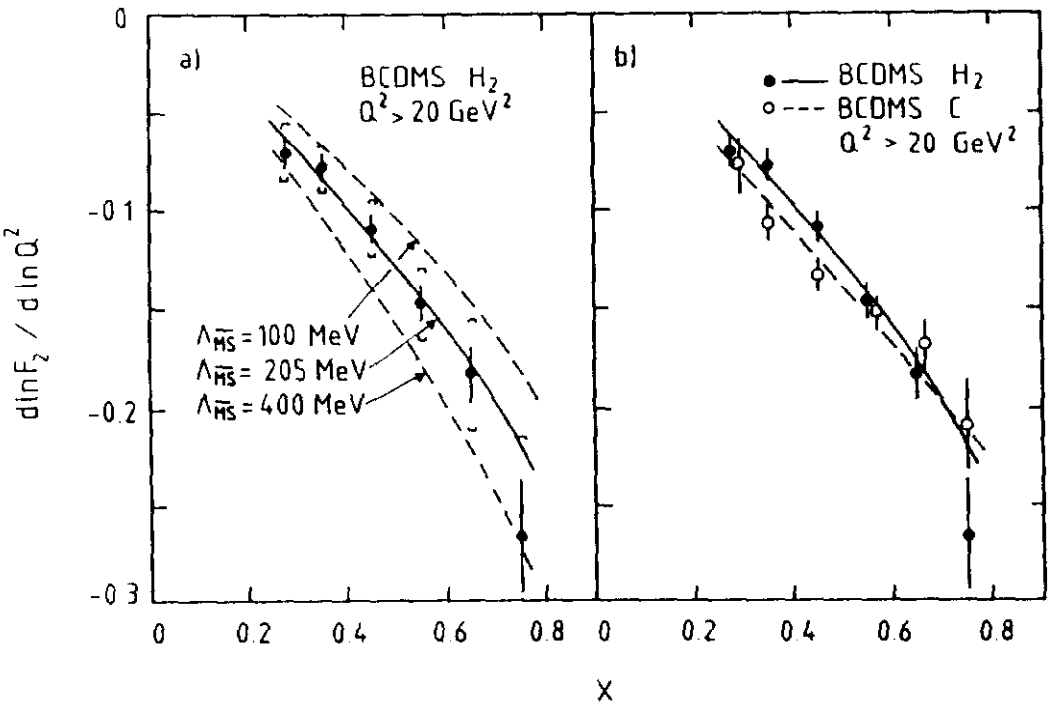

Figure 19: Logarithmic Q^2 derivative of the F_2 structure function in the previous figure with QCD fits, from BCDMS

of $\Lambda_{\overline{\rm MS}}$. A detailed fit gives [35]

$$\Lambda^{(4)}_{\overline{\rm MS}} \;=\; 220 \;\pm\; 15 \;\pm\; 50 \text{ MeV} \tag{3.42}$$

This result for $\Lambda_{\overline{\rm MS}}$ is compared with determinations from other processes in Fig.(2).

Deep inelastic experiments measure quark densities over a broad range in x up to about $Q = 15$ GeV. Knowing $\Lambda_{\overline{\rm MS}}$, these can then be evolved to higher μ and used for hadron collider phenomenology. Instead of laboriously integrating the Altarelli-Parisi equations each time a parton distribution is required, it is useful to have an analytic approximation, valid to a sufficient accuracy over a prescribed (x, μ) range. Several such parametrisations are available.

The widely used Duke and Owens parametrisations [36], for example, are of the form

$$\begin{aligned} q(x,Q) &= Ax^a(1+cx)(1-x)^b \\ A &= A_0 + A_1 s + A_2 s^2 \qquad \text{etc.} \end{aligned}$$

$$s = \ln\left(\frac{\ln(Q^2/\Lambda^2)}{\ln(Q_0^2/\Lambda^2)}\right) > 0, \tag{3.43}$$

with the parameters A_0, A_1, ... fitted to an exact leading order evolution to give an accuracy of a few per cent. Because deep inelastic scattering does not significantly constrain the gluon distribution, it was usual – in the past – to include in the parametrisations a choice of gluon distributions, typically a 'hard gluon' and a 'soft gluon', each with its own Λ value. Nowadays, high precision fixed-target prompt photon experiments are able to constrain the gluon, particularly in the medium x range, and 'hard gluon' parametrisations are ruled out [37]. The most recent generation of parton distributions – for example the HMRS sets [38] – are obtained from next-to-leading order QCD fits to a wide variety of deep inelastic data, as well as data from prompt photon and lepton pair production. The distributions cover a wide range in x and μ, and are ideal for making quantitative predictions for present and future hadron-hadron and lepton-hadron colliders.

3.4 Small x behaviour of the parton distributions

From Fig.(13), we see that the gluon distribution grows rapidly at small x. In the asymptotic limit where $x \to 0$ and $\mu \to \infty$ it is possible to determine the behaviour of the distributions directly from the Altarelli-Parisi equations.

The $x \to 0$ limit of the parton distributions is controlled by the behaviour of the anomalous dimensions $\gamma(j)$ near $j = 1$. Considering the gluon only we have

$$\frac{d}{dt}g(j,t) = \frac{\alpha(t)}{2\pi}\gamma_{gg}^{(0)}(j)g(j,t) \tag{3.44}$$

where from Eq.(3.28),

$$\gamma_{gg}^{(0)}(j) \approx \frac{2N}{j-1}. \tag{3.45}$$

In this limit the solution for the moments of the gluon distribution is,

$$g(j,t) = g(j,t_0)\exp\left(\frac{N\xi}{\pi b(j-1)}\right), \tag{3.46}$$

and ξ is defined by,

$$\xi = b\int_{t_0}^{t} dt'\alpha_S(t'). \tag{3.47}$$

To return to x space we perform the inverse Mellin transform as given by Eq.(3.21)

$$G(x,t) \equiv xg(x,t) = \frac{1}{2\pi i}\int dj\, x^{-(j-1)} g(j,t) \tag{3.48}$$

$$\equiv \frac{1}{2\pi i}\int dj\, g(j,t_0)\exp\Big[f(j)\Big] g(j,t_0) \tag{3.49}$$

where the exponent f is,

$$f(j) = \Big[(j-1)\ln(1/x) + \frac{N\xi}{\pi b(j-1)}\Big]. \tag{3.50}$$

In the limit in which both $\ln(1/x)$ and ξ tend to infinity we can estimate this integral by expanding about the saddle point of the exponential:

$$f(j) = \sqrt{2\xi y} + O(j-j_0)^2,\ \ j_0 = 1 + \frac{N}{\pi b}\sqrt{\frac{2\xi}{y}},\ \ y = \frac{2N}{\pi b}\ln(1/x). \tag{3.51}$$

We therefore find for the asymptotic solution

$$G(x,t) = g(j_0,t_0)\exp\sqrt{2\xi y}, \tag{3.52}$$

which expressed in the original variables yields

$$g(x) \sim \frac{1}{x}\exp\sqrt{\frac{4N}{\pi b}\ln\frac{\ln\mu^2/\Lambda^2}{\ln\mu_0^2/\Lambda^2}\ln\frac{1}{x}},\ \ N=3,\ \ b = \frac{(33-2n_f)}{12\pi}. \tag{3.53}$$

Notice that the dependence on the starting distribution enters via the j_0th moment of g. Therefore at fixed ξ/y the initial information enters only as an overall factor.

A topic which is presently under active investigation [39] is the mechanism which limits the growth of the gluon distribution. In the infinite momentum frame the gluon momentum distribution $G(x,t)$ gives the number of gluons per unit of rapidity with a transverse size greater than $1/\mu$. If the number of gluons grows so large that the partons start to overlap inside the nucleon new effects will come into play. A crude estimate of when this begins to happen is provided by,

$$G(x,t) = \frac{\text{Area of hadron}}{\text{Area of parton}} \sim \mu^2 r^2 \sim \mu^2\ 25\ \text{GeV}^{-2}, \tag{3.54}$$

where $r \sim 1/m_\pi$ is the radius of the hadron. At presently attainable values of x the value of $G(x,t)$ does not exceed 3 or 4, so, if the above estimate is correct, the saturation limit is beyond the range of the present colliders.

4. The QCD Parton Model in Hadron-Hadron Collisions

In this lecture we shall consider the application of the parton model to processes involving two hadrons in the initial state.

4.1 The QCD improved parton model

The high energy interactions of hadrons are described by the QCD improved parton model. In this model a hard scattering process between two hadrons is the result of an interaction between the quarks and gluons which are the constituents of the incoming hadrons. The incoming hadrons provide broad band beams of partons which possess varying fractions of the momenta of their parent hadrons, as described in the previous lecture.

The cross section for a hard scattering process initiated by two hadrons with four-momenta P_1 and P_2 can be written as

$$\sigma(P_1,P_2) = \sum_{i,j}\int dx_1 dx_2\ f_i(x_1,\mu) f_j(x_2,\mu)\ \hat{\sigma}_{ij}(p_1,p_2,\alpha_S(\mu),Q). \qquad (4.1)$$

The parton model for hard scattering events is depicted in Fig.(20). The momenta of the partons which participate in the hard interaction are $p_1 = x_1 P_1$ and $p_2 = x_2 P_2$. The characteristic scale of the hard scattering is denoted by Q. This could be, for example, the mass of a weak boson or heavy quark, or the transverse momentum of a jet. The functions $f_i(x,\mu)$ are the usual QCD quark or gluon distributions, defined at factorisation scale μ. The short distance cross section for the scattering of partons of type i and j is denoted by $\hat{\sigma}_{ij}$. Since the coupling is small at high energy, the short distance cross section can be calculated as a perturbation series in the running coupling α_S. Therefore the nth order approximation to the short distance cross section is given by

$$\hat{\sigma} = c^{(0)}\alpha_S^k\Big(1+\sum_{j=1}^{n} c^{(j)}\alpha_S^j\Big), \qquad (4.2)$$

where the $c^{(j)}$ are functions of the kinematic variables.

In the leading approximation ($n = 0$) the short distance cross section is identical to the normal parton scattering cross section calculated in exactly the same way as the cross section for a QED process. In higher orders, the short distance cross

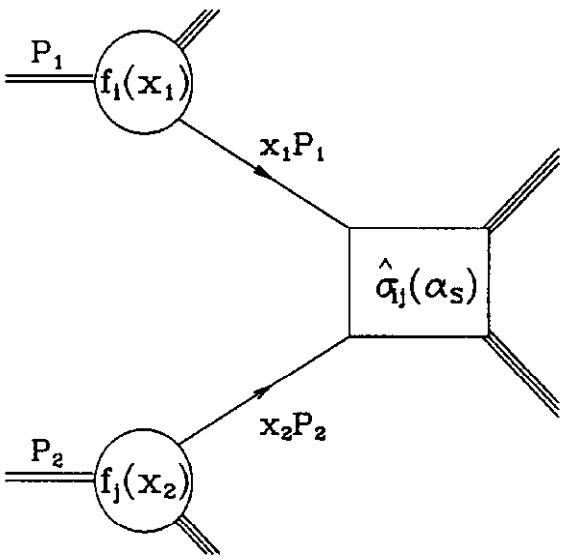

Figure 20: Schematic of the parton model description of a hard scattering process

section is derived from the parton scattering cross section by removing long distance pieces and factoring them into the parton distribution functions. The remaining cross section involves only high momentum transfers and is insensitive to the physics of low momentum scales. In particular, the short distance cross section does not depend on the details of the hadron wave function or the type of the incoming hadron. It is a purely short-distance construct and is calculable in perturbation theory because of asymptotic freedom. This factorisation property of the cross section can be proved to all orders in perturbation theory. For more details, see for example reference [40]. A heuristic argument for the validity of factorisation is given in the next section. It is a fundamental property of the theory which turns QCD into a reliable calculational tool with controllable approximations, distinguishing it from the 'naive' parton model of Feynman [31].

The scale μ in Eq.(4.1) is an arbitrary parameter. It should be chosen to be of the order of the hard scale Q which characterises the parton-parton interaction. The more terms are included in the perturbative expansion, the weaker the dependence on μ.

Finally, it should be emphasised that Eq.(4.1) is not a description of the bulk of

the events which occur at a hadron-hadron collider, but as we shall see, it can be used to describe the most interesting classes of events which involve a hard interaction.

4.2 Factorisation of the cross section

The property of factorisation allows us to use the QCD parton model to describe inelastic processes. In this section we shall present a simple classical model that illustrates why the factorisation property holds and when it should fail. As an example of a hard process we consider the production of a massive vector boson V – in practice a massive photon, W or Z – in the collision of two hadrons,

$$H_1(P_1) + H_2(P_2) \to V + X. \tag{4.3}$$

This is in many respects the simplest hard process involving two hadrons, since the observed vector boson in the final state carries no colour and its leptonic decay products are observed directly. It is therefore the easiest to analyse theoretically and consequently has received the most theoretical attention.

A very important theoretical issue in this process is whether the partons in hadron H_1, through the influence of their colour fields, change the distribution of partons in hadron H_2 before the hard scattering occurs, thus spoiling the simple parton picture. Soft gluons which are created long before the collision are potentially troublesome in this respect.

We shall argue that soft gluons do not in fact spoil the parton picture, using a simple model [41] from classical electrodynamics. The vector potential due to a current density J is given by [42]

$$A^\mu(t,\vec{x}) = \int dt' d\vec{x}' \, \frac{J^\mu(t',\vec{x}')}{|\vec{x}-\vec{x}'|} \, \delta(t' + |\vec{x}-\vec{x}'| - t), \;\; c = 1, \tag{4.4}$$

where the delta function provides the retarded behaviour required by causality. Consider a particle with charge e travelling in the positive z direction with constant velocity β. The non-zero components of the current density are

$$\begin{aligned} J^t(t,\vec{x}) &= e\delta(\vec{x} - \vec{r}(t)) \\ J^z(t,\vec{x}) &= e\beta\delta(\vec{x} - \vec{r}(t)), \;\; \vec{r}(t) = \beta t\hat{z}, \end{aligned} \tag{4.5}$$

where $\hat{z}$ is a unit vector in the z direction. The charge passes through the origin at time $t = 0$. At an observation point (the position of hadron H_2) described by coordinates x, y and z, the vector potential at time t due to the passage of the fast moving charge is obtained by performing the integrations in Eq.(4.4) using the current density of Eq.(4.5). The result is

$$\begin{aligned} A^t(t,\vec{x}) &= \frac{e\gamma}{\sqrt{[x^2+y^2+\gamma^2(\beta t - z)^2]}} \\ A^x(t,\vec{x}) &= 0 \\ A^y(t,\vec{x}) &= 0 \\ A^z(t,\vec{x}) &= \frac{e\gamma\beta}{\sqrt{[x^2+y^2+\gamma^2(\beta t - z)^2]}}, \end{aligned} \tag{4.6}$$

where $\gamma^2 = 1/(1-\beta^2)$. The observation point can be taken to be the target hadron H_2 which is at rest near the origin, so that $\gamma \approx s/m^2$. Note that for large γ and fixed non-zero $(\beta t - z)$ some components of the potential tend to a constant independent of γ, suggesting that there will be non-zero fields which are not in coincidence with the arrival of the particle, even at high energy. However at large γ the potential is a pure gauge piece and hence does not lead to E or B fields. The implication of this result is that a covariant formulation which uses the vector potential A will not be the most efficient method to handle this problem, since we will have large fields which ultimately have no physical effect.

To show that these large terms in the vector potential have no effect we compute the field strengths from Eq.(4.6). The leading terms in γ cancel and the field strengths are of order $1/\gamma^2$ and hence of order m^4/s^2. For example, the electric field along the z direction is

$$E^z(t,\vec{x}) = F^{tz} \equiv \frac{\partial A^z}{\partial t} + \frac{\partial A^t}{\partial z} = \frac{e\gamma(\beta t - z)}{[x^2+y^2+\gamma^2(\beta t - z)^2]^{\frac{3}{2}}}. \tag{4.7}$$

Thus the force experienced by a charge in the hadron H_2, at any fixed time before the arrival of the quark, decreases as m^4/s^2. There are residual interactions which distort the distribution of quarks in hadron H_2, but their effects vanish at high energies. A breakdown of factorisation at order $1/s^2$ is therefore to be expected in perturbation theory and has been demonstrated explicitly in ref. [43]. Note that these effects are due to the long range nature of the vector field. In the realistic case of an incoming

colour neutral hadron there are no long-range colour fields. It is therefore possible that the factorisation property is even better in the full theory than in perturbation theory. In the next lecture we will consider vector boson production, dropping all terms suppressed by powers of s. The QCD improved parton model will provide a valid description of this process.

4.3 Parton luminosities

Since partons only carry a fraction of their parent hadron's momentum the available centre of mass energy of a parton-parton collision is less than the overall hadron-hadron collision energy. A convenient way to quantify this is to define *parton luminosities.* Consider a generic hard process initiated by two hadrons of momenta P_1 and P_2 and $s = (P_1 + P_2)^2$,

$$\sigma(s) = \sum_{i,j} \int_0^1 dx_1 \int_0^1 dx_2 \; f_i(x_1,\mu) f_j(x_2,\mu) \; \hat{\sigma}_{ij}(x_1 P_1, x_2 P_2, \alpha_S(\mu)). \tag{4.8}$$

We may define the parton luminosity as follows:

$$\tau \frac{dL_{ij}}{d\tau} = \frac{1}{1+\delta_{ij}} \int_0^1 dx_1 dx_2 \; [(x_1 f_i(x_1,\mu) \; x_2 f_j(x_2,\mu)) + (1 \leftrightarrow 2)] \delta(\tau - x_1 x_2). \tag{4.9}$$

If $\hat{\sigma}$ depends only on the product $x_1 x_2$ the parton cross section can be written as,

$$\sigma(s) = \sum_{\{ij\}} \int_{\tau_0}^1 \frac{d\tau}{\tau} \left[\frac{1}{s} \frac{dL_{ij}}{d\tau} \right] \left[\hat{s} \hat{\sigma}_{ij} \right] \tag{4.10}$$

where $\hat{s} = x_1 x_2 s$ and the sum now runs over all pairs of partons $\{ij\}$. The first object in square brackets has the dimensions of a cross section. The second object in square brackets is dimensionless and is approximately determined by couplings. Hence knowing the luminosities we can roughly estimate cross sections. As an example we can estimate the cross section for the production of two gluon jets with $p_T > 1$ TeV at $\sqrt{s} = 40$ TeV. We assume that $\sqrt{\hat{s}} = 2$ TeV and from Fig.(21) we find

$$\left[\frac{1}{s} \frac{dL_{ij}}{d\tau} \right] \approx 10^3 \text{pb}. \tag{4.11}$$

The gluon jet cross section can be calculated to be approximately 10 pb after including two powers of $\alpha_S \approx 0.1$.

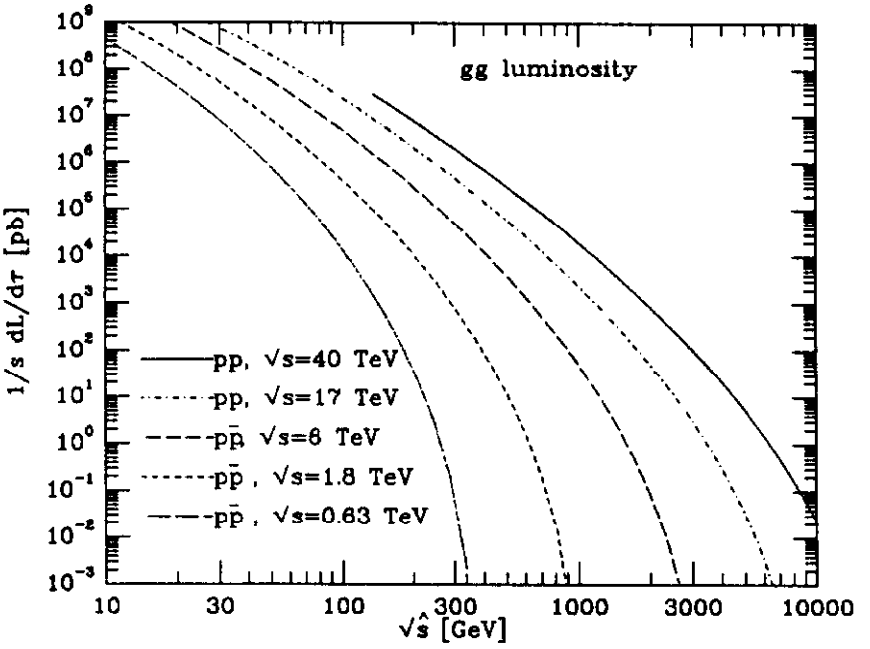

Figure 21: Luminosity plot

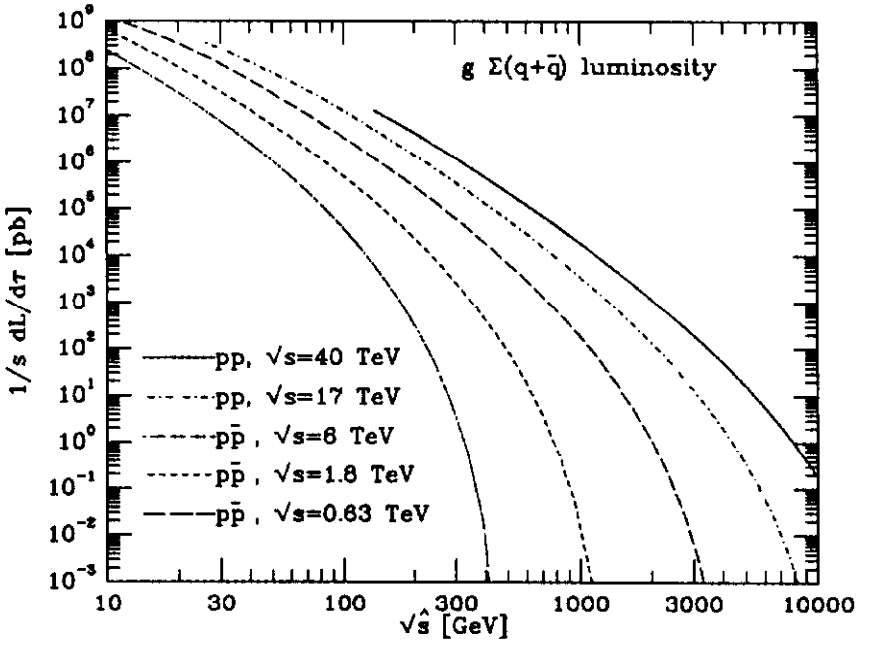

Figure 22: Luminosity plot

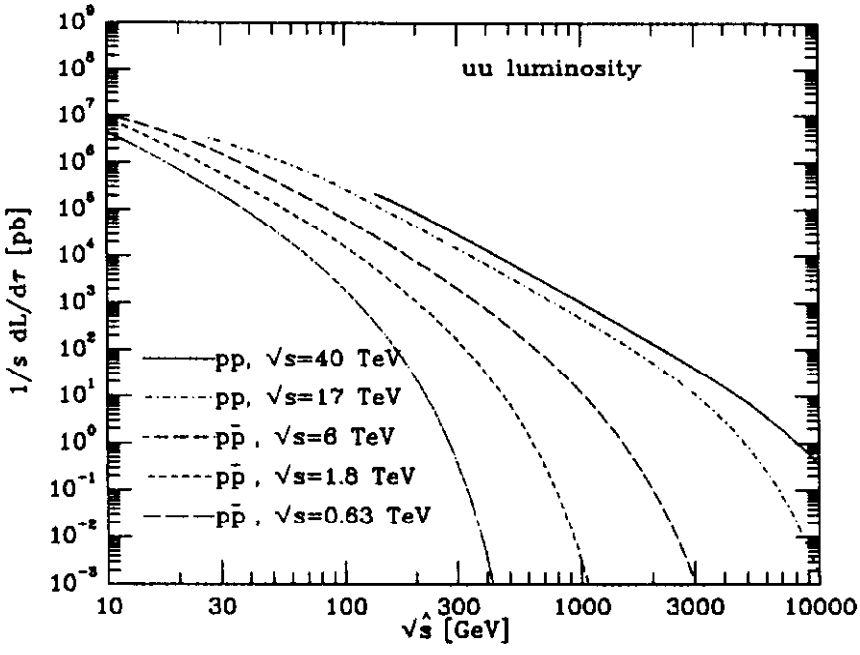

Figure 23: Luminosity plot

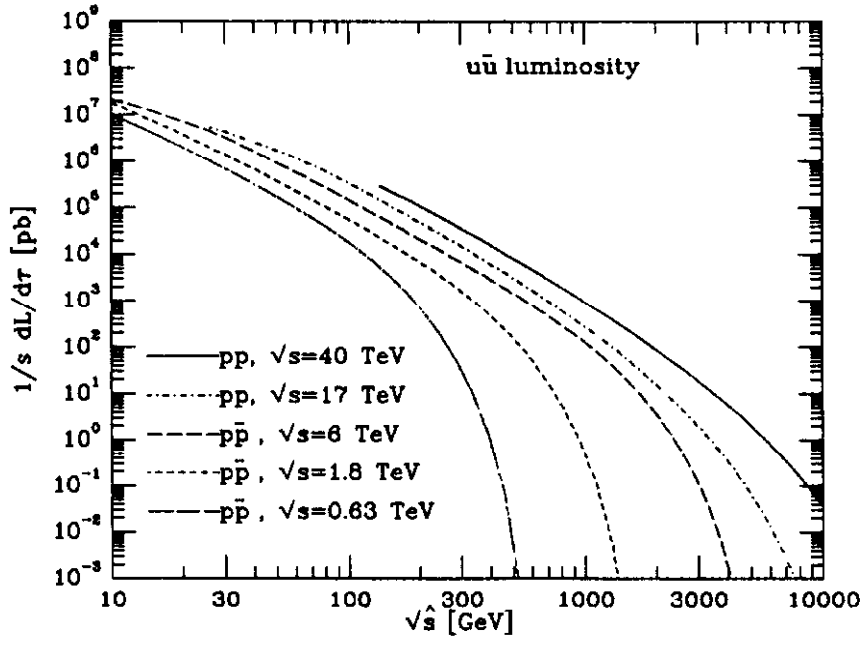

Figure 24: Luminosity plot

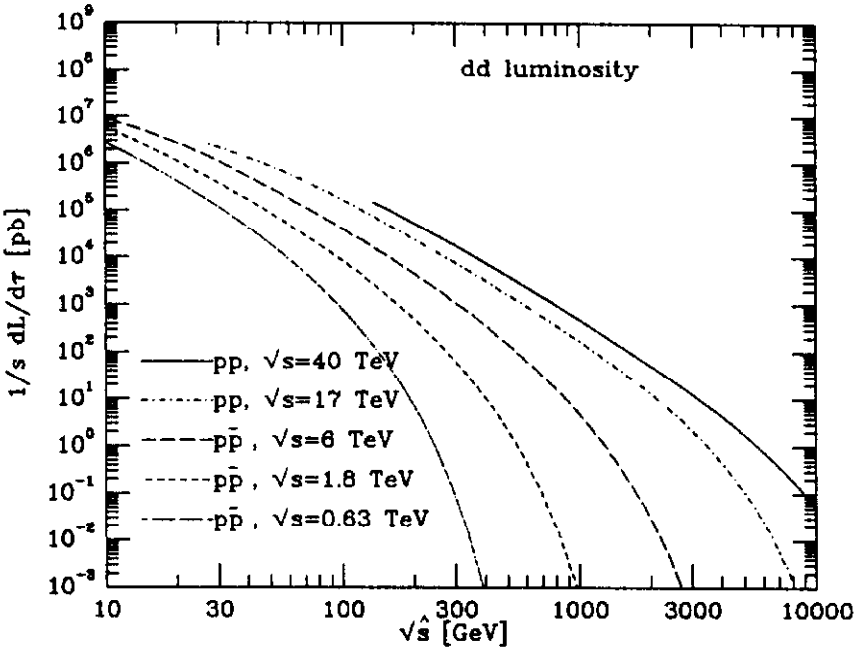

Figure 25: Luminosity plot

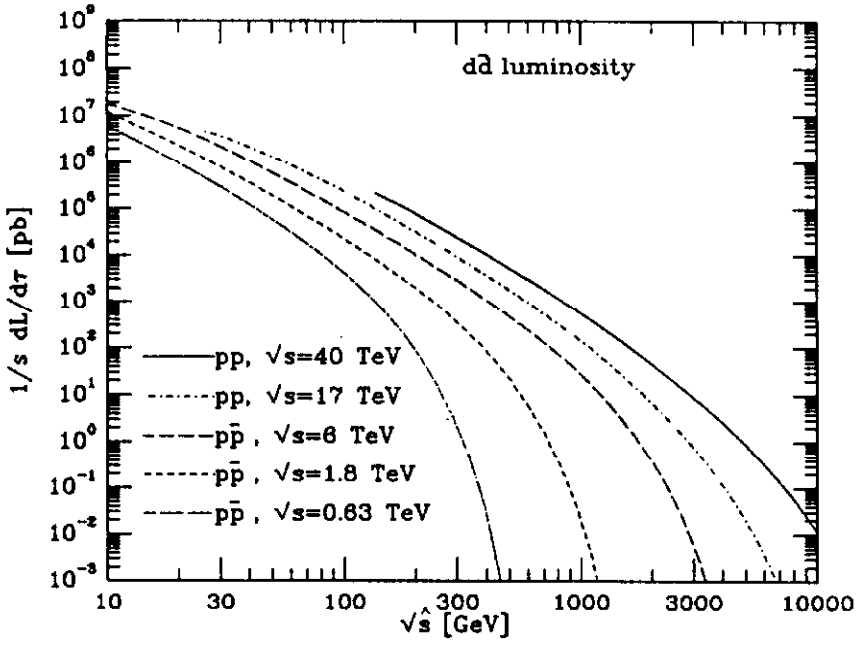

Figure 26: Luminosity plot

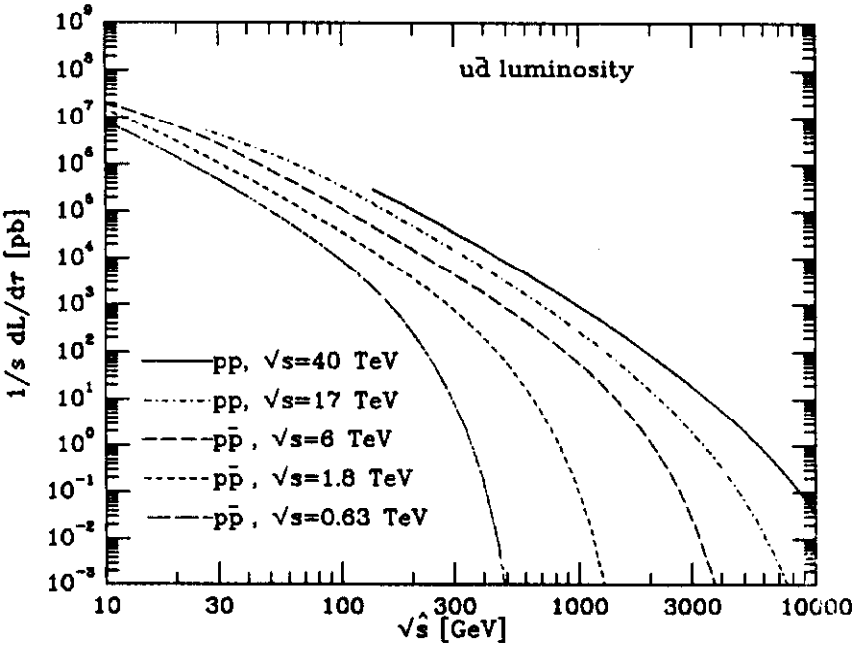

Figure 27: Luminosity plot

5. Large p_T Jet Production in Hadron-Hadron Collisions

The scattering processes $e^+e^- \to e^+e^-$, $e^+e^- \to \gamma\gamma$, ... provide fundamental tests of QED. The analog processes for QCD, $qq \to qq$, $q\bar{q} \to gg$, ... can be studied in the production of large transverse momentum jets in hadron-hadron collisions. After defining some kinematics, we show how the jet inclusive cross section is calculated in the QCD improved parton model. We study the p_T and angular distributions, and compare the theoretical predictions with the experimental data. We extend the discussion to include multijet cross sections, and finally describe the related process of direct photon production.

5.1 Kinematics and jet definition

As described in the previous lecture, the scattering of two hadrons provides two broad band beams of incoming partons. These incoming beams have a spectrum of longitudinal momenta determined by the parton distribution functions. The centre of mass of the parton-parton scattering is normally boosted with respect to the centre of mass of the two incoming hadrons. It is therefore useful to classify the final state in terms of variables which transform simply under longitudinal boosts. For this purpose we introduce the rapidity y, the transverse momentum p_T and the azimuthal angle ϕ. In terms of these variables, the four components of momenta of a particle of mass m may be written as

$$p^\mu = \left(\sqrt{p_T^2 + m^2}\cosh(y), p_T \sin\phi, p_T \cos\phi, \sqrt{p_T^2 + m^2}\sinh(y)\right). \tag{5.1}$$

The rapidity y is therefore defined by

$$y = \frac{1}{2}\ln\left(\frac{E + p_z}{E - p_z}\right), \tag{5.2}$$

and is additive under the restrictive class of Lorentz transformations corresponding to a boost along the z direction. Rapidity differences are boost invariant.

In practice the rapidity is normally replaced by the pseudorapidity η,

$$\eta = -\ln\tan(\frac{\theta}{2}), \tag{5.3}$$

which coincides with the rapidity in the $m \to 0$ limit. It is a more convenient variable experimentally, since the angle θ from the beam direction is measured directly in the detector. It is also standard to use the transverse *energy* rather than the transverse *momentum* for similar reasons. Many methods can be used to define what is meant by a jet. There is no best definition, but one must be sure that both theoretical and experimental analyses use the same definition. A commonly used definition of a jet is a cluster of transverse energy E_T in a cone of size ΔR, where

$$\Delta R = \sqrt{[(\Delta y)^2 + (\Delta \phi)^2]}. \tag{5.4}$$

In the two-dimensional y, ϕ plane, lines of constant ΔR describe a circle around the axis of the jet. The cone size can be chosen at the experimentalist's convenience, and the measured jet cross-section will depend on the value chosen.

5.2 Two-jet cross sections

In QCD, two-jet events result when an incoming parton from one hadron scatters off an incoming parton from the other hadron to produce two high transverse momentum partons which are observed as jets. From momentum conservation the two final state partons are produced with equal and opposite momenta in the subprocess centre-of-mass frame. If only two partons are produced, and the relatively small intrinsic transverse momentum of the incoming partons is neglected, then the two jets will be back-to-back in azimuth and balanced in transverse momentum in the laboratory frame.

For a $2 \to 2$ parton scattering process

$$\text{parton}_i(p_1) + \text{parton}_j(p_2) \to \text{parton}_k(p_3) + \text{parton}_l(p_4), \tag{5.5}$$

described by a matrix element M, the parton cross section is

$$\frac{E_3 E_4 d^6\hat{\sigma}}{d^3p_3 d^3p_4} = \frac{1}{2\hat{s}} \frac{1}{16\pi^2} \overline{\sum} |M|^2 \, \delta^4(p_1 + p_2 - p_3 - p_4), \tag{5.6}$$

All parton processes which contribute in lowest order can be derived from the diagrams shown in Fig.(28) by including other diagrams which are related by crossing. Expressions for the leading order matrix elements squared $\overline{\sum}|M|^2$, averaged and

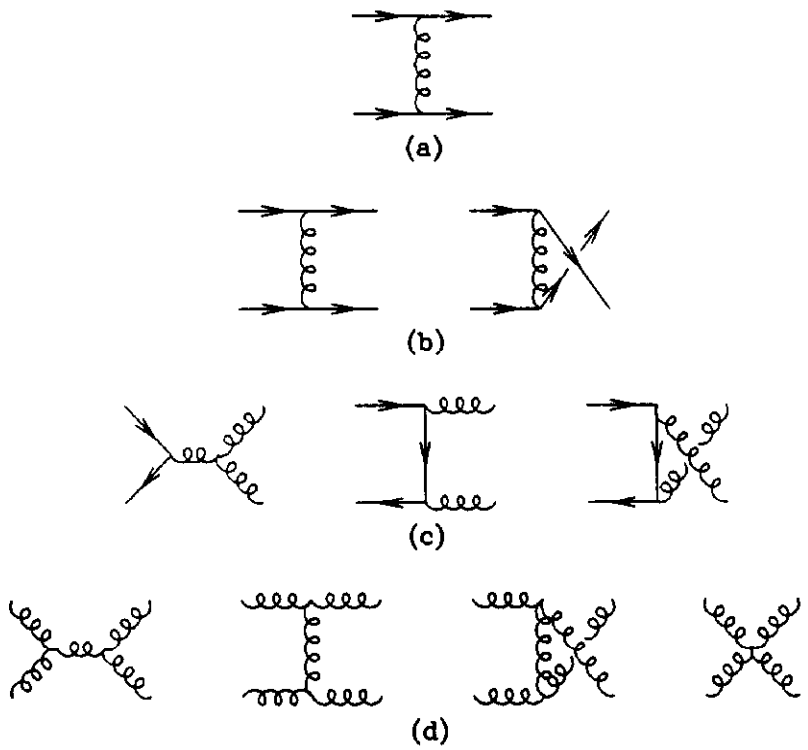

Figure 28: Diagrams for jet production

summed over initial and final state spins and colours are given in Table 3 in the notation $\hat{s} = (p_1 + p_2)^2$, $\hat{t} = (p_1 - p_3)^2$ and $\hat{u} = (p_2 - p_3)^2$.

The two-jet cross section may be written as a sum of terms each representing the contribution to the cross section due to a particular combination of incoming (i, j) and outgoing (k, l) partons. Using Eq.(5.6) the result for the two jet inclusive cross section is,

$$\frac{d^3\sigma}{dy_3 dy_4 dp_T^2} = \frac{1}{16\pi s^2} \sum_{i,j} \sum_{k,l} \frac{f_i(x_1,\mu)}{x_1} \left(\frac{f_j(x_2,\mu)}{x_2}\right) \overline{\sum} |M(ij \to kl)|^2 \frac{1}{1+\delta_{kl}} \qquad (5.7)$$

where the $f_i(x,\mu)$ represent the number distributions for partons of type i ($i = u, \bar{u}, d, \bar{d}, g, \ldots$ etc.), evaluated at momentum scale μ, and y_3 and y_4 represent the laboratory rapidities of the outgoing partons. For massless partons the rapidities

Process	$\overline{\sum}\|M\|^2/g^4$	$\theta^* = \pi/2$
$q\,q' \to q\,q'$	$\frac{4}{9}\,\frac{\hat{s}^2+\hat{u}^2}{\hat{t}^2}$	2.22
$q\,q \to q\,q$	$\frac{4}{9}\,(\frac{\hat{s}^2+\hat{u}^2}{\hat{t}^2}+\frac{\hat{s}^2+\hat{t}^2}{\hat{u}^2})-\frac{8}{27}\,\frac{\hat{s}^2}{\hat{u}\hat{t}}$	3.26
$q\,\overline{q} \to q'\,\overline{q'}$	$\frac{4}{9}\,\frac{\hat{t}^2+\hat{u}^2}{\hat{s}^2}$	0.22
$q\,\overline{q} \to q\,\overline{q}$	$\frac{4}{9}\,(\frac{\hat{s}^2+\hat{u}^2}{\hat{t}^2}+\frac{\hat{t}^2+\hat{u}^2}{\hat{s}^2})-\frac{8}{27}\,\frac{\hat{u}^2}{\hat{s}\hat{t}}$	2.59
$q\,\overline{q} \to g\,g$	$\frac{32}{27}\,\frac{\hat{t}^2+\hat{u}^2}{\hat{t}\hat{u}}-\frac{8}{3}\frac{\hat{t}^2+\hat{u}^2}{\hat{s}^2}$	1.04
$g\,g \to q\,\overline{q}$	$\frac{1}{6}\,\frac{\hat{t}^2+\hat{u}^2}{\hat{t}\hat{u}}-\frac{3}{8}\frac{\hat{t}^2+\hat{u}^2}{\hat{s}^2}$	0.15
$g\,q \to g\,q$	$-\frac{4}{9}\,\frac{\hat{s}^2+\hat{u}^2}{\hat{s}\hat{u}}+\frac{\hat{u}^2+\hat{s}^2}{\hat{t}^2}$	6.11
$g\,g \to g\,g$	$\frac{9}{2}\,(3-\frac{\hat{t}\hat{u}}{\hat{s}^2}-\frac{\hat{s}\hat{u}}{\hat{t}^2}-\frac{\hat{s}\hat{t}}{\hat{u}^2})$	30.4

Table 3: The invariant matrix elements squared $\overline{\sum}|M|^2$ for two-to-two parton subprocesses with massless partons. The colour and spin indices are averaged (summed) over initial (final) states.

and pseudorapidities may be used interchangeably. The Kronecker delta function introduces the statistical factor necessary for identical final state partons. If we assume that the detector and jet algorithm are 100% efficient, the rapidities and p_T of the outgoing jets may be identified with those of the outgoing partons.

We now consider the kinematics of the two produced jets in detail. The laboratory rapidity ($y_{\rm boost}$) of the two-parton system and the equal and opposite rapidities ($\pm y^*$) of the two jets in the parton-parton centre-of-mass system are given in terms of the observed rapidities by:

$$y_{\rm boost} = (y_3 + y_4)/2, \quad y^* = (y_3 - y_4)/2. \tag{5.8}$$

For a massless parton the centre of mass scattering angle θ^* is given by,

$$\cos\theta^* = \frac{p_z^*}{E^*} = \frac{\sinh(y^*)}{\cosh(y^*)} = \tanh(\frac{y_3 - y_4}{2}), \tag{5.9}$$

where $y^* = y_3 - y_{\rm boost}$. The measurement of the rapidity difference of the two jets in the laboratory frame determines the subprocess centre of mass scattering angle θ^*.

The longitudinal momentum fractions of the incoming partons x_1 and x_2 in Eq.(5.7) are given in terms of p_T, y_3 and y_4 by momentum conservation:

$$x_1 = x_T e^{y_{\rm boost}} \cosh(y^*), \quad x_2 = x_T e^{-y_{\rm boost}} \cosh(y^*), \quad y_{\rm boost} = \frac{1}{2}\ln\frac{x_1}{x_2}, \tag{5.10}$$

where $x_T = 2p_T/\sqrt{s}$. Lastly, the invariant mass of the jet-jet system can be written as,

$$M_{JJ}^2 = \hat{s} = 4p_T^2 \cosh^2(y^*). \tag{5.11}$$

Given a knowledge of the parton distributions from deep inelastic scattering experiments, Eq.(5.7) may be used to make leading order QCD predictions for jet production in hadron-hadron collisions. For example, the inclusive jet cross section at the parton level may be obtained by integrating Eq.(5.6) over the momentum of one of the jets.

$$\frac{E d^3\hat{\sigma}}{d^3p} \equiv \frac{d^3\hat{\sigma}}{dy d^2p_T} = \frac{1}{2\hat{s}}\frac{1}{8\pi^2}\overline{\sum}|M|^2\,\delta(\hat{s}+\hat{t}+\hat{u}), \tag{5.12}$$

where $\hat{t}$ and $\hat{u}$ are fixed by $\hat{s}$ and the centre of mass scattering angle,

$$\begin{aligned} \hat{t} &= -\frac{\hat{s}}{2}(1-\cos\theta^*) \\ \hat{u} &= -\frac{\hat{s}}{2}(1+\cos\theta^*). \end{aligned} \tag{5.13}$$

Again assuming that the detector and jet algorithm are 100% efficient, so that $p_{\rm jet}^\mu = p_{\rm parton}^\mu$, the single jet inclusive cross section is obtained from Eq.(5.12) by folding in the parton distribution functions:

$$\begin{aligned} \frac{E_J d^3\hat{\sigma}}{d^3p_J} &= \frac{1}{16\pi^2 s}\sum_{i,j,k,l=q,g}\int_0^1 \frac{dx_1}{x_1}\frac{dx_2}{x_2}\, f_i(x_1,\mu) f_j(x_2,\mu) \\ &\quad \overline{\sum}|M(ij\to kl)|^2 \frac{1}{1+\delta_{kl}}\delta(\hat{s}+\hat{t}+\hat{u}). \end{aligned} \tag{5.14}$$

Note that this result corresponds to massless quarks and gluons and that no distinction is made between quark and gluon jets.

5.3 Comparison with experiment

Although large p_T jet production has been studied at different machines over a period of many years, the definitive data are from the high energy $p\bar{p}$ colliders, i.e. from the UA1 and UA2 collaborations at the CERN $p\bar{p}$ collider ($\sqrt{s}$ = 546 GeV and 630 GeV) and from the CDF collaboration at the FNAL Tevatron collider ($\sqrt{s}$ = 1.8 TeV). It appears that only at these very high collision energies does the identification and measurement of large p_T jets become relatively unambiguous. At lower energies it is difficult to separate the jets from the other 'underlying' hadrons in the event.

Two quantities are particularly useful for comparing theory with experiment. The first is the jet p_T distribution, obtained from the inclusive cross section by

$$\frac{Ed^3\sigma}{d^3p} \equiv \frac{d^3\sigma}{d^2p_T dy} \longrightarrow \frac{1}{2\pi E_T}\frac{d^2\sigma}{dE_T d\eta} \tag{5.15}$$

where the third term follows if we assume that the jets are approximately massless.

Fig.(29) shows the jet E_T distribution in $p\bar{p}$ collisions at $\sqrt{s}$ = 1.8 TeV, from the CDF collaboration. The curve is the QCD prediction, calculated in next-to-leading order (i.e. $O(\alpha_S^3)$) by S. D. Ellis et al. [44] and using the HMRSB parton distributions from reference [38]. The next-to-leading order contributions considerably reduce the dependence on the scale parameter μ, and allow a more precise treatment of effects due to the finite width of the jet. The agreement is excellent, especially considering that there are essentially no free parameters in the theoretical prediction. Note that at this energy about half the cross section comes from quark-gluon scattering, the other half coming from gluon-gluon scattering at the lower E_T end, and quark-(anti)quark scattering at the high E_T end.

The second quantity of interest is the jet angular distribution. In the parton-parton centre of mass, the angular distribution is sensitive to the form of the $2 \rightarrow 2$ matrix elements. The differential cross section for a jet pair of mass M_{JJ} produced at an angle θ^* to the beam direction in the jet-jet centre of mass can readily be obtained

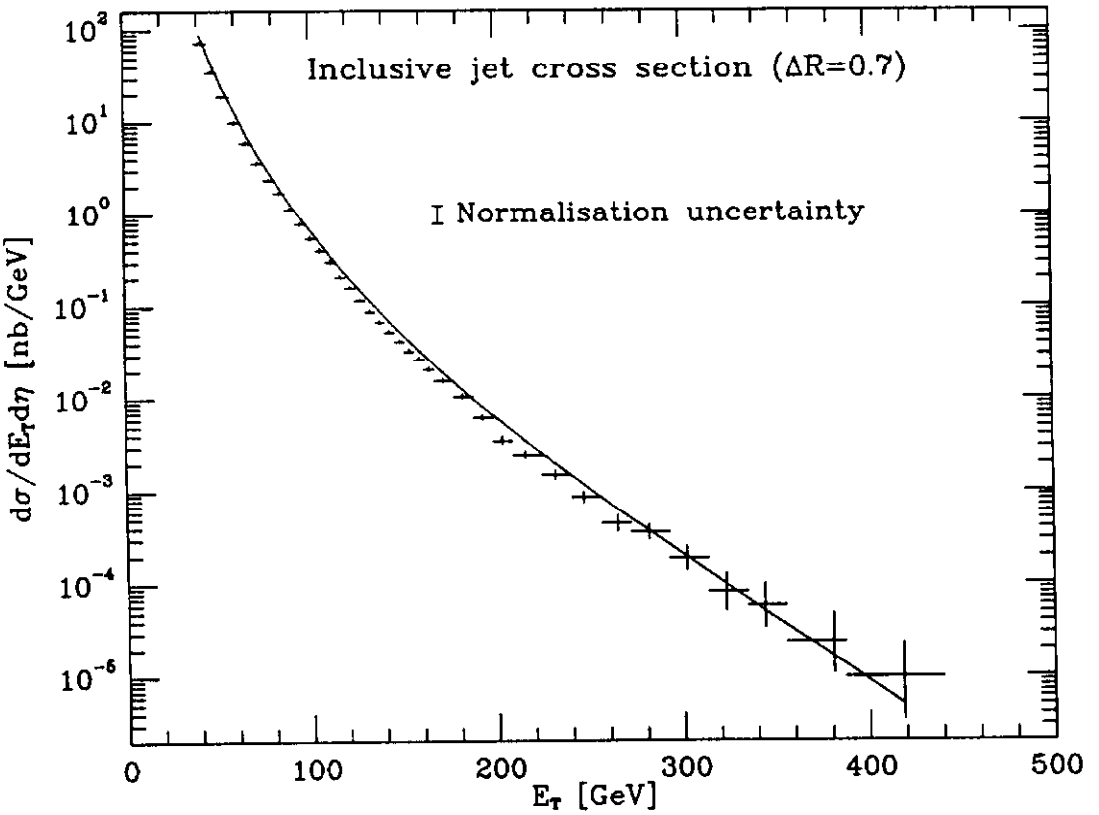

Figure 29: Jet E_T distribution from the CDF collaboration, compared with a next-to-leading order QCD prediction from [44]

from Eq.(5.7) using the transformation

$$dp_T^2 dy_3 dy_4 \equiv \frac{s}{2} dx_1 dx_2 d\cos\theta^* \tag{5.16}$$

to give

$$\begin{aligned} \frac{d^2\sigma}{dM_{JJ}^2 d\cos\theta^*} &= \sum_{i,j=q,g} \int_0^1 dx_1 dx_2 \; f_i(x_1,\mu) f_j(x_2,\mu) \; \delta(x_1 x_2 s - M_{JJ}^2) \; \frac{d\hat{\sigma}^{ij}}{d\cos\theta^*} \\ &= \sum_{\{ij\}} \frac{\tau_J}{s} \; \frac{dL_{ij}(\tau_J,\mu)}{d\tau_J} \frac{d\hat{\sigma}^{ij}}{d\cos\theta^*}, \end{aligned} \tag{5.17}$$

with $\tau_J = M_{JJ}^2/s$ and

$$\frac{d\hat{\sigma}^{ij}}{d\cos\theta^*} = \sum_{k,l} \frac{1}{32\pi M_{JJ}^2} \overline{\sum} |M(ij \to kl)|^2 \frac{1}{1+\delta_{kl}} \tag{5.18}$$

Note that for each subprocess the $d\hat{\sigma}/d\cos\theta^*$ is symmetrised in $\hat{t}$ and $\hat{u}$ (unless $k \equiv l$). Thus, for example,

$$\frac{d\hat{\sigma}^{u\bar{d}}}{d\cos\theta^*} = \frac{\pi\alpha_S^2}{2M_{JJ}^2} \frac{4}{9} \left[\frac{4+(1+\cos\theta^*)^2}{(1-\cos\theta^*)^2} + \frac{4+(1-\cos\theta^*)^2}{(1+\cos\theta^*)^2} \right]. \tag{5.19}$$

Numerically the most important subprocesses are $gg \to gg$, $gq \to gq$ and $q\bar{q} \to q\bar{q}$. For each of these, the θ^* distributions have the familiar Rutherford scattering behaviour at small angle, characteristic of the exchange of a vector boson in the t-channel:

$$\frac{d\hat{\sigma}}{d\cos\theta^*} \sim \frac{1}{\sin^4(\frac{\theta^*}{2})}. \tag{5.20}$$

It is convenient to plot the data in terms of the variable χ, which removes the Rutherford singularity [48],

$$\chi = \frac{1+\cos\theta^*}{1-\cos\theta^*}. \tag{5.21}$$

In the small angle limit ($\chi \to \infty$) the cross section differential in χ is then

$$\frac{d\hat{\sigma}}{d\chi} \sim \text{constant}. \tag{5.22}$$

Data on the angular distribution from the CDF collaboration are shown in Fig.(30), with the leading order QCD prediction. Again, there is excellent agreement. Note that these data automatically rule out certain other quark scattering mechanisms. For example, a model in which quarks scatter by exchanging a *scalar* gluon would give a less singular behaviour ($\sin^{-2}(\theta^*/2)$) at small angle.

It is also interesting to note that the angular dependences of the dominant subprocesses are very similar. Fig.(31) shows the $\cos\theta^*$ dependence of the $qg \to qg$ and $q\bar{q} \to q\bar{q}$ subprocesses normalised to $gg \to gg$. These ratios are evidently rather constant at the numerical values 4/9 and $(4/9)^2$ respectively. This can be understood in terms of the colour structure of the Feynman diagrams. Thus to a good approximation the $gg \to gg$ subprocess can be used as the 'universal' subprocess in the result given in Eq.(5.17), i.e. the angular dependence effectively factors out leaving

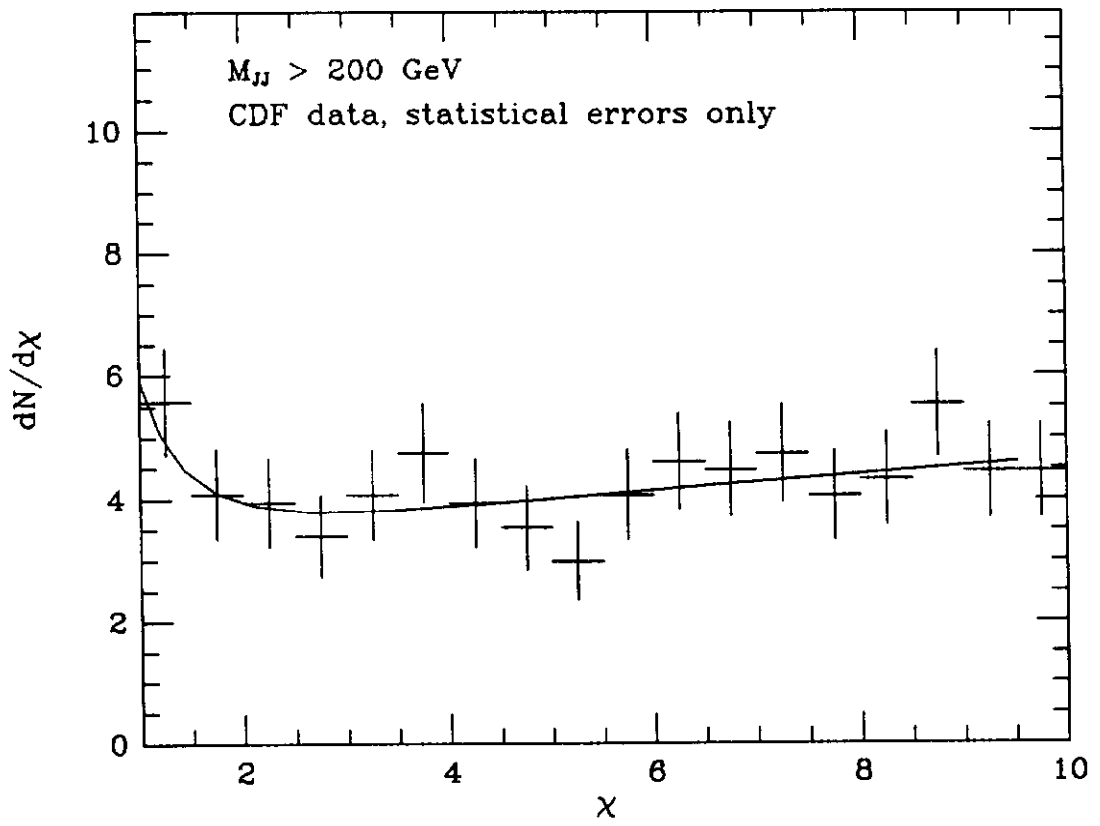

Figure 30: χ distribution from the CDF collaboration compared with the leading order QCD prediction

a convolution of parton distributions. This is called the *single effective subprocess approximation* [48].

5.4 Multijet production

As long as the jets are required to be well separated in phase space, multijet cross sections can be calculated from scattering processes involving many quarks and gluons in the final state. In this way one defines an n-jet cross section σ^n for producing n jets which satisfy, say, $p_T^i > p_T^{min}$, $|\eta^i| < \eta^{max}$ and $\Delta R_{ij} > \Delta R_{min}$ for $i,j = 1,...,n$. In leading order QCD, these cross sections are calculated at the parton level from 'tree-level' Feynman diagrams, i.e. diagrams without any internal loops. The general

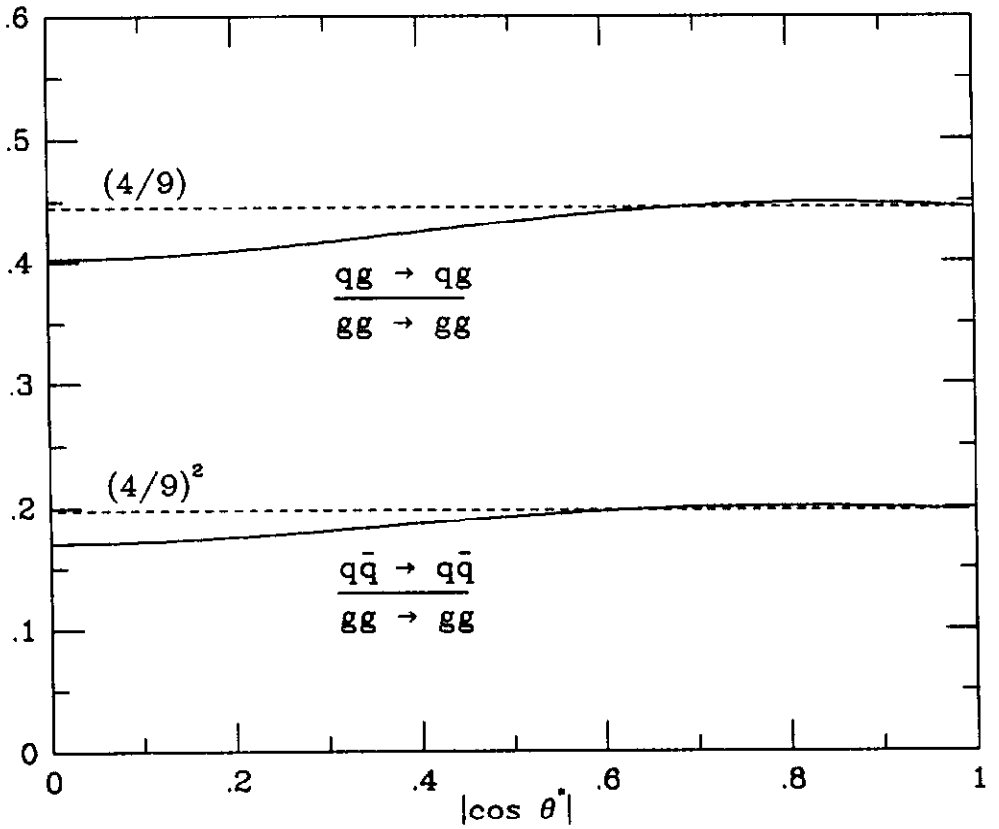

Figure 31: Quark-antiquark and quark-gluon angular distributions, normalised to that for $gg \to gg$

expression is again obtained from Eq.(4.8):

$$\sigma^n = \sum_{i,j,k_1,\ldots,k_n=q,g} \int_0^1 dx_1 dx_2 \; f_i(x_1,\mu) f_j(x_2,\mu) \; \hat{\sigma}^{ij\to k_1,\ldots,k_n}. \qquad (5.23)$$

The matrix elements for all the $2 \to 2,3,4,5$ QCD processes are known exactly [45]. Since each n-jet cross section is proportional to α_S^n, the cross sections fall roughly geometrically with increasing n.

Events with three jets at large transverse energy are described in QCD by amplitudes with two incoming partons and three outgoing partons. Very elegant results for the two-to-three parton scattering processes have been given by Berends et al. [46].

For a complete description it is sufficient to consider the following four processes.

$$\begin{aligned}
(A)\quad & q(p_1)+q'(p_2) \;\rightarrow\; q(p_3)+q'(p_4)+g(k)\\
(B)\quad & q(p_1)+q(p_2) \;\rightarrow\; q(p_3)+q(p_4)+g(k)\\
(C)\quad & q(p_a)+\overline{q}(p_b) \;\rightarrow\; g(p_1)+g(p_2)+g(p_3)\\
(D)\quad & g(p_1)+g(p_2) \;\rightarrow\; g(p_3)+g(p_4)+g(p_5).
\end{aligned} \tag{5.24}$$

The momentum assignments for the partons are given in brackets. All other matrix elements for two-to-three parton amplitudes may be obtained by crossing from the above four processes.

The matrix elements squared for the processes $(A-D)$, averaged (summed) over the initial (final) colours and spins are given below. We have set the masses of the quarks equal to zero. With the momentum assignments of Eq.(5.24) the matrix element [47] for process (A) is,

$$\overline{\sum}\left|M^{(A)}\right|^2 = \frac{g^4 C_F}{N}\left(\frac{s^2+s'^2+u^2+u'^2}{2tt'}\right)\left(2C_F\Big([14]+[23]\Big)+\frac{1}{N}[12;34]\right). \tag{5.25}$$

The kinematic variables are defined as follows,

$$\begin{aligned}
& s=(p_1+p_2)^2,\;\; t=(p_1-p_3)^2,\;\; u=(p_1-p_4)^2,\\
& s'=(p_3+p_4)^2,\;\; t'=(p_2-p_4)^2,\;\; u'=(p_2-p_3)^2.
\end{aligned} \tag{5.26}$$

For compactness of notation we have introduced the eikonal factor $[ij]$ which is defined as,

$$[ij] \equiv \frac{g^2 p_i.p_j}{p_i.k\; k.p_j}. \tag{5.27}$$

We have also defined the following sum of eikonal terms,

$$[12;34] = 2[12]+2[34]-[13]-[14]-[23]-[24]. \tag{5.28}$$

Note that this combination is free from collinear singularities. In Eq.(5.25) the dependence on the $SU(N)$ colour group is shown explicitly, $(C_A = N = 3, C_F = 4/3)$.

In the same notation the result for process (B) with four identical quarks [47] may be written,

$$\begin{aligned}\overline{\sum}\left|M^{(B)}\right|^2 &= \frac{g^4C_F}{N}\left(\frac{s^2+s'^2+u^2+u'^2}{2tt'}\right)\left(2C_F([14]+[23])+\frac{1}{N}[12;34]\right)\\ &+ \frac{g^4C_F}{N}\left(\frac{s^2+s'^2+t^2+t'^2}{2uu'}\right)\left(2C_F([13]+[24])+\frac{1}{N}[12;34]\right)\\ &- \frac{2g^4C_F}{N^2}\left(\frac{(s^2+s'^2)(ss'-tt'-uu')}{4tt'uu'}\right)\left(2C_F([12]+[34])+\frac{1}{N}[12;34]\right).\end{aligned} \tag{5.29}$$

To write the results for the remaining two processes we introduce a compact notation for the dot product of two momenta,

$$\{ij\} \equiv p_i \cdot p_j. \tag{5.30}$$

Using the momentum assignments of Eq.(5.24) the result for process (C) may be written as [46],

$$\begin{aligned}\overline{\sum}\left|M^{(C)}\right|^2 &= \frac{g^6(N^2-1)}{4N^4}\left(\sum_{i=1}^{3}\frac{\{ai\}\{bi\}(\{ai\}^2+\{bi\}^2)}{\{a1\}\{a2\}\{a3\}\{b1\}\{b2\}\{b3\}}\right)\\ &\times\left[\{ab\}+N^2\left(\{ab\}-\sum_P\frac{\{a1\}\{b2\}+\{a2\}\{b1\}}{\{12\}}\right)\right.\\ &\left.+\frac{N^4}{\{ab\}}\left(\sum_P\frac{\{a3\}\{b3\}(\{a1\}\{b2\}+\{a2\}\{b1\})}{\{23\}\{31\}}\right)\right].\end{aligned} \tag{5.31}$$

The sums run over the three cyclic permutations P of the momentum labels of the final state gluons.

Using the momentum labels of Eq.(5.24) the result for process (D) is [46],

$$\overline{\sum}\left|M^{(D)}\right|^2 = \frac{g^6N^3}{240(N^2-1)}\left[\sum_P\{12\}^4\right]\left[\sum_P\{12\}\{23\}\{34\}\{45\}\{51\}\right]\left(\prod_{i<j}\{ij\}\right)^{-1}. \tag{5.32}$$

The sums run over the 120 permutations of the momentum labels.

These matrix elements display the typical bremsstrahlung structure with the emission of soft and collinear gluons predominating. This is particularly clear from the

form of the result given in Eqs.(5.25,5.29) where the dominant contributions come from the region in which the eikonal factors are large. From the tree graph results one can also show that the same effective structure function which is relevant for two-jet production is also to a very good approximation valid for three-jet production [49].

For three final-state (massless) partons the final-state parton configuration, at fixed centre of mass energy, is specified by five independent variables. Two variables are required to specify how the available energy is shared between the three final-state partons, and two variables serve to fix the orientation of the three-jet system with respect to the axis defined by the colliding partons. The last variable is an overall azimuthal angle. If x_3, x_4, and x_5 are the energies of the outgoing partons scaled such that $x_3 + x_4 + x_5 = 2$ and ordered such that $x_3 > x_4 > x_5$ and θ_i is the angle between parton i and the beam direction, then the subprocess differential cross section can be written using the three particle massless phase space of Eq.(2.6):

$$\frac{d^4\hat{\sigma}}{dx_3 dx_4 d\cos\theta_1 d\psi} = \frac{1}{(1024\pi^4)}\overline{\sum}|M|^2 . \tag{5.33}$$

In Eq.(5.33) the variable ψ is the angle between the plane containing jet-2 and jet-3 and the plane containing jet-1 and the axis defined by the incoming partons.

There is again excellent agreement between the above theoretical predictions and the experimental data. As an example, Fig.(32) shows the distribution in the variable x_3 measured by the CDF collaboration. The solid line is the prediction from QCD, based on the $2 \rightarrow 3$ parton scattering amplitudes, and the dashed line is the prediction from phase space alone. The data clearly favour the former.

5.5 Direct photon production

High transverse momentum direct photon production and high transverse momentum jet production are two closely related phenomena. From an experimental point of view, the study of direct photon production has several advantages with respect to the study of jets: the energy resolution of the electromagnetic calorimeter is generally better for photons than it is for hadrons, and systematic uncertainties on the photon energy scale are smaller. Furthermore, since photons do not fragment, the direction and energy of photons is straightforwardly measured in the calorimeter without the need for a jet algorithm which is required to reconstruct a jet. Only the relatively

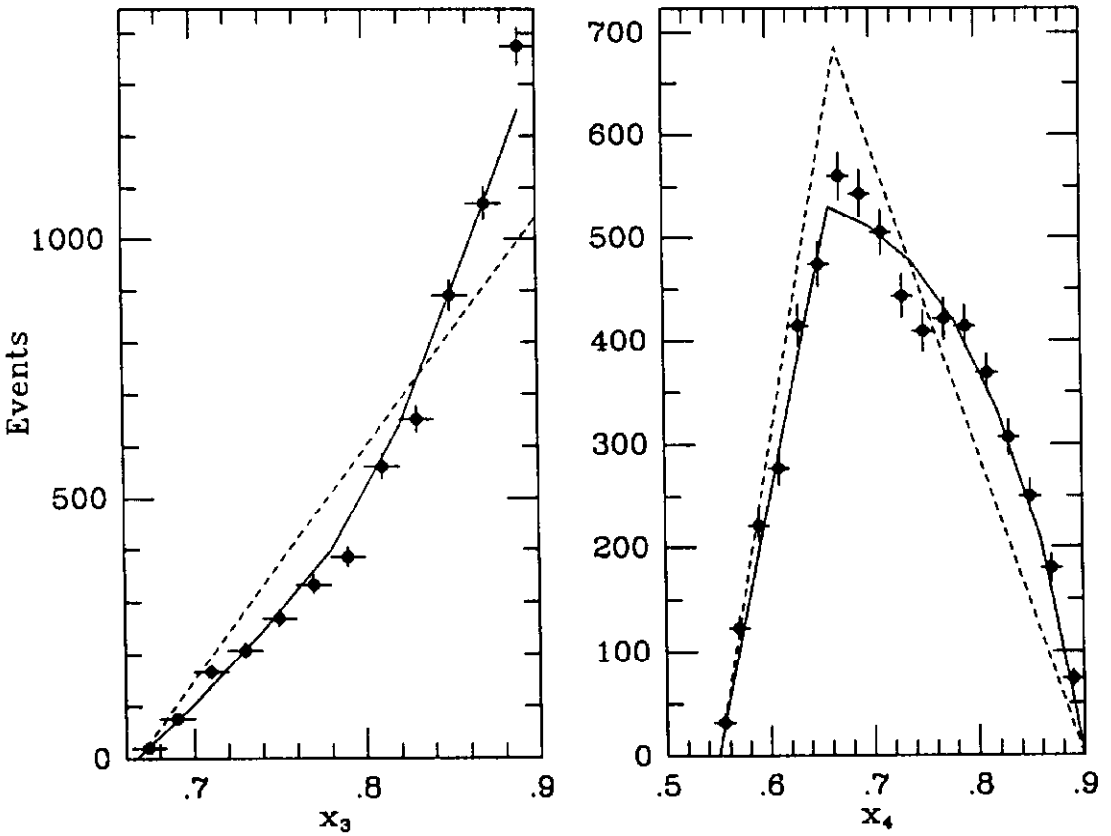

Figure 32: Distribution in the variable x_3 and x_4 in a sample of three jet events, as measured by the CDF collaboration. The solid, dashed lines are the predictions from QCD, phase space respectively

low rate for the production of direct photons and the non-negligible background from jet production processes have limited the usefulness of the direct photons for making quantitative QCD tests.

The leading order subprocesses are (a) the annihilation process $q\bar{q} \rightarrow \gamma g$ and (b) the Compton process $qg \rightarrow \gamma q$ shown in Fig.(33) The invariant matrix elements squared are given in Table 4. Depending on the nature of the colliding hadrons and on the values of $\sqrt{s}$ and $p_T(\equiv p_T^\gamma)$, either of these two subprocesses can dominate. For example, in proton-proton or proton-nucleus collisions at medium p_T the Compton process dominates while in proton-antiproton collisions at high p_T the annihilation process is more important.

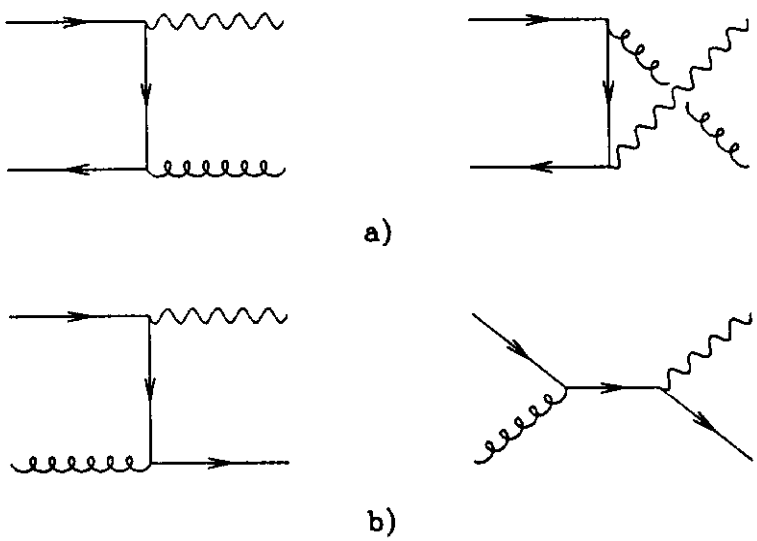

Figure 33: Diagrams for direct photon or vector boson production at large p_T.

Process	$\overline{\sum}\|M\|^2/(g^2e_q^2)$
$q\,\bar{q} \to \gamma^*\,g$	$\frac{(N^2-1)}{N^2}\,\frac{t^2+u^2+2s(s+t+u)}{tu}$
$g\,q \to \gamma^*\,q$	$-\frac{1}{N}\,\frac{s^2+u^2+2t(s+t+u)}{su}$

Table 4: Lowest order processes for virtual photon production. The colour and spin indices are averaged (summed) over initial (final) states. For a real photon $(s+t+u)=0$.

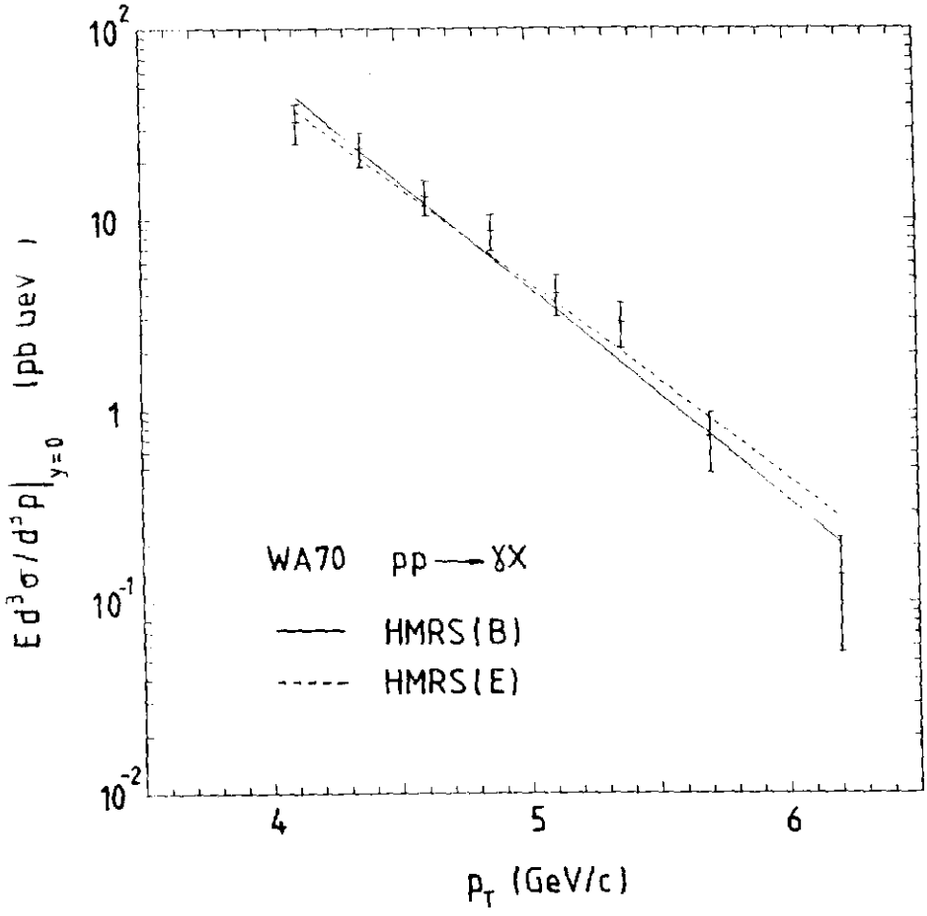

gure 34: Direct photon p_T distribution measured by the WA70 collaboration. The rves are next-to-leading order QCD calculations, as described in the text

All direct photon data show good agreement with QCD over a large energy range. he most *precise* data is from the WA70 collaboration [50]. Fig.(34) shows WA70 ata on $pp \to \gamma X$ at $\sqrt{s} = 23$ GeV. The curves are the fully-corrected QCD cross ections, based on the next-to-leading order calculation of Aurenche et al. [51], using he latest HMRS(E,B) parton distributions [38]. In fact the gluon distributions in hese two sets are chosen to fit the WA70 data.

6. The Production of Vector Bosons in Hadronic Collisions

In this lecture we review the physics of vector boson production in hadron-hadron collisions. We begin by discussing the production of lepton pairs by quark-antiquark annihilation into a virtual photon – the Drell-Yan process. After a brief review of the standard electroweak model, we next discuss the phenomenology of W, Z production in $p\bar{p}$ collisions, with special emphasis on perturbative QCD effects.

6.1 The Drell-Yan mechanism

The cross section for quark-antiquark annihilation to a lepton pair via an intermediate massive photon is easily obtained from the $e^+e^- \to q\bar{q}$ cross section presented in the second lecture, Eq.(2.3):

$$\sigma(q\bar{q} \to e^+e^-) = \frac{4\pi\alpha^2}{3\hat{s}}\frac{1}{N}Q_k^2. \tag{6.1}$$

Note that the time-reversed process, $q\bar{q} \to e^+e^-$ is smaller by a colour factor of $1/N^2$ because of the averaging over the colours of the initial quarks. The differential cross section for the production of a lepton pair of mass M is therefore given by

$$\frac{d\hat{\sigma}}{dM^2} = \frac{\hat{\sigma}_0}{N}Q_k^2\delta(\hat{s}-M^2), \quad \hat{\sigma}_0 = \frac{4\pi\alpha^2}{3M^2}. \tag{6.2}$$

The overall colour factor of $1/N$ is due to the fact that only when the colour of the quark matches with the colour of the antiquark can the annihilation into a colour singlet final state take place. In the centre-of-mass frame of the two hadrons the components of momenta of the incoming partons may be written as

$$\begin{aligned} p_1 &= \frac{\sqrt{s}}{2}(x_1,0,0,x_1) \\ p_2 &= \frac{\sqrt{s}}{2}(x_2,0,0,-x_2). \end{aligned} \tag{6.3}$$

The square of the parton centre-of-mass energy $\hat{s}$ is related to the corresponding hadronic quantity by $\hat{s} = x_1x_2s$. Using Eq.(4.1), the parton model cross section for this process can be written as

$$\frac{d\sigma}{dM^2} = \frac{\sigma_0}{N}\int_0^1 dx_1dx_2\delta(x_1x_2s-M^2)\Big[\sum_k Q_k^2(q_k(x_1,\mu)\bar{q}_k(x_2,\mu)+[1\leftrightarrow 2])\Big]. \tag{6.4}$$

Apart from the mild logarithmic behaviour in the distribution functions, the lepton pair cross section exhibits *scaling* in the variable $\tau = M^2/s$:

$$\frac{M^3 d\sigma}{dM} = \frac{8\pi\alpha^2\tau}{3N}\int_0^1 dx_1 dx_2 \delta(x_1x_2-\tau)\Big[\sum_k Q_k^2(q_k(x_1,\mu)\bar{q}_k(x_2,\mu)+[1\leftrightarrow 2])\Big] \approx F(\tau). \tag{6.5}$$

From Eq.(6.3) the rapidity of the produced lepton pair is found to be $y = 1/2\ln(x_1/x_2)$, and hence

$$x_1 = \sqrt{\tau}e^{y}, \qquad x_2 = \sqrt{\tau}e^{-y}. \tag{6.6}$$

The double differential cross section is therefore

$$\frac{d\sigma}{dM^2 dy} = \frac{\sigma_0}{Ns}\Big[\sum_k Q_k^2(q_k(x_1,\mu)\bar{q}_k(x_2,\mu)+[1\leftrightarrow 2])\Big]. \tag{6.7}$$

with x_1 and x_2 given by Eq.(6.6). By measuring the distribution in rapidity and mass of the produced lepton pair one can in principle measure the quark distribution functions of the incoming hadrons.

In QCD there exists a systematic procedure for calculating the perturbative corrections to all orders. The next-to-leading order corrections are obtained from the graphs shown in Fig.(35):

$$\begin{aligned}\frac{d\sigma}{dM^2} = \frac{\sigma_0}{Ns}\int_0^1 dx_1 dx_2 dz\,\delta(x_1x_2z-\tau)\\ \Bigg\{\Big[\sum_k Q_k^2(q_k(x_1,\mu)\bar{q}_k(x_2,\mu)+[1\leftrightarrow 2])\Big]\Big[\delta(1-z)+\frac{\alpha_S(\mu)}{2\pi}f_q(z)\Big]\\ +\Big[\sum_k Q_k^2(g(x_1,\mu)(q_k(x_2,\mu)+\bar{q}_k(x_2,\mu))+[1\leftrightarrow 2])\Big]\Big[\frac{\alpha_S(\mu)}{2\pi}f_g(z)\Big]\Bigg\},\end{aligned} \tag{6.8}$$

where the correction terms are [52,53]

$$\begin{aligned} f_q(z) &= C_F\left[\delta(1-z)\Big(1+\frac{4\pi^2}{3}\Big)-6-4z+\Big(\frac{3}{1-z}\Big)_+ + 2(1+z^2)\Big(\frac{\ln(1-z)}{1-z}\Big)_+\right]\\ f_g(z) &= \frac{1}{2}\left[(z^2+(1-z)^2)\ln(1-z)+\frac{3}{2}-5z+\frac{9}{2}z^2\right],\end{aligned} \tag{6.9}$$

and the plus distributions are defined as in Eq.(3.27).

The size of the $O(\alpha_S)$ correction depends on the lepton pair mass and on the overall center-of-mass energy. At fixed-target energies and masses the correction is

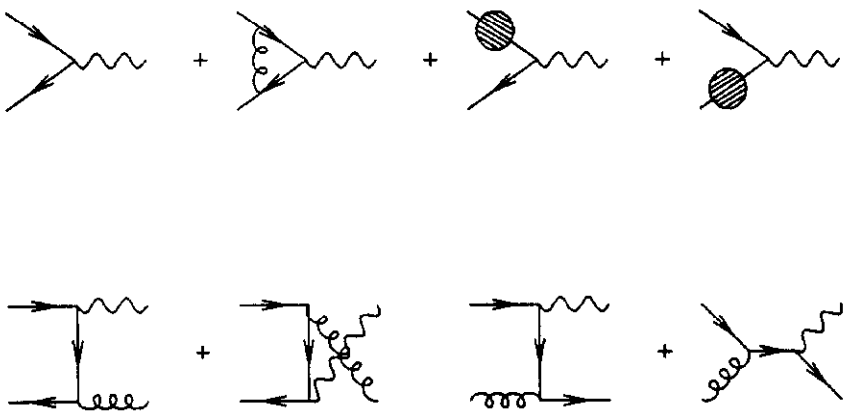

Figure 35: The leading and next-to-leading order diagrams for the Drell-Yan process

large and positive, of order 50% or more. In this regime of relatively large τ, the (negative) contribution from the quark-gluon scattering term is quite small. However at $p\bar{p}$ collider energies, where τ is much smaller, the f_g term is more important and the overall correction is smaller. For W and Z production the $O(\alpha_S)$ correction increases the lowest order cross section by about 25% - 30%.

Several important pieces of information can be obtained from Drell-Yan data. Low mass lepton pair production in high energy hadron collisions is sensitive to the small x behaviour of the parton distributions. In pp or pN collisions the cross section is proportional to the sea quark distribution, $\bar{q}(x,\mu)$. This provides complementary information to deep inelastic data, and in fact Drell-Yan data is used to constrain the sea quark distributions in the latest MRS fits [38]. Fig.(36) shows data from the E605 collaboration [54], compared with the next-to-leading order QCD calculation using

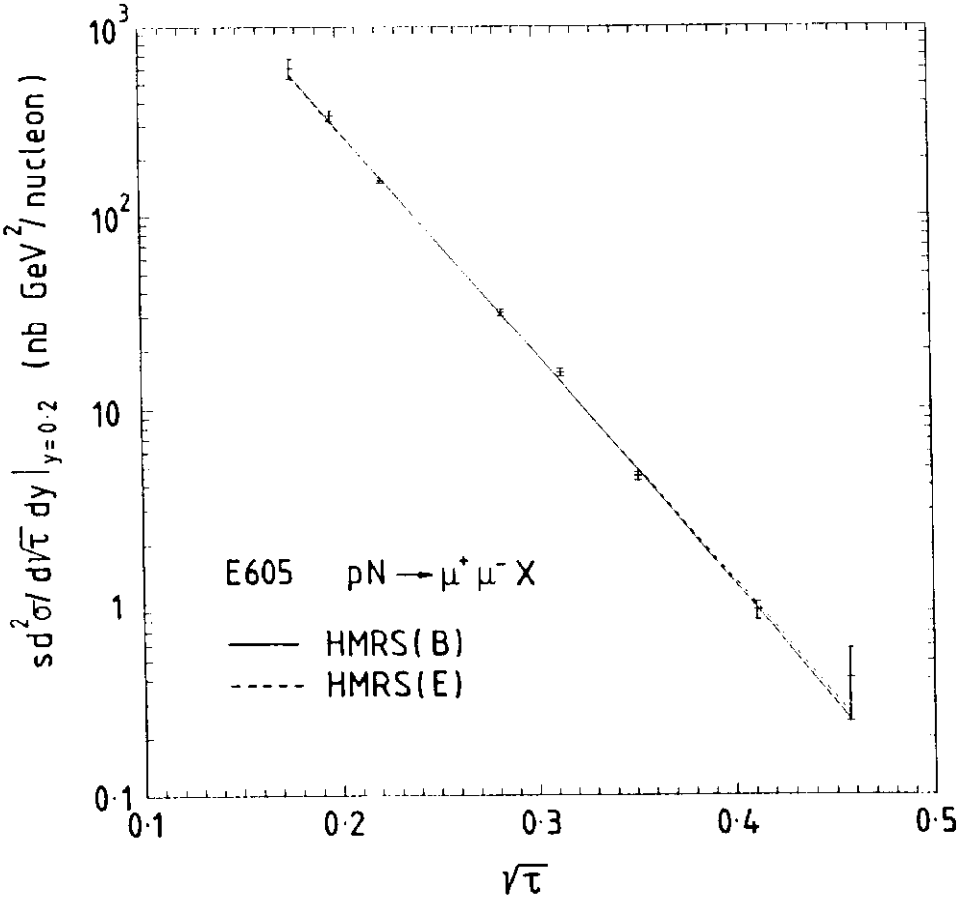

Figure 36: Drell-Yan data from the E605 collaboration with next-to-leading order theoretical predictions

the HMRS(E,B) distributions. Equally important is the fact that the distributions of quarks in *pions* can be extracted from Drell-Yan data in πp and πN collisions. A comprehensive review of Drell-Yan phenomenology can be found in reference [55]. Fig.(37) shows the predictions for lepton pair production at collider energies, including the effects of the Z pole. Fig.(37) also illustrates the influence of higher order corrections.

6.2 W and Z production

The discovery in 1983 of the W and Z weak bosons provided dramatic confirmation of the Glashow-Salam-Weinberg electroweak model. In the remainder of this lecture we discuss the physics of W and Z production in $p\bar{p}$ collisions, starting with an

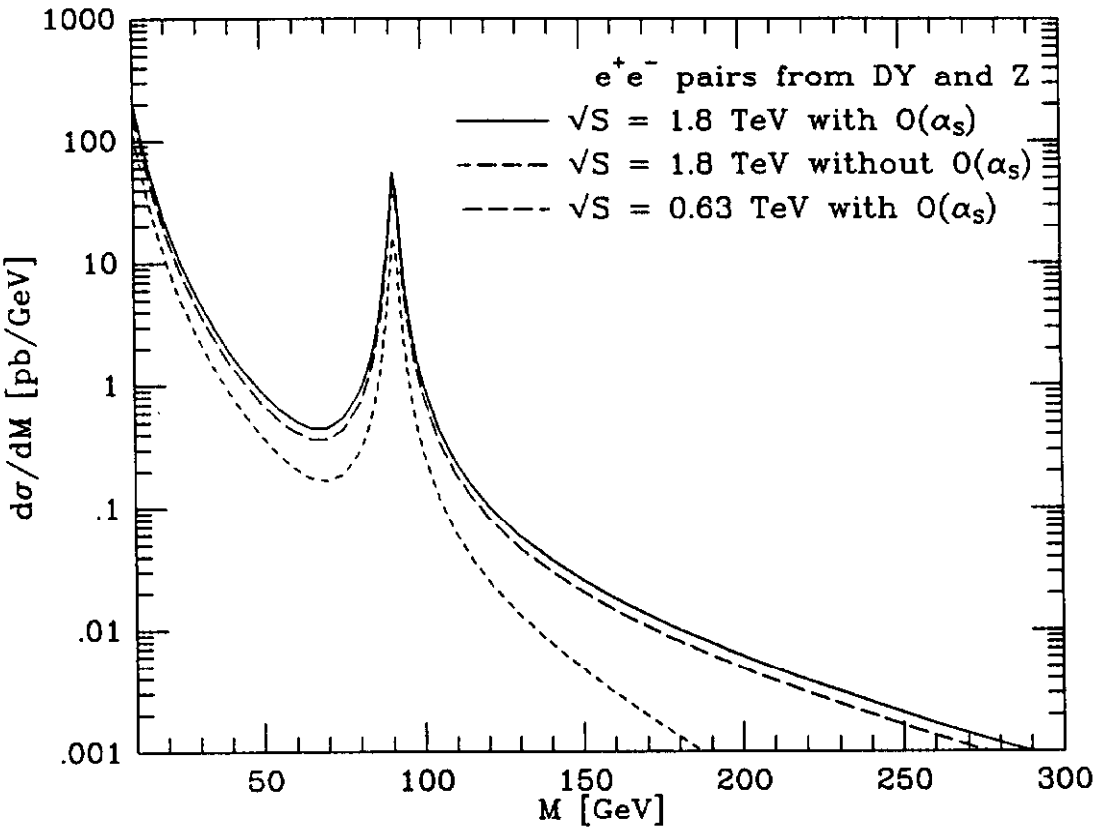

Figure 37: The predicted e^+e^- pair production cross section in $p\bar{p}$ collisions

elementary introduction to the electroweak model.

The Lagrangian for the Glashow-Weinberg-Salam model of the electroweak interactions is

$$\begin{aligned}\mathcal{L}_{GWS} &= -\frac{g_W}{2\sqrt{2}}\sum_i \overline{\psi}_i\gamma^\mu(1-\gamma^5)(T^+W_\mu^+ + T^-W_\mu^-)\psi_i - e\sum_i Q_i\overline{\psi}_i\gamma^\mu\psi_i\mathcal{A}_\mu \\ &\quad -\frac{g_W}{2\cos\theta_W}\sum_i \overline{\psi}_i\gamma^\mu(V_i - A_i\gamma^5)\psi_i Z_\mu, \qquad (6.10)\end{aligned}$$

where θ_W is the Weinberg angle and $g_W = e/\sin\theta_W$. T^+ and T^- are the isospin raising and lowering operators and the vector and axial couplings of the Z are given by

$$V_i = t_{3L}(i) - 2Q_i\sin^2(\theta_W), \quad A_i = t_{3L}(i), \qquad (6.11)$$

where $t_{3L}(i)$ is the weak isospin of the fermion ($+\frac{1}{2}$ for u_i and ν_i, $-\frac{1}{2}$ for d_i and e_i), and Q_i is the charge of the fermion in units of the positron charge. At tree-graph level the Fermi constant can be written in terms of the coupling g_W:

$$\frac{g_W^2}{8M_W^2} = \frac{G_F}{\sqrt{2}}. \tag{6.12}$$

The electromagnetic and Fermi coupling constants are measured to high precision using the Josephson effect and the muon lifetime respectively:

$$\begin{aligned} \alpha^{-1} &= 137.03604(11) \\ G_F &= 1.16637(2) \times 10^{-5}\ \text{GeV}^{-2}. \end{aligned} \tag{6.13}$$

Using the value for the Weinberg angle derived from charged and neutral deep inelastic neutrino-nucleon total cross sections, $\sin^2\theta_W = 0.23$ [56], we obtain the leading order predictions for the masses:

$$\begin{aligned} M_W &= \sqrt{\left[\frac{\pi\alpha}{G_F\sqrt{2}}\right]}\frac{1}{\sin\theta_W} \approx 78\ \text{GeV}, \\ M_Z &= \frac{M_W}{\cos\theta_W} \approx 89\ \text{GeV}. \end{aligned} \tag{6.14}$$

The most recent measured values [57,58,59] for the masses are

$$\begin{aligned} M_W = {} & 79.91 \pm 0.35(\text{stat}) \pm 0.24(\text{sys}) \pm 0.19(\text{scale}) && : \text{CDF}(e\nu) \\ M_W = {} & 79.90 \pm 0.53(\text{stat}) \pm 0.32(\text{sys}) \pm 0.08(\text{scale}) && : \text{CDF}(\mu\nu) \\ M_W = {} & 80.79 \pm 0.31(\text{stat}) \pm 0.21(\text{sys}) \pm 0.81(\text{scale}) && : \text{UA2}(e\nu) \\ M_Z = {} & 91.49 \pm 0.35(\text{stat}) \pm 0.12(\text{sys}) \pm 0.92(\text{scale}) && : \text{UA2}(e^+e^-) \\ M_Z = {} & 91.150 \pm 0.032 && : \text{LEP} + \text{SLC} \end{aligned} \tag{6.15}$$

The differences between the predictions in Eq.(6.14) and the experimental measurements are due to higher order electroweak perturbative corrections. When these are taken into account [60], the agreement between theory and experiment is excellent.

In analogy with the Drell-Yan cross section in the previous section, the subprocess

cross sections for W and Z production are readily calculated to be

$$\begin{aligned} \hat{\sigma}^{q\bar{q}'\to W} &= \frac{\pi}{3}\sqrt{2}G_F M_W^2 \,|V_{qq'}|^2\, \delta(\hat{s}-M_W^2) \\ \hat{\sigma}^{q\bar{q}\to Z} &= \frac{\pi}{3}\sqrt{2}G_F M_Z^2 (V_q^2+A_q^2)\delta(\hat{s}-M_Z^2), \end{aligned} \tag{6.16}$$

where $V_{qq'}$ is the appropriate Kobayashi-Maskawa matrix element.

The $O(\alpha_S)$ perturbative QCD correction to the W and Z cross sections is the same as the Drell-Yan correction (for a photon of the same mass) discussed in the previous section – the gluon is 'flavour blind' and couples in the same way to the annihilating quark and antiquark. Fig.(38) shows the theoretical predictions for the W and Z cross sections (times leptonic branching ratios – see next section) compared with measurements from the $p\bar{p}$ collider experiments [61,62,63]. Note that the systematic and statistical errors on the measurements have been combined in quadrature. The values of the masses of the vector bosons have been chosen to be $M_W = 80$ GeV, $M_Z = 91.16$ GeV. The parton distributions are the HMRS(B) set, with the scale choice $\mu = M_{W,Z}$. We have included a $\pm 10\%$ error band on the theoretical prediction to allow for the uncertainties due to the parton distributions, to higher order electroweak corrections, and – most significantly – to the only partially known $O(\alpha_S^2)$ QCD corrections [64]. Evidently the agreement is very good. Note that this constitutes a non-trivial check on the evolution of the parton distributions, since in this calculation they are being evaluated at much higher μ values than the deep inelastic scattering data.

6.3 W and Z decay properties

At leading order in electroweak perturbation theory the partial widths of the W and Z bosons are given (in the standard model) by

$$\begin{aligned} \Gamma(W^+ \to f\bar{f}') &= N\frac{G_F M_W^3}{6\sqrt{2}\pi} \\ \Gamma(Z^0 \to f\bar{f}) &= N\frac{G_F M_Z^3}{6\sqrt{2}\pi}(V_f^2+A_f^2), \end{aligned} \tag{6.17}$$

where N is a normalisation factor which is 1 for leptons and 3 for quarks. For the latter, the W^+ decay rate refers to the sum of the decays to a given quark of charge

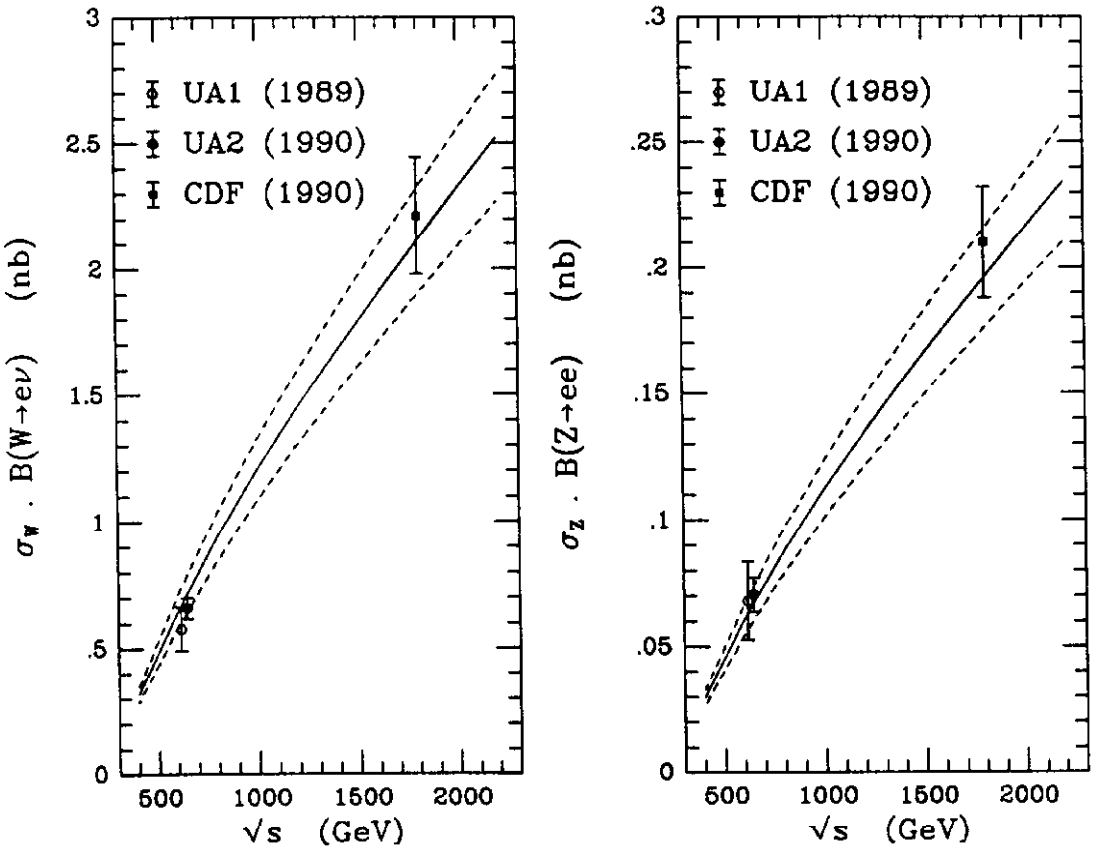

Figure 38: Comparison of W and Z cross section measurements with theoretical predictions

$\frac{2}{3}$ and all antiquarks of charge $\frac{1}{3}$, e.g. $W^+ \to u\bar{d} + u\bar{s} + u\bar{b}$. For any individual mode there is an additional factor from the Kobayashi-Maskawa mixing matrix.

Using these relations we can calculate the branching ratios for the observed decay modes. By counting decay modes we obtain for the W (if the top quark is heavy: $m_t > m_W - m_b$),

$$\begin{aligned} \mathrm{BR}(W^+ \to e^+\bar{\nu}, \mu^+\bar{\nu}, \tau^+\bar{\nu}) &= \frac{1}{3+3+3} \approx 11.1\% \\ \mathrm{BR}(W^+ \to u\bar{d} + u\bar{s} + u\bar{b}) &\approx 33.3\% \\ \mathrm{BR}(W^+ \to c\bar{d} + c\bar{s} + c\bar{b}) &\approx 33.3\%. \end{aligned} \tag{6.18}$$

For the Z we obtain

$$\begin{array}{c|c|c|c} e^+e^- & \nu_e\bar{\nu}_e & u\bar{u} & d\bar{d} \\ [1+(1-4\sin^2\theta_W)^2] & [2] & [1+(1-\frac{8}{3}\sin^2\theta_W)^2] & [1+(1-\frac{4}{3}\sin^2\theta_W)^2] \end{array} \tag{6.19}$$

Choosing $\sin^2\theta_W = 0.23$ gives

$$\begin{aligned} \mathrm{BR}(Z^0 \to e^+e^-, \mu^+\mu^-, \tau^+\tau^-) &\approx 3.4\% \\ \mathrm{BR}(Z^0 \to \textstyle\sum \nu_i\bar{\nu}_i) &\approx 20.4\% \\ \mathrm{BR}(Z^0 \to u\bar{u}, c\bar{c}) &\approx 11.8\% \\ \mathrm{BR}(Z^0 \to d\bar{d}, s\bar{s}, b\bar{b}) &\approx 15.2\%. \end{aligned} \tag{6.20}$$

Note the large branching fraction of the Z boson into neutrinos and bottom quarks.

Although the hadronic decay modes are enhanced relative to the leptonic modes, at hadronic colliders there is a very serious background from normal QCD two-jet production. A statistically significant signal has been reported by the UA2 collaboration [65]. The W decay mode into $t\bar{b}$ is of great interest since it offers the possibility of observing the top quark. Taking the mass of the top quark into account, (but setting the mass of the bottom quark equal to zero), the partial width of the W into top and bottom quarks is reduced from the expression given for $q_i\bar{q}_j$ above. The correct result is

$$\frac{\Gamma(W^+ \to t\bar{b})}{\Gamma(W^+ \to e^+\nu_e)} = 3|V_{tb}|^2(1-r_W)(1-\frac{r_W}{2}(1+r_W)), \tag{6.21}$$

where $r_W = m_t^2/M_W^2$. Counting up all modes we see that the branching ratio into a given leptonic channel, such as $e^+\nu_e$, is

$$\frac{1}{12} < B < \frac{1}{9} \tag{6.22}$$

depending on the mass of the top quark. The larger value holds when the decay to the top quark is forbidden. A massive top quark can also affect the Z branching ratios if $m_t < M_Z/2$. Including the effect of the top quark in both the matrix element and the phase space we find

$$\frac{\Gamma(Z^0 \to t\bar{t})}{\Gamma(Z^0 \to u\bar{u})} = \sqrt{1-4r_Z}\left[1+(1-\frac{8}{3}\sin^2\theta_W)^2 + 2r_Z((1-\frac{8}{3}\sin^2\theta_W)^2 - 2)\right] \tag{6.23}$$

where $r_Z = m_t^2/m_Z^2$.

Because the total widths (and hence the branching ratios) of the W and Z depend on m_t and (for the Z) on the number of light neutrino species, measurements of the production and leptonic decay rates can provide information on these quantities. Nowadays we know from precision measurements of the Z width at LEP that $N_\nu = 3$, and from direct searches by the CDF collaboration at the Tevatron $p\bar{p}$ collider that $m_t > 89$ GeV [66]. It is important nevertheless to check that the collider W and Z measurements are consistent with these results. It is not impossible, for example, that a light top quark with non-standard decays could evade direct discovery while still contributing to the total W decay width.

At a hadron collider the widths of the W and Z are hard to measure directly, and so we consider instead an indirect method, which however requires a certain amount of theoretical input [67]. The idea is to express the ratio R of the number of observed W and Z decays in terms of the ratio of production cross sections and branching fractions:

$$R = \frac{\text{Number of decays } W \to e\nu}{\text{Number of decays } Z \to ee} = \frac{\sigma_W}{\sigma_Z} \cdot \frac{\text{BR}(W \to e\nu)}{\text{BR}(Z \to ee)} = R_\sigma \cdot R_{\text{BR}}$$

$$R_{BR} = \frac{B(W \to l\nu)}{B(Z \to l^+l^-)} = \frac{\Gamma(W \to l\nu)}{\Gamma(W \to \text{all})} \frac{\Gamma(Z \to \text{all})}{\Gamma(Z \to l^+l^-)}. \qquad (6.24)$$

The ratio R_σ is calculable theoretically, with a certain error due to ignorance of the input parton distributions. In Fig.(39) theory is compared with experiment. The theoretical predictions are shown as functions of m_t, for $N_\nu = 3, 4, 5$. The band on each prediction is indicative of the theoretical uncertainty from parton distributions [38]. The most recent experimental measurements for R are [62,68]:

$$R = 9.38^{+0.82}_{-0.72}(\text{stat}) \pm 0.25(\text{sys}) : \quad \text{UA2}$$

$$R = 10.2 \pm 0.8(\text{stat}) \pm 0.4(\text{sys}) : \quad \text{CDF}. \qquad (6.25)$$

The results are evidently consistent with the $N_\nu = 3$, $m_t > 90$ GeV hypothesis.

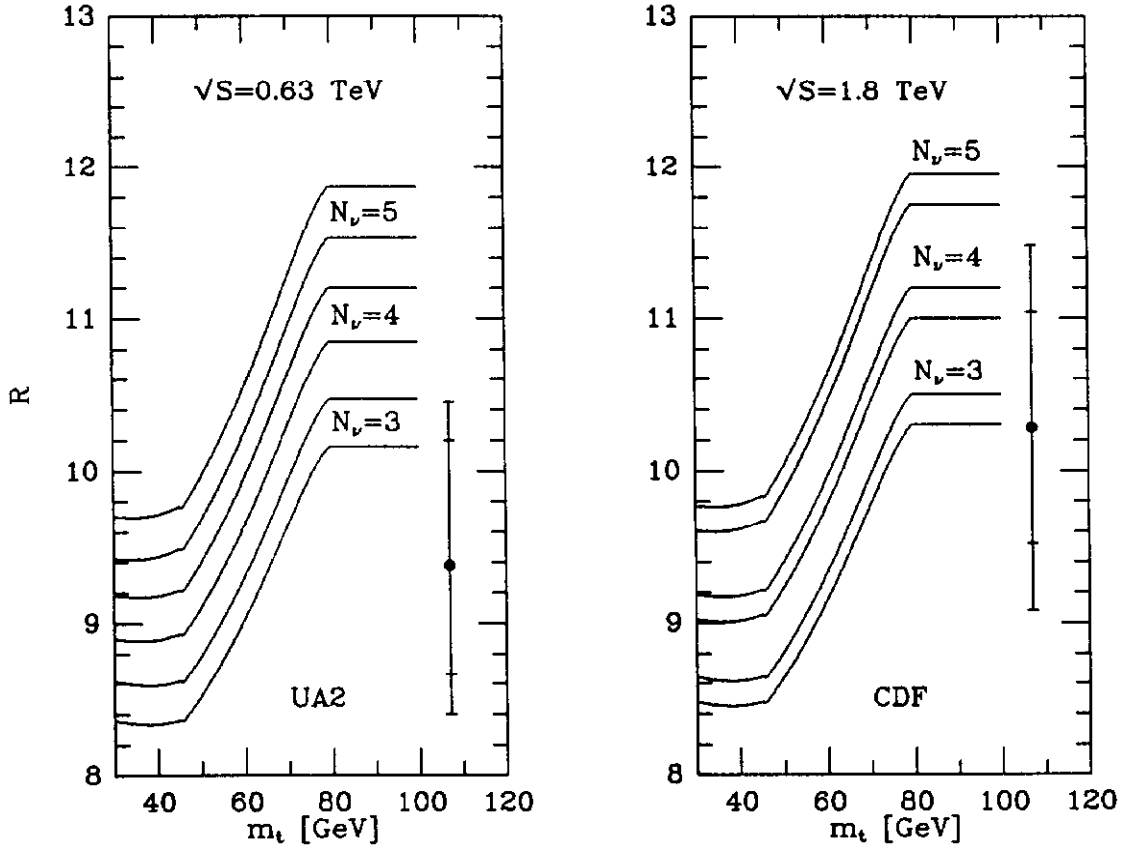

Figure 39: Theoretical values of the R ratio compared with data.

6.4 Lepton angular distribution in W and Z decay

Another important test of the theory concerns the $V-A$ structure of the weak charged current, Eq.(6.10). For the process

$$d(p_d) + \bar{u}(p_u) \rightarrow e^-(p_e) + \bar{\nu}(p_\nu), \tag{6.26}$$

where the momentum labels are shown in brackets, we obtain (using the couplings derived from the electroweak Lagrangian),

$$\overline{\sum}\left|M(d\bar{u} \rightarrow e^-\bar{\nu})\right|^2 = 64\left(\frac{G_F M_W^2}{\sqrt{2}}\right)^2 |V_{ud}|^2 \frac{(p_u \cdot p_e)^2}{[((p_u+p_d)^2 - M_W^2)^2 + M_W^2\Gamma^2]}. \tag{6.27}$$

Likewise, for the charge conjugate process, we have

$$\overline{\sum}\left|M(u\bar{d}\to e^+\nu)\right|^2 = 64\left(\frac{G_F M_W^2}{\sqrt{2}}\right)^2 |V_{ud}|^2 \frac{(p_u\cdot p_e)^2}{[((p_u+p_d)^2-M_W^2)^2+M_W^2\Gamma^2]}, \quad (6.28)$$

where now p_u is the momentum of the incoming u quark etc. If we define θ^* to be the $e^+(e^-)$ angle of emission in the W rest frame, measured with respect to the direction of the incident $\bar{p}(p)$, and if we assume that all incoming quarks (antiquarks) are constituents of the proton (antiproton), then for both of the above matrix elements we have

$$(p_u\cdot p_e)^2 \sim (1+\cos\theta^*)^2. \quad (6.29)$$

Thus the cross section is maximal when the outgoing electron (positron) moves in the direction of the incoming proton (antiproton). There is a simple angular momentum argument for this. In the standard model, the W couples to negative helicity fermions and positive helicity antifermions. Angular momentum conservation therefore requires the outgoing fermion (electron) to follow the direction of the incoming fermion (quark), which is usually the direction of the incoming proton.

The lepton asymmetry is clearly visible in the data. Fig.(40) shows θ^* distributions from the UA1 and UA2 collaborations [61,69]. The data are consistent with the $V-A$ hypothesis. Note, however, that since there are *two* W-fermion-fermion vertices in the scattering amplitude, the arguments are unchanged if the $(1-\gamma_5)$ coupling is replaced by $(1+\gamma_5)$.

The situation is more complicated for Z decay. Because the coupling of the Z to fermions is a combination of left- and right-handed pieces, the lepton angular distribution is an admixture of $(1\pm\cos\theta^*)^2$ terms, the relative amounts being determined by $\sin\theta_W$. Fig.(41) shows the angular distribution from the CDF collaboration [70]. The curve shows the standard model prediction with $\sin^2\theta_W = 0.231$.

6.5 W and Z transverse momentum distributions

Most W and Z bosons are produced with relatively little transverse momentum. However, part of the total cross section corresponds to the production of large transverse momentum bosons. The relevant mechanisms are the $2\to 2$ processes $q\bar{q}\to Vg$ and $qg\to Vq$. The diagrams are identical to those for large p_T direct photon production,

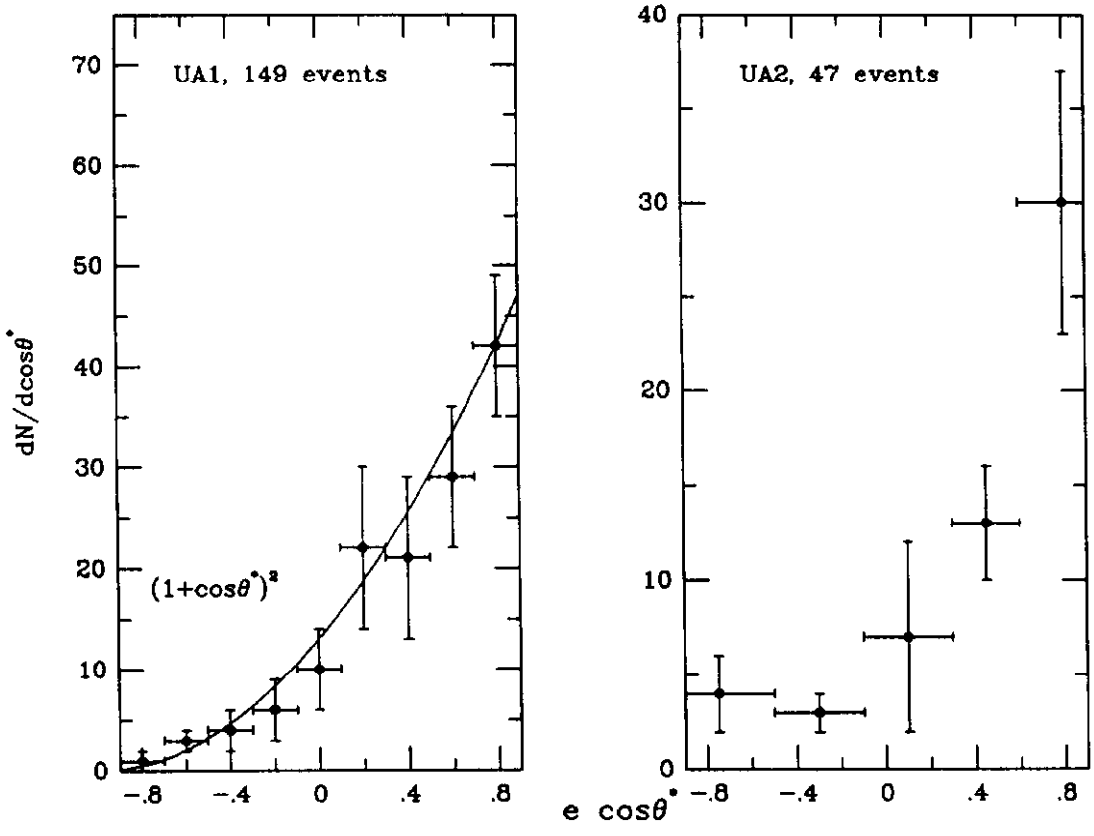

Figure 40: Angular distribution of leptons from W-boson decay.

Fig.(33), and the annihilation and Compton matrix elements are (Table 4)

$$\overline{\sum}\left|M^{q\bar{q}\to Wg}\right|^2 = \pi\alpha_S\sqrt{2}G_F M_W^2\,\frac{8}{9}\,\frac{t^2+u^2+2M_W^2 s}{tu}$$
$$\overline{\sum}\left|M^{gq\to Wq}\right|^2 = \pi\alpha_S\sqrt{2}G_F M_W^2\,\frac{1}{3}\,\frac{s^2+u^2+2tM_W^2}{-su}, \qquad (6.30)$$

with similar results for the Z obtained by changing the overall couplings. The W transverse momentum distribution is then obtained by convoluting these matrix elements with parton distributions in the usual way.

Data on the p_T distribution of the W from the CDF collaboration [72] are shown in Fig.(42). The curve is a next-to-leading order QCD prediction from Arnold and Reno [71], using HMRS(B) parton distributions. The agreement is very reasonable over the complete p_T range, although it is clearly not possible yet to use such data for

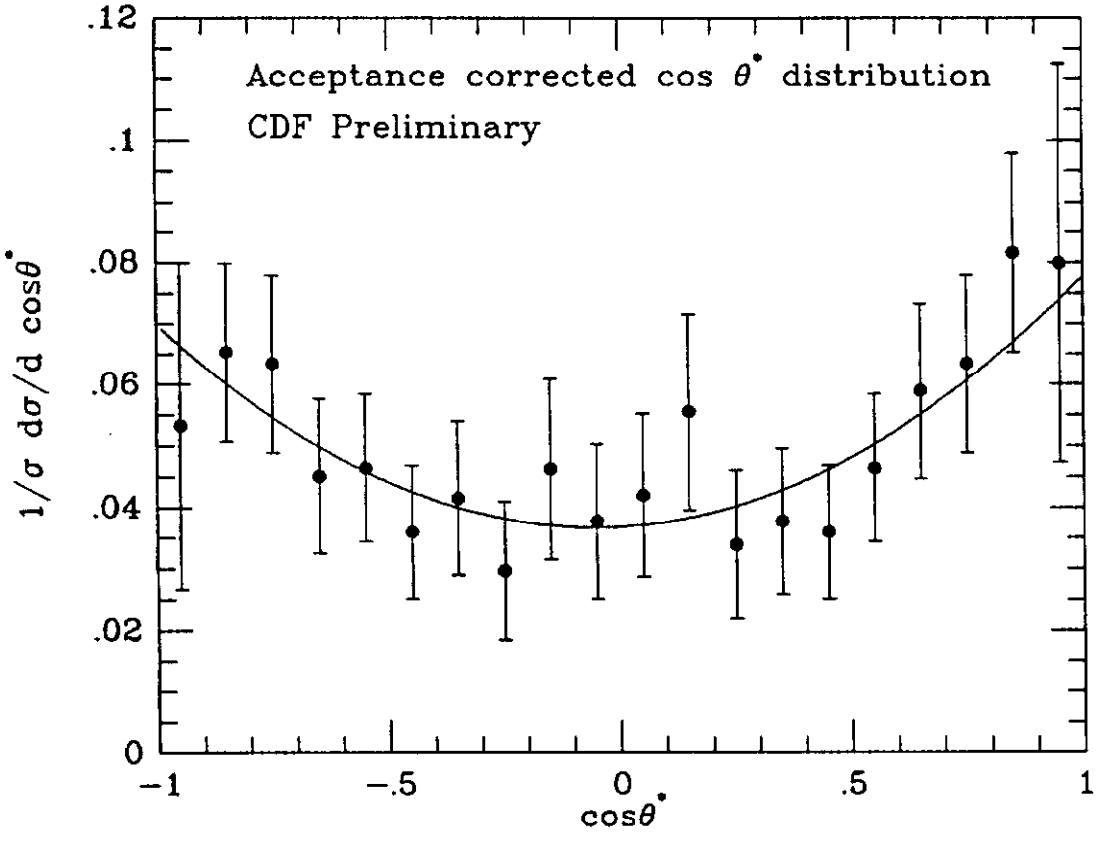

Figure 41: Angular distribution of leptons from Z-boson decay, from CDF

a *precision* $\Lambda_{\overline{\rm MS}}$ measurement. The UA2 collaboration have, however, derived a value for α_S to leading order by comparing the relative rates of $W + 1$ jet and $W + 0$ jet events [73]:

$$\alpha_S(\overline{\rm MS}, \mu = M_W) = 0.13 \pm 0.03\ (\text{stat}) \pm 0.03\ (\text{exp.sys}) \pm 0.02\ (\text{th.sys}). \quad (6.31)$$

From Fig.(2) we see that the result is consistent with measurements from other processes.

At small transverse momentum, the theoretical cross section in Fig.(42) diverges. This is a reflection of the infra-red singularity in the matrix element (i.e. the poles at $t = 0$ and $u = 0$ in the expressions given in Eq.(6.30)). As the transverse momentum becomes smaller, the emission of multiple soft gluons becomes important. The generic

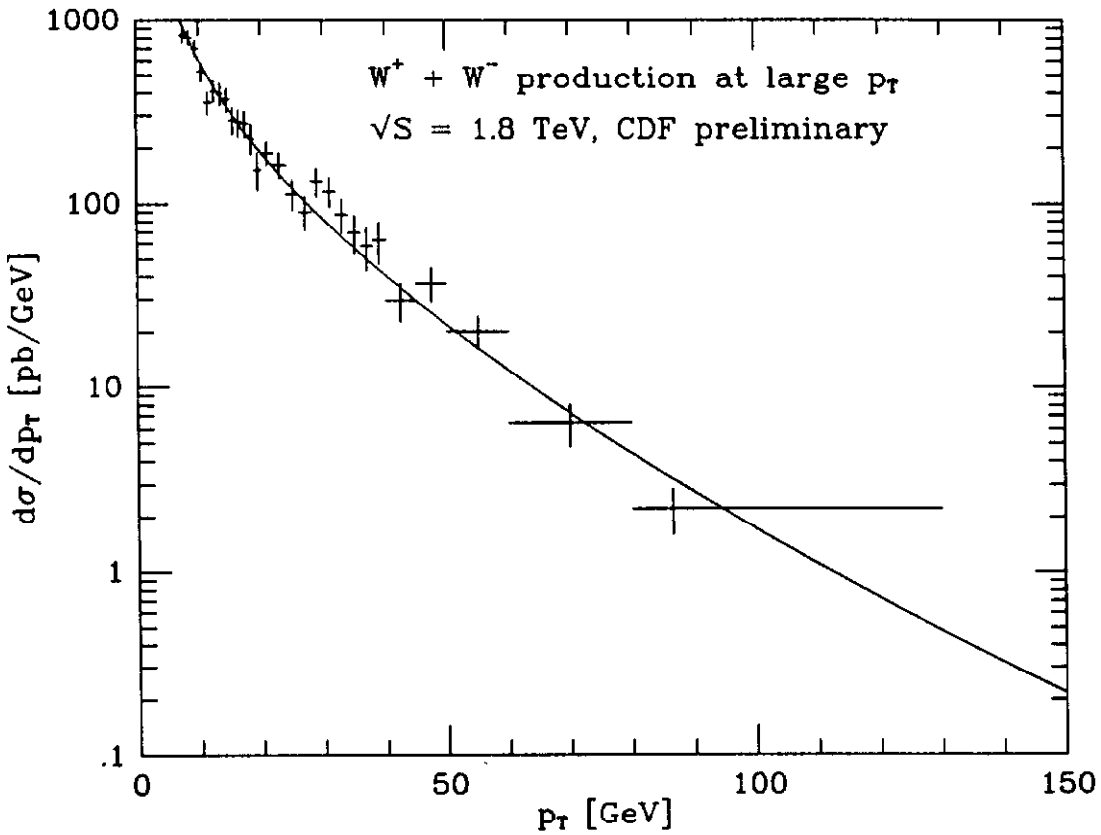

Figure 42: W transverse momentum distribution from the CDF collaboration, with next-to-leading order QCD predictions

expression for the cross section in this limit is:

$$\frac{1}{\sigma}\frac{d\sigma}{dp_T^2} \simeq A_1\frac{\alpha_S(p_T^2)}{p_T^2}\log\frac{M^2}{p_T^2} + A_2\frac{\alpha_S^2(p_T^2)}{p_T^2}\log^3\frac{M^2}{p_T^2} + \ldots, \tag{6.32}$$

where the A_i are coefficients of $O(1)$. The higher order terms are evidently important when

$$\alpha_S(p_T^2)\,\log^2\frac{M^2}{p_T^2} \sim 1. \tag{6.33}$$

In practice, this corresponds to p_T values less than about $10-15$ GeV/c. Fortunately, the large logarithms in Eq.(6.32) can be *resummed* to all orders in perturbation theory. For more details see reference [40]. The result is a 'Sudakov' form factor which regulates the cross section at small p_T. The small p_T QCD cross section is most

naturally expressed as a Fourier transform. Introducing the two-dimensional 'impact parameter' vector $\vec{b}$, which is the Fourier conjugate of $\vec{p_T}$, the cross section is given, schematically, by

$$\frac{1}{\sigma_0}\frac{d\sigma}{dp_T^2} \simeq \int_0^\infty db\ b\ J_0(bp_T)\ \exp(-S(b,M)) \cdot \int_0^1 dx_1\ dx_2 \delta(x_1x_2 - \frac{M^2}{s})\ q(x_1,b^{-1})\ \bar{q}(x_2,b^{-1}). \quad (6.34)$$

To the extent that the exponent S in Eq.(6.34) depends on α_S and hence on $\Lambda_{\overline{MS}}$, the small p_T distribution can in principle be used as a test of QCD. In practice, however, there are some difficulties – for example, some non-perturbative cut-off or smearing must be included to make the b integral in Eq.(6.34) converge at large b. This introduces some theoretical uncertainty. It is also difficult to make an accurate experimental measurement when the transverse momentum is of the same order as the missing transverse energy resolution. Fig.(43) shows an example of a comparison [74] of theory with data from the CDF collaboration [72]. The solid line is the resummed QCD prediction and the dashed line is the $O(\alpha_S^2)$ fixed order prediction. Note that the latter is singular at $p_T = 0$, in accordance with Eq.(6.32). Experiment and theory evidently agree quite well.

6.6 Multijet production with W and Z

One of the most important standard model processes in high energy hadron-hadron collisions is the production of a W or Z with accompanying hadron (quark or gluon) jets. Essentially *any* new physics process (heavy quarks, SUSY,...) can be mimicked by the production of vector bosons in association with jets. It is therefore important to be able to estimate these backgrounds accurately. In addition quantitative tests of QCD are possible – we have already mentioned in an earlier section the measurement by the UA2 collaboration of the strong coupling α_S from the relative rate of $W + 1$ jet and $W + 0$ jet production.

As long as the jets are required to be well-separated from each other and from the beam, the cross sections can be calculated from the matrix elements for the tree-level parton processes: $ij \to V + k_1 \ldots k_n$, where $V = W, Z$ and $i, j, k_r = q, g$. Details of how the matrix element calculations are performed, together with references to earlier

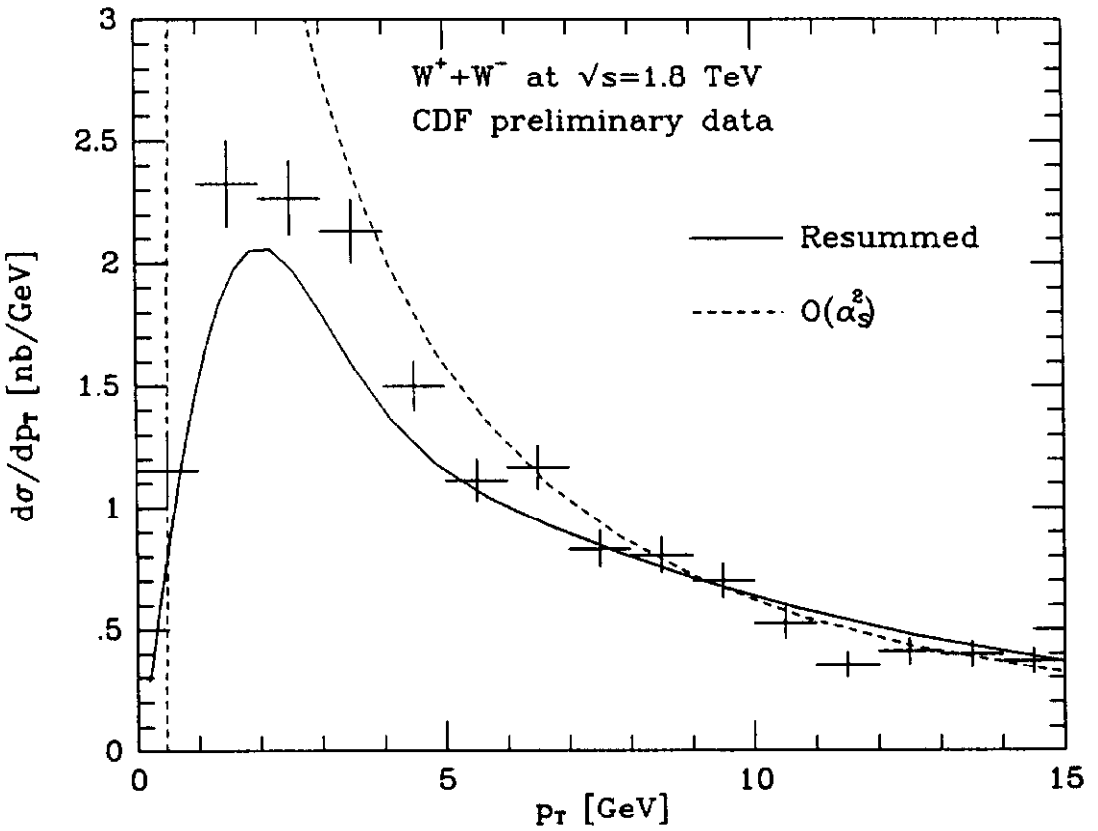

Figure 43: W transverse momentum distribution at small p_T^W, from the CDF collaboration, with resummed QCD predictions from ref. [74]

work, can be found in reference [45]. As an illustration, Fig.(44) shows the standard model predictions for the jet fractions f_n defined by

$$f_n = \frac{\sigma(p\bar{p} \to W + n \text{ jets})}{\sigma_{\text{tot}}(p\bar{p} \to W + X)} \tag{6.35}$$

at $\sqrt{s} = 1.8$ TeV, using a representative set of p_T, η and ΔR cuts for the final state leptons and jets. The predictions combine the $V + 0, 1, 2, 3$ jet calculations of reference [75] with the recent $V + 4$ jet calculation from reference [76]. It is interesting to note the almost exact geometric relation between the jet fractions, i.e. with this choice of cuts, the $0, \ldots, 4$ jet fractions are well-parametrised by $f_n = f_0(0.19)^n$. Given the complexity of the multijet calculations, it is surprising that the final predictions are related in this simple way.

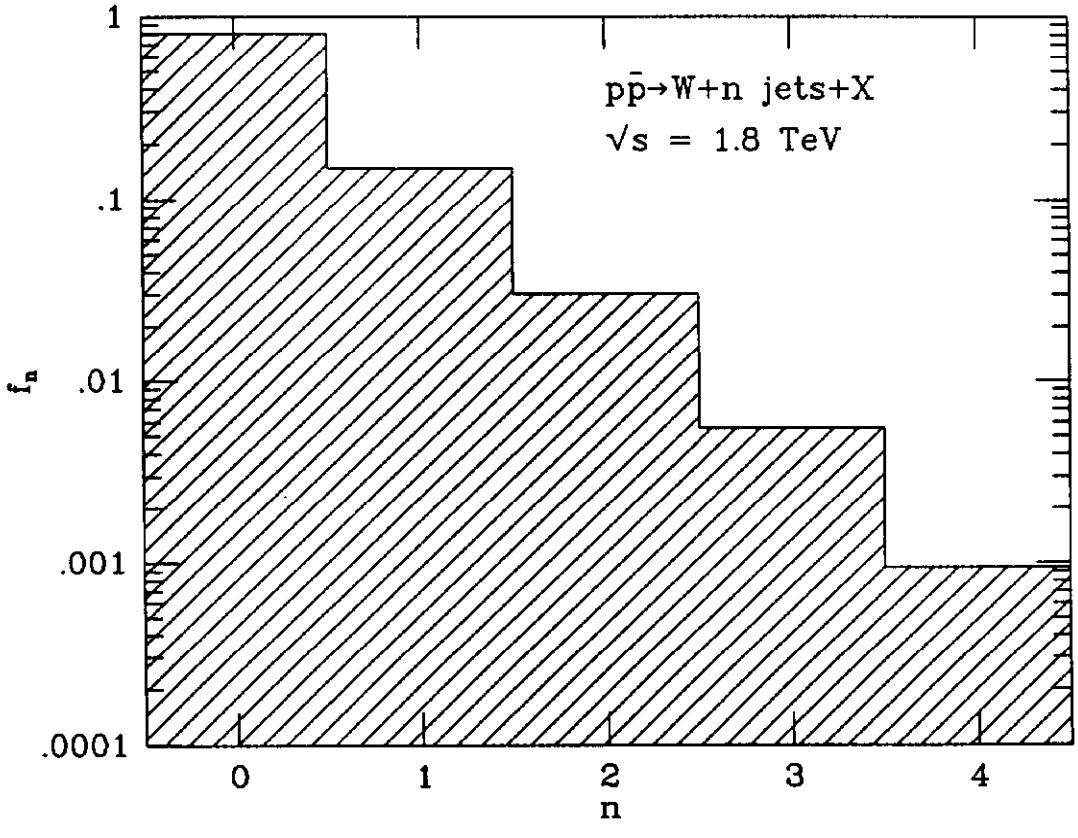

Figure 44: Predictions for the jet fractions in W production

7. The Production of Heavy Quarks

The production of heavy quarks is an important issue. One of the motivations for collider experiments is to discover new heavy objects, such as the top quark. It is therefore important to test our understanding of such production processes by predicting the production rates for the known heavy objects, such as the bottom quark. Because the cross sections are large, hadronic interactions offer the potential to produce the large number of bottom quarks necessary to study their decays in detail. For example, with sufficient b's it may be possible to observe CP violation in the b system. The disadvantage of hadronically produced b's is that they have to be distinguished from a large background of other hadrons. It is therefore necessary to find an efficient way to isolate the bottom events from the background. This is done by using the special properties of their decay products.

7.1 The decays of heavy quarks

The existence of hadrons containing heavy quarks is deduced by observation of their decays. Therefore any experiment which measures the cross section for the production of hadrons containing heavy quarks makes assumptions concerning the branching fraction to the observed mode.

We shall start by considering the decays of a free top quark in the standard model. We shall consider the case $m_t > m_W$ as well as the experimentally less favoured case $m_t < m_W$. Consider the decay of a very massive top quark which decays into an on-shell W boson and a b quark. This process has a semi-weak decay rate involving only one power of the Fermi constant. In the limit in which $m_t \gg m_W$ the total t width is given by,

$$\Gamma(t \to bW) = \frac{G_F m_t^3}{8\pi\sqrt{2}} |V_{tb}|^2 \approx 170 \text{ MeV} \left(\frac{m_t}{m_W}\right)^3. \tag{7.1}$$

When the top quark is so heavy that the width becomes bigger than a typical hadronic scale the top quark decays before it hadronises. Hadrons containing the top quark are never formed.

This should be compared with the top quark decay for $m_t < m_W - m_b$ which is a

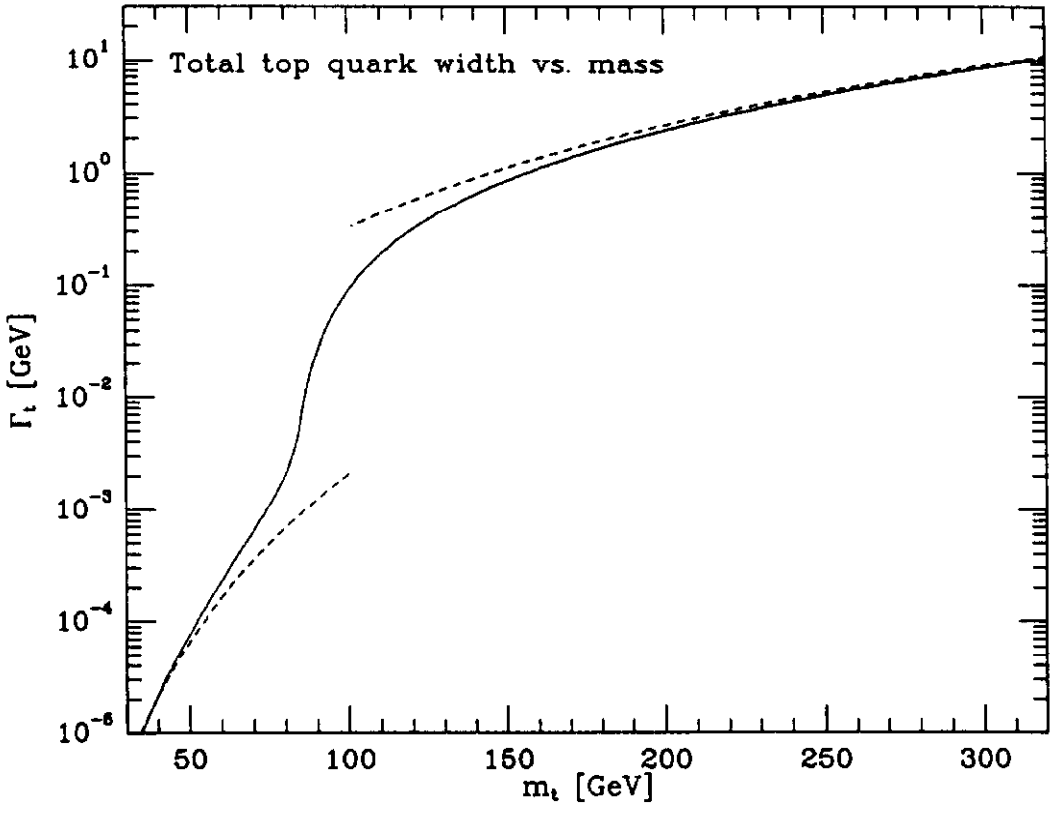

Figure 45: The total width of the top quark

scaled-up version of μ decay. In this case the partial width into $e\bar{\nu}$ is given by,

$$\Gamma(t \to be\bar{\nu}) = \frac{G_F^2 m_t^5}{192\pi^3} |V_{tb}|^2 \approx 2.3 \text{ keV} \left(\frac{m_t}{40 \text{ GeV}} \right)^5 . \tag{7.2}$$

Fig.(45) shows the width of the top quark for general values of the top mass. The dashed lines show the asymptotes derived from Eq.(7.1) and Eq.(7.2).

In both cases the top branching ratio to leptons is given in the simplest approximation by counting modes for the W decay. Assuming the decay channel to $t\bar{b}$ is forbidden because $m_t > m_W - m_b$, the branching ratio is given by counting the decay modes $e\bar{\nu}_e$, $\mu\bar{\nu}_\mu$, $\tau\bar{\nu}_\tau$ and three colours of $u\bar{d}$ and $c\bar{s}$.

$$\text{BR}(W^+ \to e^+\bar{\nu}) = \frac{1}{3+3+3} \approx 11\% \tag{7.3}$$

All direct searches for the top quark make assumptions about the branching ratio into leptons. It is important to investigate unconventional decays of the top quark, especially if they alter the branching ratio into the leptonic decay mode. As an example, we consider a simple extension of the standard model which involves the introduction of a second Higgs doublet. Top quark decay in this model has been investigated in ref. [77]. In order to avoid strangeness changing neutral currents [78] one must couple all quarks of a given charge to only one Higgs doublet. After spontaneous symmetry breaking we are left with one charged physical Higgs η and three neutral Higgs particles. If $m_t > m_\eta + m_b$ the dominant decay mode of the top quark is not to a leptonic mode, but rather to the charged Higgs,

$$\Gamma(t \to b\eta^+) > \frac{1}{4\pi v}\frac{m_b}{m_t^2}(m_t^2 + m_b^2 - m_\eta^2 + 2m_t m_b)\lambda^{\frac{1}{2}}(m_t^2, m_b^2, m_\eta^2) \qquad (7.4)$$

In this equation $\lambda(a,b,c) = ((a-b-c)^2 - 4bc)$ and v is the normal vacuum expectation value. As an extreme example, for $m_t = 30$ GeV, $m_\eta = 25$ GeV and $m_b = 4.7$ GeV it is found [77] that $\Gamma \geq 0.4 MeV$. It is clear that for a large range of parameters, the semi-weak width Eq.(7.4) greatly exceeds the weak width as determined from Eq.(7.2). The decay modes of the η^+ determine the signature of the light top quark in this model. The η^+ decays predominantly to $c\bar{s}$ and $\bar{\tau}\nu_\tau$. If the vacuum expectation values of the two Higgs fields are taken to be equal the branching fraction into $c\bar{s}$ is 64% and into $\bar{\tau}\nu_\tau$ is 31% for $m_\eta = 25$ GeV [77].

We may also treat the decays of the B-meson in analogy with the decay of a free muon. This is called the spectator model, since the quarks which accompany the b quark in the B-meson play no role in the decay. However in this case the finite masses of the u and c quarks, to which the b decays, must be taken into account. In addition strong interaction corrections can be appreciable because $\alpha_S(m_b)$ is large. For further details and references to the original papers see ref. [79].

7.2 The theory of heavy quark production

The leading order processes for the production of a heavy quark Q of mass m are,

$$\begin{aligned} &(a) \quad q(p_1) + \bar{q}(p_2) \to Q(p_3) + \overline{Q}(p_4) \\ &(b) \quad g(p_1) + g(p_2) \to Q(p_3) + \overline{Q}(p_4) \ , \end{aligned} \qquad (7.5)$$

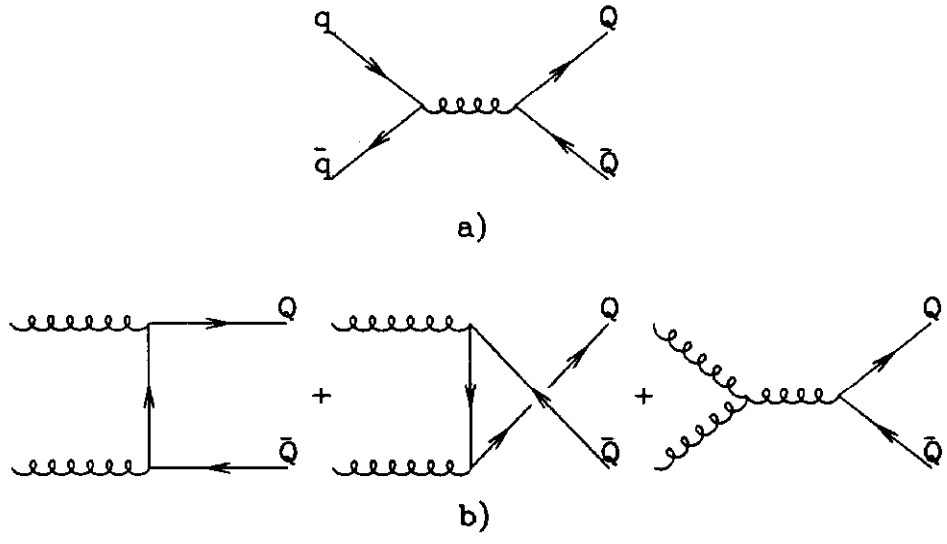

Figure 46: Lowest order Feynman diagrams for heavy quark production

where the four momenta of the partons are given in brackets. The Feynman diagrams which contribute to the matrix elements squared in $O(g^4)$ are shown in Fig.(46). The invariant matrix elements squared [80,81] which result from the diagrams in Fig. (46) are given in Table 5. The matrix elements squared have been averaged (summed) over initial (final) colours and spins, (as indicated by $\overline{\sum}$). In order to express the matrix elements in a compact form, we have introduced the following notation for the ratios of scalar products,

$$\tau_1 = \frac{2p_1.p_3}{\hat{s}}, \quad \tau_2 = \frac{2p_2.p_3}{\hat{s}}, \quad \rho = \frac{4m^2}{\hat{s}}, \quad \hat{s} = (p_1 + p_2)^2. \tag{7.6}$$

In leading order the short distance cross section is obtained from the invariant

Process	$\overline{\sum}\|M\|^2/g^4$
$q\,\overline{q} \to Q\,\overline{Q}$	$\frac{4}{9}\left(\tau_1^2+\tau_2^2+\frac{\rho}{2}\right)$
$g\,g \to Q\,\overline{Q}$	$\left(\frac{1}{6\tau_1\tau_2}-\frac{3}{8}\right)\left(\tau_1^2+\tau_2^2+\rho-\frac{\rho^2}{4\tau_1\tau_2}\right)$

Table 5: Lowest order processes for heavy quark production. $\overline{\sum}|M|^2$ is the invariant matrix element squared. The colour and spin indices are averaged (summed) over initial (final) states.

matrix element in the normal fashion [1]:

$$d\hat{\sigma}_{ij} = \frac{1}{2\hat{s}}\,\frac{d^3p_3}{(2\pi)^3 2E_3}\,\frac{d^3p_4}{(2\pi)^3 2E_4}(2\pi)^4\delta^4(p_1+p_2-p_3-p_4)\,\overline{\sum}|M_{ij}|^2\,. \tag{7.7}$$

The first factor is the flux factor for massless incoming particles. The other terms come from the phase space for two-to-two scattering.

We shall now illustrate why it is plausible that heavy quark production is described by perturbation theory [82]. Consider first the differential cross section. Let us denote the momenta of the incoming hadrons, which are moving in the z direction, by P_1 and P_2 and the square of the total centre of mass energy by s where $s=(P_1+P_2)^2$. The short distance cross section in Eq.(4.1) is to be evaluated for parton momenta $p_1=x_1P_1$, $p_2=x_2P_2$ and hence the square of the total parton centre of mass energy is $\hat{s}=x_1x_2s$, if we ignore the masses of the incoming particles. The rapidity variable for the two final state partons is defined in terms of their energies and longitudinal momenta as,

$$y=\frac{1}{2}\ln\left[\frac{E+p_z}{E-p_z}\right]. \tag{7.8}$$

Using Eqs.(4.1) and (7.7) the result for the invariant cross section may be written as,

$$\frac{d\sigma}{dy_3dy_4d^2p_T}=\frac{1}{16\pi^2\hat{s}^2}\sum_{ij}x_1f_i(x_1,\mu)x_2f_j(x_2,\mu)\overline{\sum}|M_{ij}|^2\,. \tag{7.9}$$

The energy momentum delta function in Eq.(7.7) fixes the values of x_1 and x_2 if we

know the value of the p_T and rapidity of the outgoing heavy quarks. In the centre of mass system of the incoming hadrons we may write the components of the parton four momenta as (E, p_x, p_y, p_z)

$$\begin{aligned} p_1 &= \sqrt{s}/2(x_1, 0, 0, x_1) \\ p_2 &= \sqrt{s}/2(x_2, 0, 0, -x_2) \\ p_3 &= (m_T \cosh y_3, p_T, 0, m_T \sinh y_3) \\ p_4 &= (m_T \cosh y_4, -p_T, 0, m_T \sinh y_4). \end{aligned} \tag{7.10}$$

Applying energy and momentum conservation we obtain,

$$x_1 = \frac{m_T}{\sqrt{s}}(e^{y_3} + e^{y_4}), \quad x_2 = \frac{m_T}{\sqrt{s}}(e^{-y_3} + e^{-y_4}), \quad \hat{s} = 2m_T^2(1 + \cosh \Delta y). \tag{7.11}$$

The transverse mass of the heavy quarks is denoted by $m_T = \sqrt{(m^2 + p_T^2)}$ and $\Delta y = y_3 - y_4$ is the rapidity difference between the two heavy quarks.

Using Eqs.(7.9) and (7.11), we may write the cross section for the production of two massive quarks calculated in lowest order perturbation theory as,

$$\frac{d\sigma}{dy_3 dy_4 d^2p_T} = \frac{1}{64\pi^2 m_T^4 (1 + \cosh(\Delta y))^2} \sum_{ij} x_1 f_i(x_1, \mu)\, x_2 f_j(x_2, \mu) \overline{\sum} |M_{ij}|^2 . \tag{7.12}$$

Expressed in terms of m, m_T and Δy the matrix elements for the two processes in Table 5 are,

$$\overline{\sum} |M_{q\bar{q}}|^2 = \frac{4g^4}{9}\Big(\frac{1}{1 + \cosh(\Delta y)}\Big)\Big(\cosh(\Delta y) + \frac{m^2}{m_T^2}\Big) \tag{7.13}$$

$$\overline{\sum} |M_{gg}|^2 = \frac{g^4}{24}\Big(\frac{8\cosh(\Delta y) - 1}{1 + \cosh(\Delta y)}\Big)\Big(\cosh(\Delta y) + 2\frac{m^2}{m_T^2} - 2\frac{m^4}{m_T^4}\Big). \tag{7.14}$$

Note that, because of the specific form of the matrix elements squared, the cross section, Eq.(7.12), is strongly damped as the rapidity separation Δy between the two heavy quarks becomes large. It is therefore to be expected that the dominant contribution to the total cross section comes from the region $\Delta y \leq 1$. Heavy quarks produced by $q\bar{q}$ annihilation are more closely correlated those produced by gluon-gluon fusion.

We now consider the propagators in the diagrams shown in Fig.(46). In terms of the above variables they can be written as,

$$\begin{aligned}(p_1+p_2)^2 &= 2p_1.p_2 &= 2m_T^2(1+\cosh\Delta y)\\ (p_1-p_3)^2-m^2 &= -2p_1.p_3 &= -m_T^2(1+e^{-\Delta y})\\ (p_2-p_3)^2-m^2 &= -2p_2.p_3 &= -m_T^2(1+e^{\Delta y}).\end{aligned} \tag{7.15}$$

Note that the denominators are all off-shell by a quantity of least of order m^2. It is this fact which distinguishes the production of a light quark from the production of a heavy quark. When a light quark is produced by these diagrams the lower cut-off on the virtuality of the propagators is provided by the light quark mass, which is less than the QCD scale Λ. Since propagators with small virtualities give the dominant contribution, the production of a light quark will not be calculable in perturbative QCD. In the production of a heavy quark, the lower cut-off is provided by the mass m. It is therefore plausible that heavy quark production is controlled by α_S evaluated at the heavy quark scale.

Note also that the contribution to the cross section from values of p_T which are much greater than the quark mass is also suppressed. The differential cross section falls like $1/m_T^4$ and as m_T increases, the parton flux decreases because of the increase of x_1 and x_2 according to Eq.(7.11). Since all dependence on the transverse momentum appears in the transverse mass combination, the dominant contribution to the cross section comes from transverse momenta of the order of the mass of the heavy quark.

Thus for a sufficiently heavy quark we expect the methods of perturbation theory to be applicable. It is the mass of the heavy quark which provides the large scale in heavy quark production. The heavy quarks have transverse momenta of the order of the heavy quark mass and are produced close in rapidity. The production is predominantly central, because of the rapidly falling parton fluxes. Final state interactions which transform the heavy quarks into the observed hadrons will not change the size of the cross section. A possible mechanism which might spoil this simple picture would be the interaction of the produced heavy quark with the debris of the incoming hadrons. However these interactions with spectator partons are suppressed by powers of the heavy quark mass [83]. For a sufficiently heavy quark they can be ignored.

The theoretical arguments summarized above do not address the issue of whether the charmed quark is sufficiently heavy that the hadroproduction of charmed hadrons in all regions of phase space is well described by only processes (a) and (b) and their perturbative corrections.

7.3 Higher order corrections to heavy quark production

The lowest order terms presented above are the beginning of a systematic expansion in the running coupling,

$$\hat{\sigma}_{ij}(s,m^2) = \frac{\alpha_S^2(\mu)}{m^2}\mathcal{F}_{ij}\left(\rho,\frac{\mu^2}{m^2}\right) \tag{7.16}$$

Eq.(7.16) completely describes the short distance cross-section for the production of a heavy quark of mass m in terms of the functions $\mathcal{F}_{ij}$, where the indices i and j specify the types of the annihilating partons. The dimensionless functions $\mathcal{F}_{ij}$ have the following perturbative expansion,

$$\mathcal{F}_{ij}\left(\rho,\frac{\mu^2}{m^2}\right) = \mathcal{F}_{ij}^{(0)}(\rho) + 4\pi\alpha_S(\mu)\left[\mathcal{F}_{ij}^{(1)}(\rho) + \overline{\mathcal{F}}_{ij}^{(1)}(\rho)\ln(\frac{\mu^2}{m^2})\right] + O(g^4) \tag{7.17}$$

where ρ is defined in Eq.(7.6). The functions $\mathcal{F}_{ij}^{(1)}$ are completely known [84,85]. Examples of the types of diagrams which contribute to $\mathcal{F}_{ij}^{(1)}$ are shown in Fig.(47). The full calculation involves both real and virtual corrections. For full details we refer the reader to ref. [84]. In order to calculate the $\mathcal{F}_{ij}$ in perturbation theory we must perform both renormalisation and factorisation of mass singularities. The subtractions required for renormalisation and factorisation are done at mass scale μ. The dependence on μ of the non-leading order term is displayed explicitly in Eq.(7.17).

As discussed in previous lectures μ is an unphysical parameter. The physical predictions should be invariant under changes of μ at the appropriate order in perturbation theory. If we have performed a calculation to $O(\alpha_S^3)$, variations of the scale μ will lead to corrections of $O(\alpha_S^4)$,

$$\mu^2\frac{d}{d\mu^2}\sigma = O(\alpha_S^4). \tag{7.18}$$

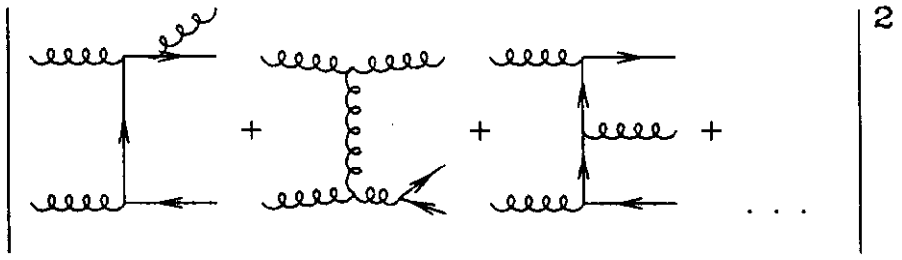

Real emission diagrams

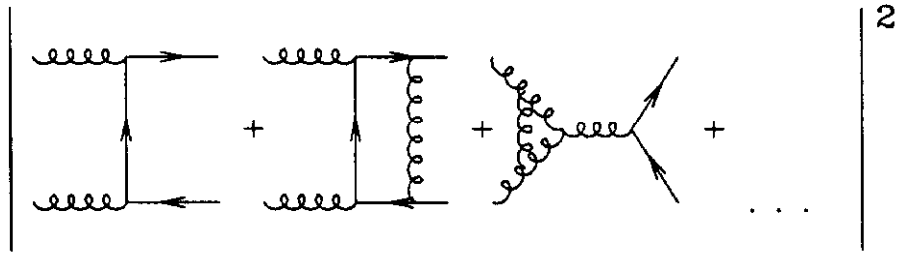

Virtual emission diagrams

Figure 47: Examples of higher order corrections to heavy quark production

In this equation σ is the hadronic cross section as determined by Eq. (4.1). Using Eq.(7.18) we find that the term $\overline{\mathcal{F}}^{(1)}$ which controls the μ dependence of the higher order perturbative contributions is fixed in terms of the lower order result $\mathcal{F}^{(0)}$:

$$\overline{\mathcal{F}}^{(1)}_{ij}(\rho) = \frac{1}{8\pi^2}\left[4\pi b\mathcal{F}^{(0)}_{ij}(\rho) - \int_\rho^1 dz_1\, \mathcal{F}^{(0)}_{kj}(\frac{\rho}{z_1})P_{ki}(z_1) - \int_\rho^1 dz_2\, \mathcal{F}^{(0)}_{ik}(\frac{\rho}{z_2})P_{kj}(z_2)\right]. \quad (7.19)$$

In obtaining this result we have used the renormalisation group equation for the running coupling, Eq.(1.22)

$$\mu^2\frac{d}{d\mu^2}\alpha_S(\mu) = -b\alpha_S^2(1 + b'\alpha_S + \ldots)$$

$$b = \frac{33 - 2n_f}{12\pi}, \quad b' = \frac{153 - 19n_f}{2\pi(33 - 2n_f)} \quad (7.20)$$

and the Altarelli-Parisi equation,

$$\mu^2 \frac{d}{d\mu^2} f_i(x,\mu) = \frac{\alpha_S(\mu)}{2\pi} \sum_k \int_x^1 \frac{dz}{z} P_{ik}(z) f_k(\frac{x}{z},\mu). \tag{7.21}$$

This illustrates an important point which is a general feature of renormalisation group improved perturbation series in QCD. The coefficient of the perturbative correction depends on the choice made for μ, but the μ dependence changes the result in such a way that the physical result is independent of the choice made for μ. Thus the μ dependence is formally small because it is of higher order in α_S. This does not assure us that the μ dependence is actually *numerically* small for all series. A pronounced dependence on μ is a signal of an untrustworthy perturbation series.

We shall illustrate this point by showing the μ dependence found in two cases of current interest. First, in Fig.(48), we show the μ dependence found for the hadroproduction of a 120 GeV top quark in leading and next-to-leading order. The inclusion of the higher order terms leads to a stabilisation of the theoretical prediction with respect to changes in μ. The situation for the bottom quark is quite different. In Fig.(49) the scale dependence of the predicted bottom quark cross section is shown. The cross section is approximately doubled by the inclusion of the higher order corrections, which do nothing to improve the stability of the prediction under changes of μ. It is apparent that the predictions for bottom production at collider energies are subject to considerable uncertainty.

We now turn to the question of flavour excitation. A flavour excitation diagram is one in which the heavy flavour is considered to reside already in the incoming hadron. It is excited by a gluon from the other hadron and appears on shell in the final state. An example of a flavour excitation diagram is shown in Fig.(50a). Note that in calculating the flavour excitation contribution the incoming heavy quark is treated as it were on its mass shell. If we denote the momentum transfer between the two incoming partons as q, the parton cross section will contain a factor $1/q^4$ coming from the propagator of the exchanged gluon. Therefore these graphs appear to be sensitive to momentum scales all the way down to the hadronic size scale. This casts doubt on the applicability of perturbative QCD to these processes.

In the following we shall sketch an analysis [82] which leads to an important conclusion. When considering the total cross section, flavour excitation contributions should not be included. The net contribution of these diagrams is already included as

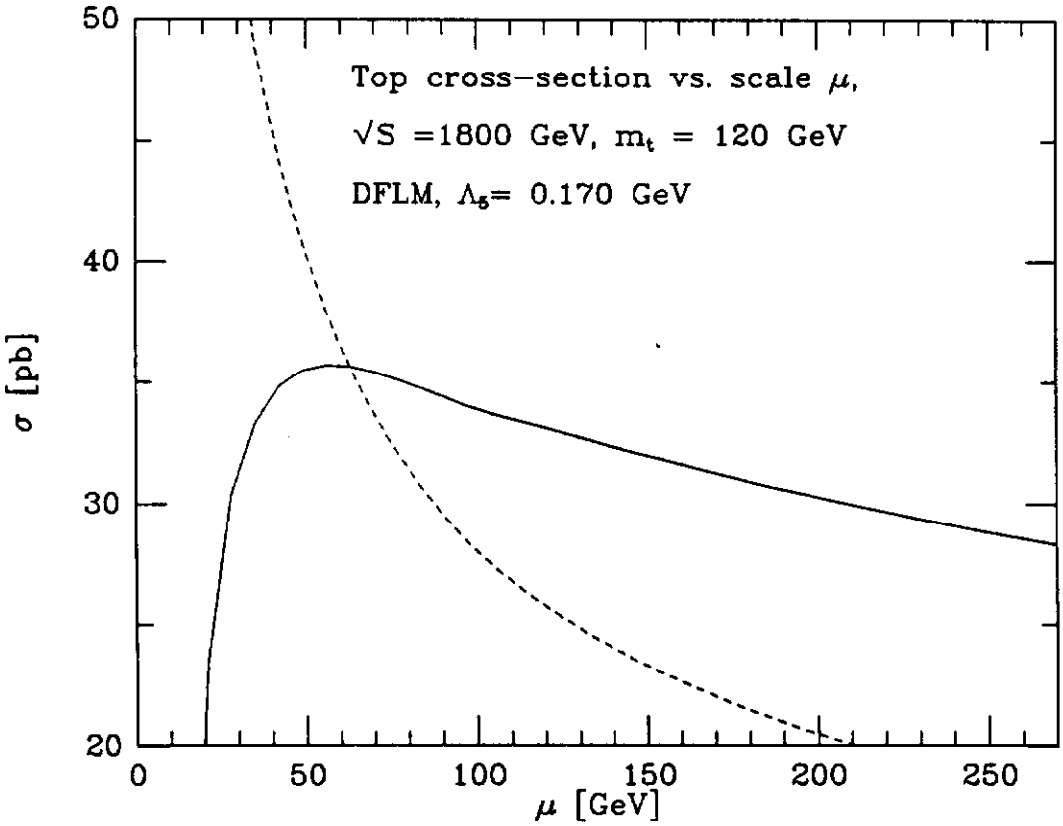

Figure 48: Scale dependence of the top quark cross section in second and third order

a higher order correction to the gluon-gluon fusion process. This analysis begins from the observation that the flavour excitation graph is already present as a subgraph of the first two diagrams shown in Fig.(50b). Does the flavour excitation approximation accurately represent the results of these diagrams? In particular is the $1/q^4$ pole, which is the signature of the presence of the flavour excitation diagrams, present in these diagrams?

We shall now indicate why the $1/q^4$ behaviour is not present in the sum of all three diagrams displayed in Fig.(50b). Let us denote the 'plus' and 'minus' components of any vector q as follows:

$$q^+ = q^0 + q^3, \quad q^- = q^0 - q^3, \quad q^2 = q^+ q^- - q_T \cdot q_T. \tag{7.22}$$

We choose the upper incoming parton in Fig.(50b) to be directed along the 'plus'

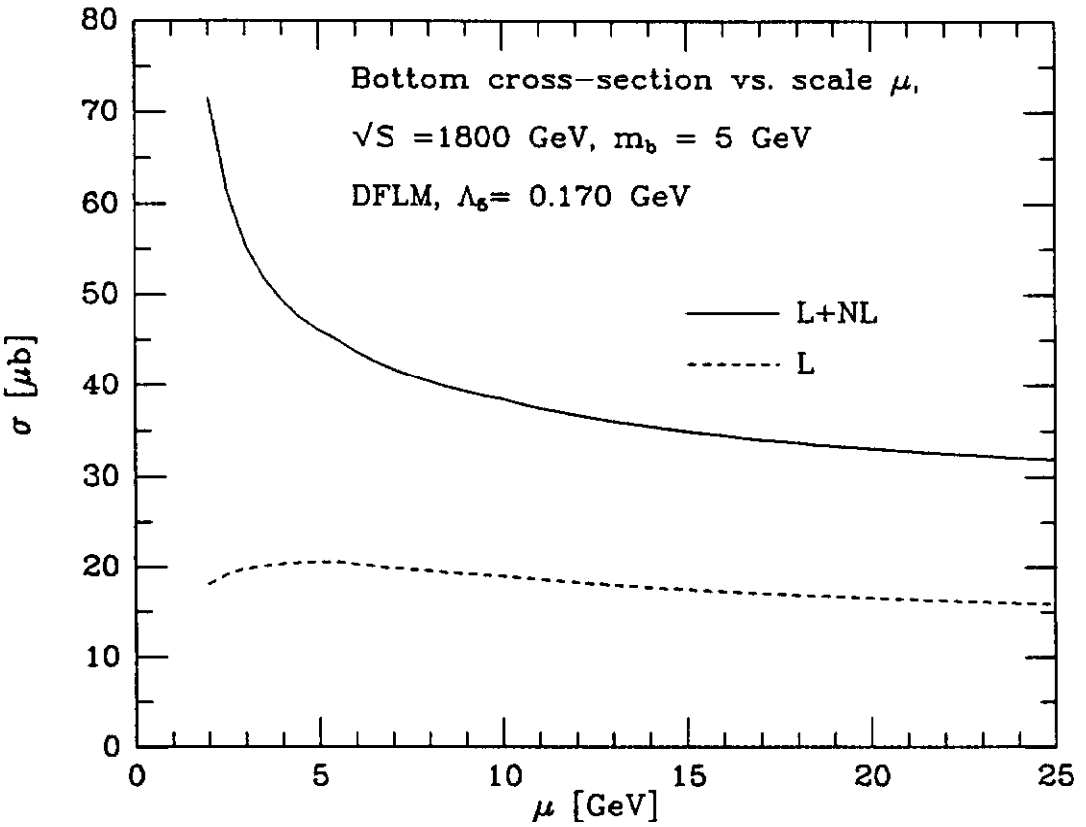

Figure 49: Scale dependence of the bottom quark cross section in second and third order

direction, $p_1 = p_1^+$. and the lower incoming parton to be directed along the 'minus' direction, $p_2 = p_2^-$. In the small q^2 region the 'plus' component of q is small, because the lower final state gluon is on shell,

$$(p_2 - q)^2 = 0, \quad q^+ = \frac{q^2}{2p_2^-}, \tag{7.23}$$

since in the centre of mass system $p_1^+ \approx p_2^- \approx \sqrt{s}$. In the low q^2 region the 'minus' component of q is determined from the condition that production is close to threshold,

$$(p_1 + q)^2 \approx 4m^2, \quad q^- \approx \frac{m^2}{p_1^+}. \tag{7.24}$$

q^- is therefore also small in the fragmentation region in which $p_1^+ \approx \sqrt{s}$. We therefore

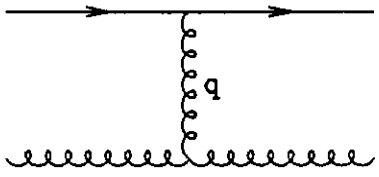

a) Example of flavour excitation graph

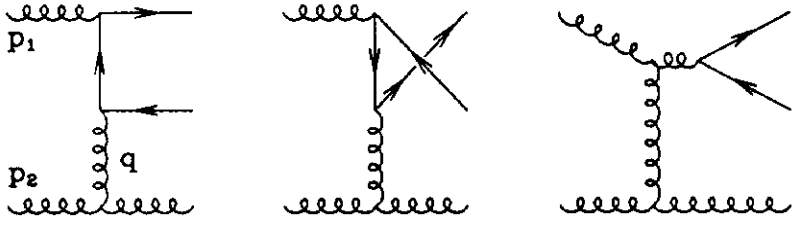

b) Graphs containing spin-one exchange in the t-channel

Figure 50: Graphs relevant for discussion of flavour excitation

find that in the fragmentation region of the upper incoming hadron,

$$q^2 = q^+q^- - q_T \cdot q_T \approx -q_T \cdot q_T \tag{7.25}$$

The current J to which the exchanged gluon of momentum q couples is determined by the upper part of the three diagrams. In the fragmentation region only the 'plus' component is large.

$$q^\mu J_\mu = q^+J^- + q^-J^+ - q_T \cdot J_T = 0, \;\; J^+ \approx \frac{q_T \cdot J_T}{q^-} \tag{7.26}$$

where the Ward identity is a property of the sum of all three diagrams. The explicit term proportional to q_T in the amplitude shows that one power of the $1/q^2$ is cancelled in the amplitude squared.

This cancellation only occurs when the soft approximation to J^+ is valid. This requires the terms quadratic in q to be small compared to the terms linear in q in the denominators in the upper parts of the diagrams in Fig.(50b). The momentum q^- must not be too small,

$$q^2 < 2p^+q^- \approx m^2. \tag{7.27}$$

We therefore expect the soft approximation to be valid and some cancellation to occur when $q^2 < m^2$. For further details we refer the reader to ref. [82]. The calculation of ref. [84] provides an explicit verification of this cancellation in the total cross section.

7.4 Results on the production of charm and bottom quarks

The value of the heavy quark mass is the principal parameter controlling the size of the cross section. This dependence is much more marked than the $1/m^2$ dependence in the short distance cross section expected from Eq.(7.16). As the mass decreases, the value of x at which the parton distributions are evaluated becomes smaller (*cf.* Eq.(7.11)) and the cross section rises because of the growth of the parton flux.

The approach which we shall take to the estimate of theoretical errors in heavy quark cross sections is as follows [86]. We shall take Λ to run in the range given by Eq.(1.46) with corresponding variations of the gluon distribution function. We shall arbitrarily choose to vary the parameter μ in the range $m/2 < \mu < 2m$ to test the sensitivity to μ. Lastly, we shall consider quark masses in the ranges,

$$\begin{aligned} 1.2 \ &< m_c < \ 1.8 \text{ GeV} \\ 4.5 \ &< m_b < \ 5.0 \text{ GeV}. \end{aligned} \tag{7.28}$$

We shall consider the extremum of all these variations to give an estimate of the theoretical error.

We immediately encounter a difficulty with this procedure in the case of charm. Variations of μ down to $m/2$ will carry us into the region $\mu < 1$ GeV in which we certainly do not trust perturbation theory. A estimate of the theoretical error on charm production cross sections is therefore not possible. In preparing the curve for charm production We have taken the lower limit on μ variations to be 1 GeV.

The dependence on the value chosen for the heavy quark mass is particularly acute

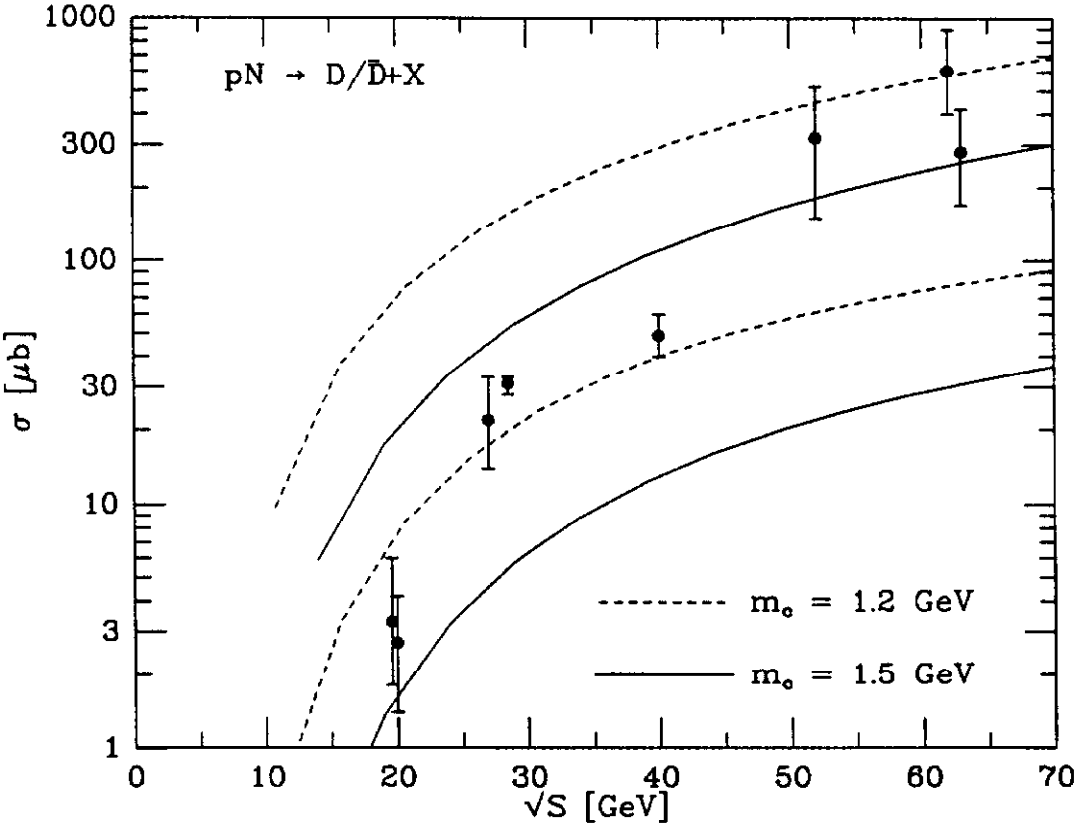

Figure 51: Data on hadroproduction of $D/\bar{D}$ compared with theory

for the case of charm. In fact, variations due to plausible changes in the quark mass, Eq.(7.28), are bigger than the uncertainties due to variations in the other parameters. We shall therefore take the aim of studies of the hadroproduction and photoproduction of charm to be the search for an answer to the following question. Is there a reasonable value for the charm quark mass which can accommodate the majority of the data on hadroproduction? In Fig.(51) we show the theoretical prediction for charm production. Note the large spread in the prediction. Also shown plotted is a compilation of data taken from ref. [87] which suggests that a value of $m_c = 1.5$ GeV gives a fair description of the data on the hadroproduction of D's. After inclusion of the $O(\alpha_S^3)$ corrections, the data can be explained without recourse to very small values of the charmed quark mass [86].

This conclusion is further reinforced by consideration of the data on photopro-

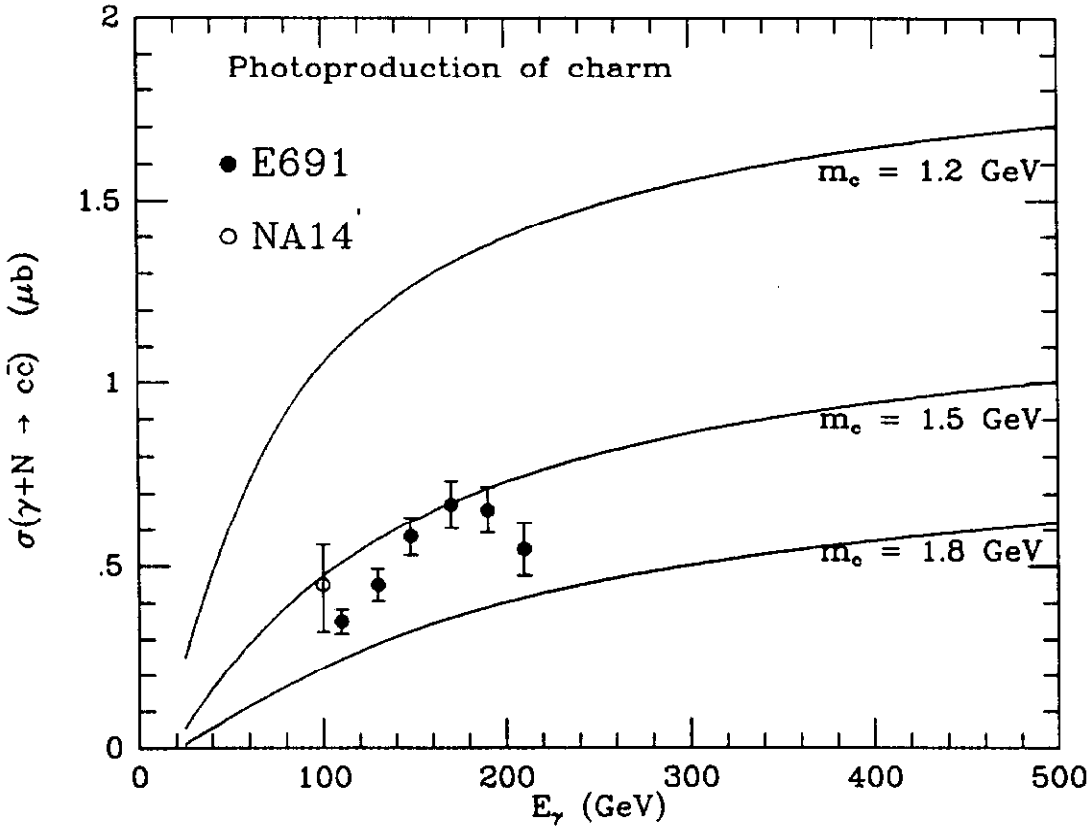

Figure 52: Data on photoproduction of charm compared with theoretical lower limits

duction of charm. The higher order $O(\alpha\alpha_S^2)$ corrections to photoproduction have been considered in ref. [88]. After inclusion of these higher order terms we obtain predictions for the total cross section as a function of the energy of the tagged photon beam. The principal uncertainty derives from the value of the heavy quark mass, so we have plotted the minimum cross section which is obtained by varying Λ and the scale μ within the range 1 GeV $< \mu < 2m$ for three values of the charm quark mass. The comparison with the data on the photoproduction of charm [89,90], shown in Fig.(52), indicates that charm quark masses smaller than 1.5 GeV do not give an acceptable explanation of the data.

In conclusion, within the large uncertainties present in the theoretical estimates, the $D/\bar{D}$ production data presented here can be explained with a charm quark mass of the order of 1.5 GeV. This is not true of all data on the hadroproduction of charm,

especially the older experiments. For a review of the experimental situation we refer the reader to ref. [91].

As emphasised above, the theoretical prediction for bottom quark production at collider energies is very uncertain. The cause of this large uncertainty is principally the very small value of x at which the parton distributions are probed. In fact, at present collider energies the bottom cross section is sensitive to the gluon distribution function at values of $x < 10^{-2}$. Needless to say the gluon distribution function has not been measured at such small values of x. An associated problem is the form of the short distance cross section in the large $\hat{s}$ region. The lowest order short distance cross sections, $\mathcal{F}^{(0)}$, tend to zero in the large $\hat{s}$ region [84]. This is a consequence of the fact that they involve at most spin $\frac{1}{2}$ exchange in the t-channel as shown in Fig.(46). The higher order corrections to gg and gq processes have a different behaviour because they involve spin 1 exchange in the t-channel. The relevant diagrams are shown in Fig.(50b). In the high energy limit they yield a constant cross section, independent of energy [84]. Naturally these high $\hat{s}$ contributions are damped by the small number of energetic gluons in the parton flux, but at collider energies the region $\sqrt{\hat{s}} \gg m$ makes a sizeable contribution to the bottom cross section. The fact that this constant behaviour is present in both $\mathcal{F}^{(1)}$ and $\overline{\mathcal{F}}^{(1)}$ indicates the sensitivity of the size of this term to the value chosen for μ. There is therefore an interplay between the size of this term and the small x behaviour of the gluon distribution function.

At fixed target energies the cross section for the production of bottom quarks is theoretically more reliable. The μ dependence plot has a characteristic form similar to Fig.(48) and it is possible to make estimates of the theoretical errors. A compilation of theoretical results [92] and estimates of the associated theoretical error is shown in Table 6. The experimental study of the production of bottom quarks in hadronic reactions is still in its infancy, but Table 6 also includes the limited number of experimental results on total bottom production cross sections.

The calculations of ref. [84] also allow us to examine the p_T and rapidity distributions of the one heavy quark inclusive cross sections. Although the prediction of the total bottom cross section at collider energy is uncertain, it is plausible that the shape of the transverse momentum and rapidity distributions is well described by the form found in lowest order pertubation theory. The supporting evidence [97] for this conjecture is shown in Fig.(53), which demonstrates that the inclusion of the

m_b [GeV]	σ (theory)	Theoretical error	Experimental data
$\sqrt{s}$ = 41 GeV, pp			
4.5	23 nb	+21 -15	
5.0	9 nb	+8.4 -5.9	
$\sqrt{s}$ = 62 GeV, pp			
4.5	142 nb	+98 -80	BCF[93], 150 < σ < 500 nb
5.0	66 nb	+47 -38	
$\sqrt{s}$ = 630 GeV, $p\bar{p}$			
4.5	19 μb	+10 -8	UA1[94], 10.2±3.3 μb
5.0	12 μb	+7 -4	
$\sqrt{s}$ = 24.5 GeV, πN			
4.5	7.6 nb	+4.7 -3.8	WA78[95], $\sqrt{s}$= 24.5 GeV, 4.8 ±0.6±1.5 nb
5.0	3.1 nb	+1.5 -1.5	NA10[96], $\sqrt{s}$= 23 GeV, 14+7-6 nb

Table 6: Cross section for bottom production at various energies.

first non-leading correction does not significantly modify the shape of the transverse momentum and rapidity distributions. At a fixed value of μ, the two curves lie on top of one another if the lowest order is multiplied by a constant factor. Similar results hold also for the shape of the top quark distribution [97]. The UA1 collaboration have investigated the transverse distribution of the produced bottom quarks. In Fig.(54) comparison of the full α_S^3 prediction with UA1 data is made. The data are plotted as a function of the lower cutoff $p_T^b(min)$ on the transverse momentum of the b quark. The agreement is satisfactory.

The corresponding prediction for the shape of the bottom production cross section at the Tevatron is shown in Fig.(55).

7.5 The search for the top quark

The belief that the top quark must exist is based both on theoretical and experimental evidence. The theoretical motivation is that complete families are required for the cancellation of anomalies in the currents which couple to gauge fields. Hence the partner of the b, τ and ν_τ must exist to complete the third family.

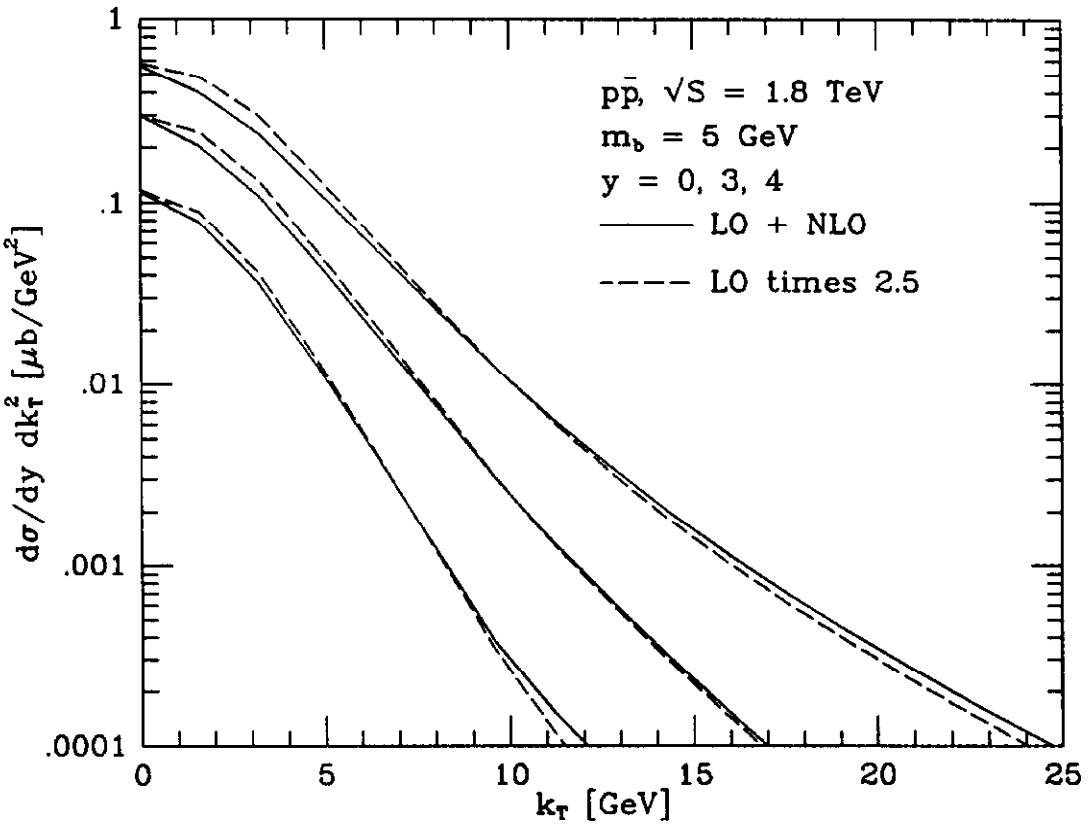

Figure 53: The shape of the cross-section for bottom quark production

An anomaly occurs in a theory because symmetries present at the classical level are destroyed by quantum effects. They typically involve contributions to the divergence of a current which is conserved at the classical level. If the gauge currents are anomalous, the Ward identities, which are vital for the proof that the gauge theory is renormalisable, are destroyed.

Anomalies occur in the simple triangle diagram with two vector currents and one axial vector current. Elimination of the anomalies for a particular current in the lowest order triangle diagram is sufficient to ensure that the current remains anomaly free, even after the inclusion of more complicated diagrams. If the currents which interact at the three corners of the triangle couple to the matrices L^a, L^b and L^c for the left-handed fields, and to the matrices R^a, R^b and R^c for the right-handed fields,

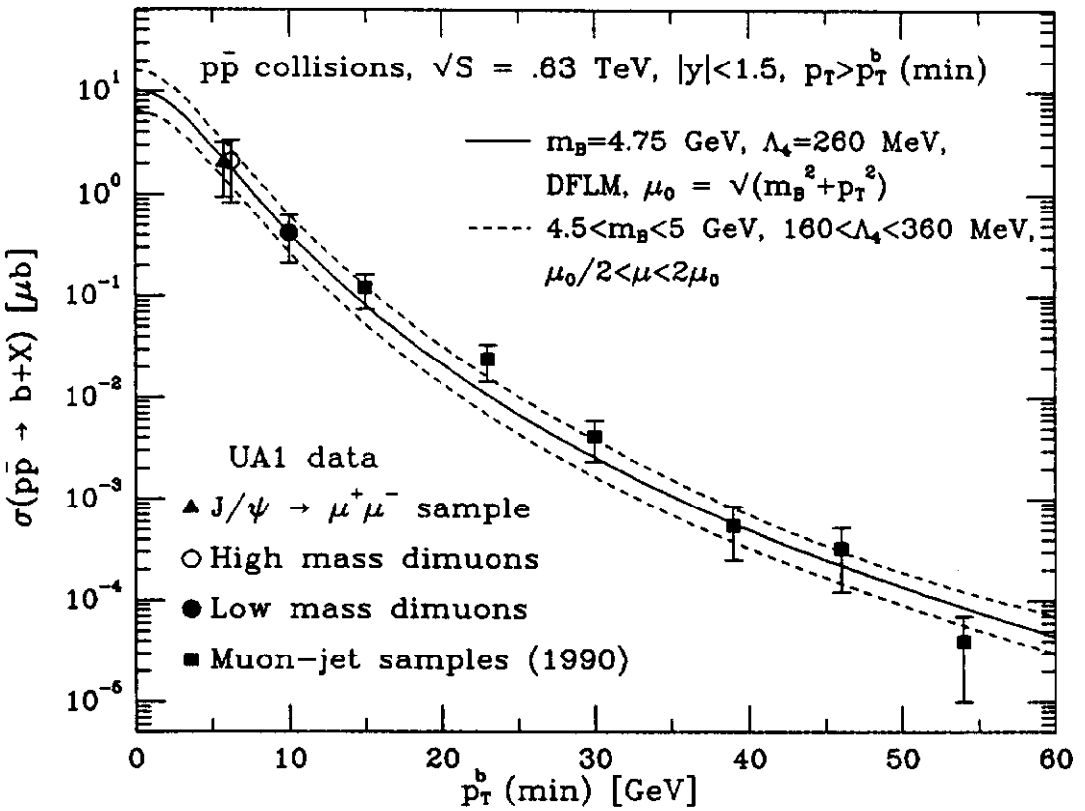

Figure 54: The cross-section for bottom quark production at CERN energy

the vector-vector-axial vector triangle anomaly is proportional to,

$$A = \mathrm{Tr}\,[R^a\{R^b, R^c\}] - \mathrm{Tr}\,[L^a\{L^b, L^c\}]. \tag{7.29}$$

For the specific case of the $SU(2)_L \times U(1)$ theory of Glashow, Weinberg and Salam (GSW) we have the following weak isospin and hypercharge assignments for the third family ($Q = T_3 + Y$),

$$\begin{aligned}
&t_L,\ T_3 = \tfrac{1}{2}, Y_L = \tfrac{1}{6}, \qquad t_R,\ T_3 = 0,\ Y_R = \frac{2}{3},\\
&b_L,\ T_3 = -\tfrac{1}{2}, Y_L = \tfrac{1}{6}, \qquad b_R,\ T_3 = 0,\ Y_R = -\frac{1}{3},\\
&\nu_L,\ T_3 = \tfrac{1}{2}, Y_L = -\tfrac{1}{2}\\
&\tau_L,\ T_3 = -\tfrac{1}{2}, Y_L = -\tfrac{1}{2}, \qquad \tau_R,\ T_3 = 0,\ Y_R = -1.
\end{aligned} \tag{7.30}$$

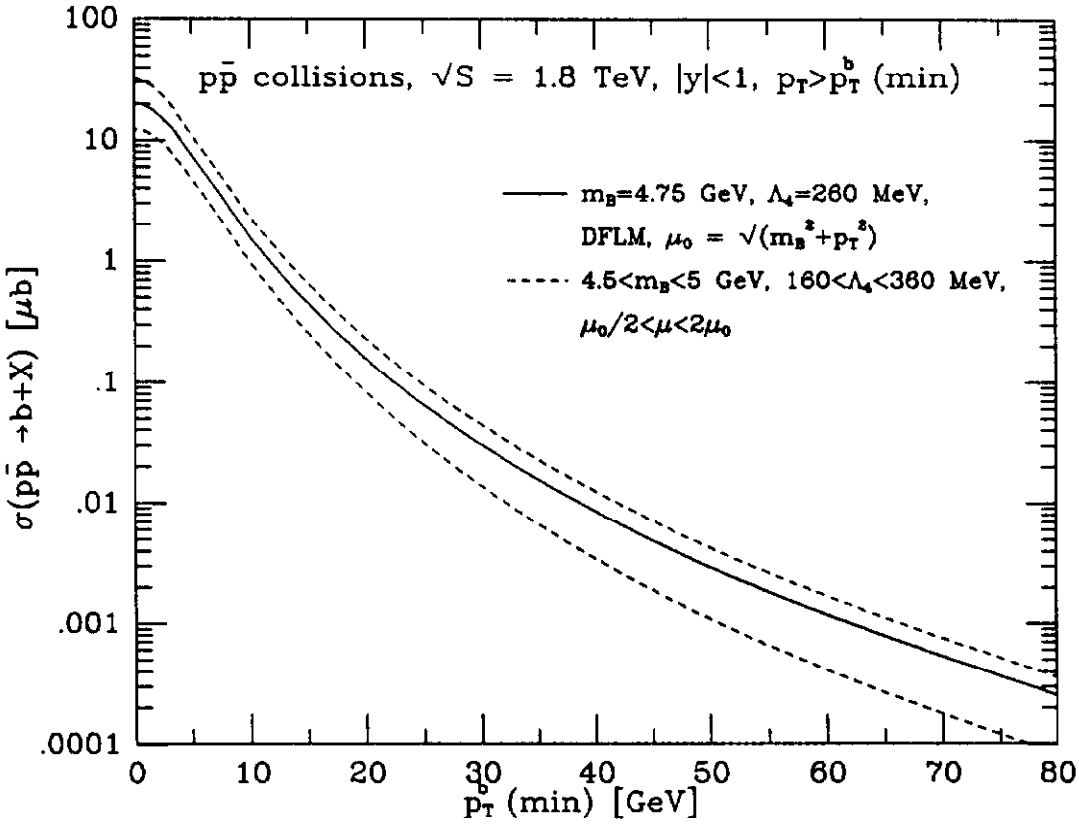

Figure 55: The cross-section for bottom quark production at FNAL energy

Substituting these couplings into Eq.(7.29), with all combinations of the $SU(2)$ matrices T^a or the $U(1)$ matrices Y we obtain the form of the anomaly for the gauge currents of the GSW theory. Two of the resulting traces of the couplings vanish for each fermion separately,

$$\mathrm{Tr}\, T^a\{T^b, T^c\} = 0, \quad \mathrm{Tr}\, T^a\{Y_L, Y_L\} = 0. \tag{7.31}$$

The other two traces vanish only for a complete family [98]

$$\mathrm{Tr}\,(Y_R^3 - Y_L^3) = 0, \quad \mathrm{Tr}\, Y_L\{T^a, T^b\} = 0. \tag{7.32}$$

It should be noted that there are still anomalies in global (non-gauged) currents in the GSW model. For example the normal isospin current corresponding to a global symmetry (in the absence of quark masses) is anomalous. It is this anomaly which is

responsible for π^0 decay.

The experimental reason to believe in the existence of the top quark is the measurement of the weak isospin of the bottom quark. The forward backward asymmetry of b-jets in e^+e^- annihilation [99] is controlled by $A_e A_b$, the product of the axial vector coupling to the electron and the b quark. The produced b and $\bar{b}$ quarks are identified by the sign of the observed muons to which they decay. The measurement is therefore subject to a small correction due to $B^0 - \overline{B^0}$ mixing. Assuming that the axial coupling to the electron has its standard value the measured weak isospin of the left-handed b quark is [99],

$$T_3 = -0.5 \pm 0.1. \tag{7.33}$$

The simplest hypothesis is that the bottom quark is in an $SU(2)$ doublet with the top quark, although more complicated schemes are certainly possible.

Thus assured that the top quark exists, it only remains to find it. The expected cross section for the process

$$p + \bar{p} \rightarrow t + \bar{t} + X \tag{7.34}$$

is shown in Fig.(56). The cross section is calculated using the full $O(\alpha_S^3)$ calculation of [84] and the method of theoretical error estimate described in the previous sections, (*cf.* [86]). In addition, production of top quarks through the decay chain $W \rightarrow t\bar{b}$ is also shown. Note the differing proportions of the two modes at CERN and FNAL energies. At $\sqrt{s} = 1.8(0.63)$ TeV the $t\bar{t}$ production is due predominantly to gluon-gluon annihilation for $m_t < 100(40)$ GeV. On the other hand the W production comes mainly from $q\bar{q}$ annihilation at both energies. This explains the more rapid growth with energy of the $t\bar{t}$ production shown in Fig.(56).

From Fig.(56) the range of top quark masses which can be investigated in current experiments can be derived. In a sample of 5 inverse picobarns about 2500 $t\bar{t}$ pairs will be produced if the top quark has a mass of 70 GeV. One can observe the decays of the top quark to the $e\mu$ channel or to the $e+$ jets channel. With a perfect detector the numbers of events expected is,

$$\begin{aligned} \text{Number of } e\mu \text{ events} &= \quad 2 \times .11 \times .11 \times 2500 \approx 60 \\ \text{Number of e + jet events} &= \quad 2 \times .11 \times .66 \times 2500 \approx 360. \end{aligned} \tag{7.35}$$

The e plus jets channel gives a more copious signal and does not require muon detec-

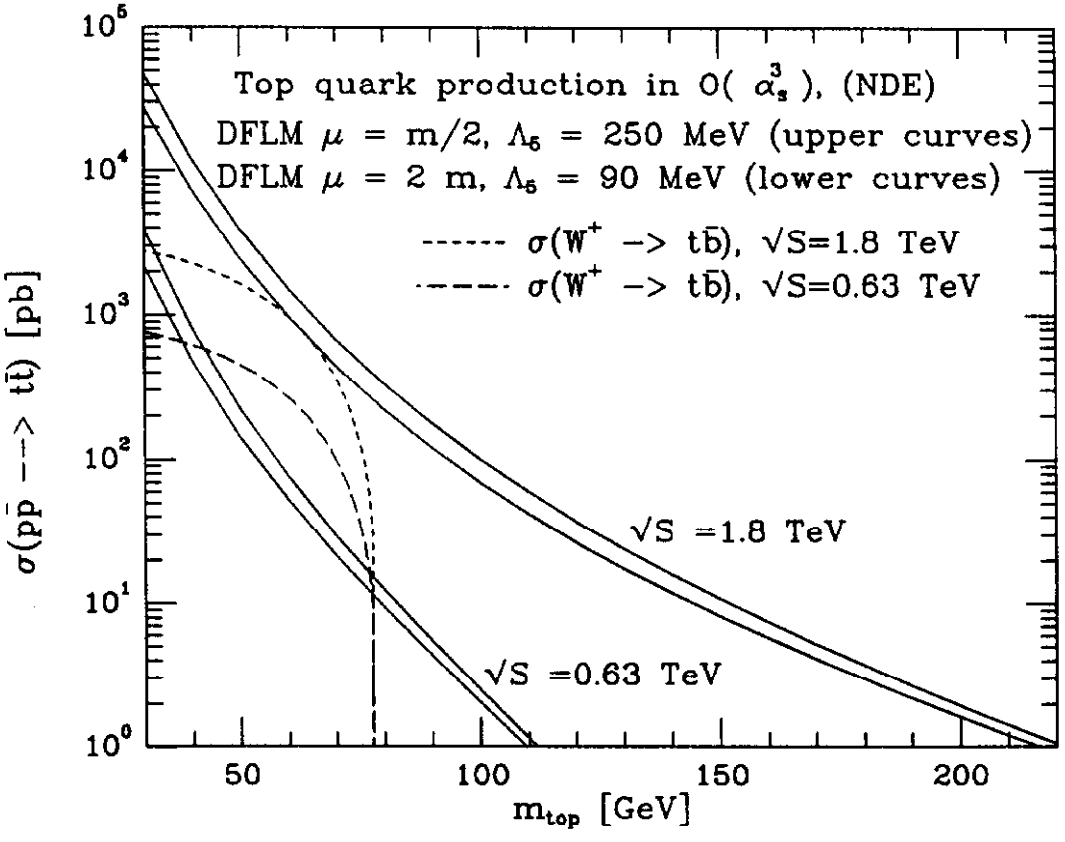

Figure 56: The cross section for top quark production at CERN and FNAL

tion, but the background is larger due to the process $p\bar{p} \rightarrow W$+jets. This background may become less severe with increasing top mass as the jets present in top decay become more energetic.

The current lower limit on the mass of the top quark is 89 GeV [66]. If the efficiency of extracting the signal from the data does not change with the mass of the top quark, we can expect to improve the limit by an additional 40 GeV above the present limit, by increasing the luminosity accumulated at the Tevatron by a factor of 10. Note however that the efficiency of the e+ multi-jets channels will increase for a heavier top quark. As the mass of the top quark increases the b quark jets occurring in its decay will be recognised in the detector as fully-fledged jets. This occurs with no extra price in coupling constants. The background due to normal W+jets production, discussed in the previous lecture, is suppressed by a power of

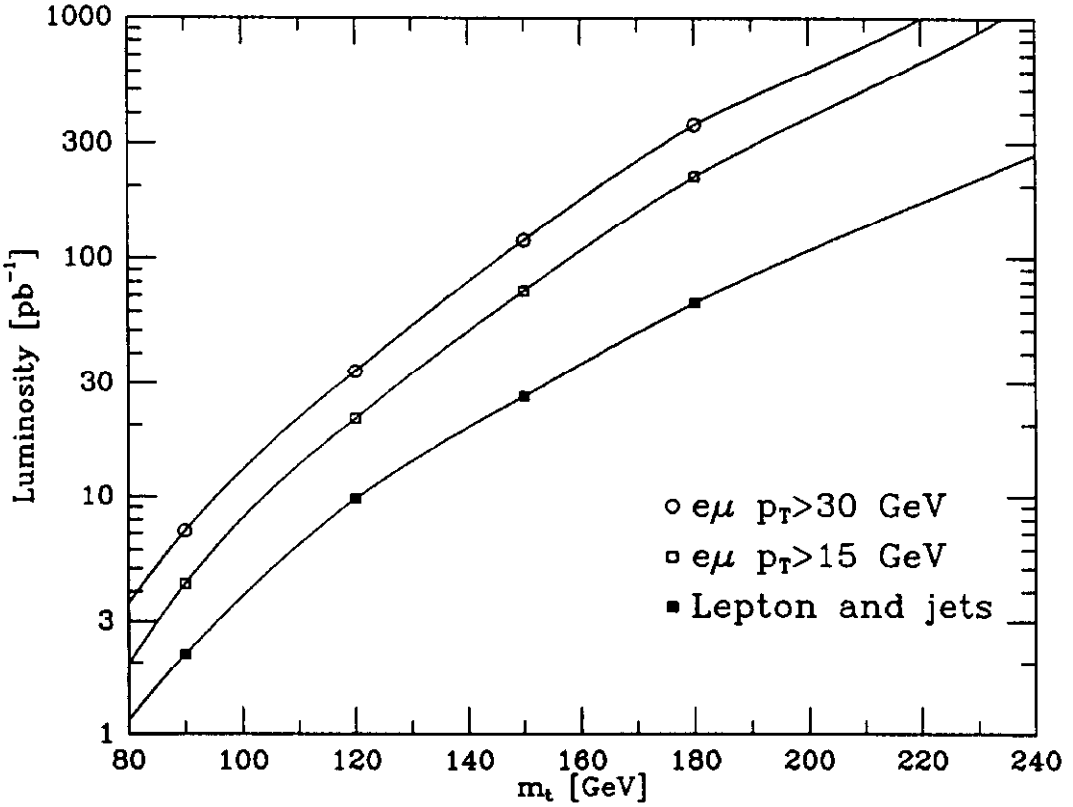

Figure 57: Required luminosity to discover top at 1.8 TeV in various decay modes

α_S for each extra jet. It will become less important in the channel with an electron and/or three and four jets. The results of a detailed study of the prospects for top quark discovery are shown in Fig.(57), taken from ref. [100]. The limits are based on the expected performance of the D0 and upgraded CDF detectors.

7.6 Heavy quark in jets

Another question of experimental interest is the frequency with which heavy quarks are found amongst the decay products of a light quark or gluon jet. Since hadrons containing heavy quarks have appreciable semi-leptonic branching ratios such events will often lead to final states with leptons in jets. If we wish to use lepton plus jet events as a signature for new physics we must understand the background due to heavy quark production and decay.

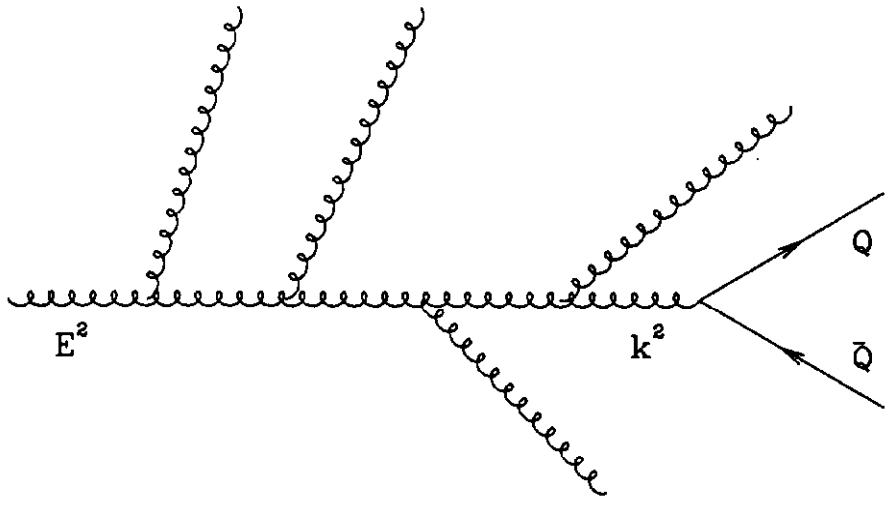

Figure 58: Heavy quark production in jets

This issue is logically unrelated to the total heavy quark cross section. As discussed above, the total cross section is dominated by events with a small transverse energy of the order of the quark mass. Jet events inhabit a different region of phase space since they contain a cluster of transverse energy $E_T \gg m_c, m_b$. This latter kinematic region gives a small contribution to the total heavy quark cross section. A gluon decaying into a heavy quark pair must have a virtuality $k^2 > 4m^2$ so perturbative methods should be applicable for a sufficiently heavy quark. The number of $Q\bar{Q}$ pairs per gluon jet is calculable [101] using diagrams such as the one shown in Fig.(58). The calculation has two parts. First one has to calculate $n_g(E^2, k^2)$, the number of gluons of off-shellness k^2 inside the original gluon with off-shellness E^2. Secondly, one needs the transition probability of a gluon with off-shellness k^2 to decay to a pair of heavy quarks.

The number of gluons of mass squared k^2 inside a jet of virtuality E^2 is given by [101],

$$n_g(E^2,k^2) = \left[\frac{\ln(E^2/\Lambda^2)}{\ln(k^2/\Lambda^2)}\right]^a \frac{\exp\sqrt{[(2N/\pi b)\ln(E^2/\Lambda^2)]}}{\exp\sqrt{[(2N/\pi b)\ln(k^2/\Lambda^2)]}}, \tag{7.36}$$

where

$$a = -\frac{1}{4}\left[1 + \frac{2n_f}{3\pi b}(1 - \frac{(N^2-1)}{2N^2})\right] \tag{7.37}$$

and b is the first order coefficient in the expansion of the β function, Eq.(7.20). The correct calculation of the growth of the gluon multiplicity Eq.(7.36) requires the imposition of the angular ordering constraint which takes into account the coherence of the emitted soft gluons [102] as discussed in the second lecture.

Define $R_{Q\overline{Q}}$ to be the number of $Q\overline{Q}$ pairs per gluon jet. Ignoring for the moment gluon branching calculated above, we obtain

$$R_{Q\overline{Q}} = \frac{1}{4\pi}\int_{4m^2}^{E^2}\frac{dk^2}{k^2}\alpha_S(k^2)\int_{z_-}^{z_+} dz\left[z^2 + (1-z)^2 + \frac{2m^2}{k^2}\right] \tag{7.38}$$

where the integration limits are given by $z_\pm = (1\pm\beta)/2$ with $\beta = \sqrt{(1-4m^2/k^2)}$. The term $(z^2+(1-z)^2)/2$ is recognisable as P^0_{qg}, the Altarelli-Parisi branching probability for massless quarks. Integrating over the longitudinal momentum fraction z we obtain,

$$R_{Q\overline{Q}} = \frac{1}{6\pi}\int_{4m^2}^{E^2}\frac{dk^2}{k^2}\alpha_S(k^2)\left[1 + \frac{2m^2}{k^2}\right]\sqrt{1 - \frac{4m^2}{k^2}}. \tag{7.39}$$

The final result including gluon branching for the number of heavy quark pairs per gluon jet is,

$$R_{Q\overline{Q}} = \frac{1}{6\pi}\int_{4m^2}^{E^2}\frac{dk^2}{k^2}\alpha_S(k^2)\left[1 + \frac{2m^2}{k^2}\right]\sqrt{1 - \frac{4m^2}{k^2}}\, n_g(E^2,k^2). \tag{7.40}$$

The predicted number of charm quark pairs per jet is plotted in Fig.(59) using a value of $\Lambda^{(3)} = 300$ MeV and three values of the charm quark mass. Also shown is the prediction for the number of bottom quarks per jet with $\Lambda^{(4)} = 260$ MeV. The data point shows the number of D^* per jet as measured by the UA1 collaboration [103] and by the CDF collaboration [104]. Note that these results depend on the values used for the branching ratios $(D^* \to D\pi)$ and $(D \to K\pi)$. CDF uses the values of the Mark III collaboration [105] whereas UA1 uses the values quoted by the Particle Data Group. In order compare these numbers with the $c\bar{c}$ pair rates, a model of the

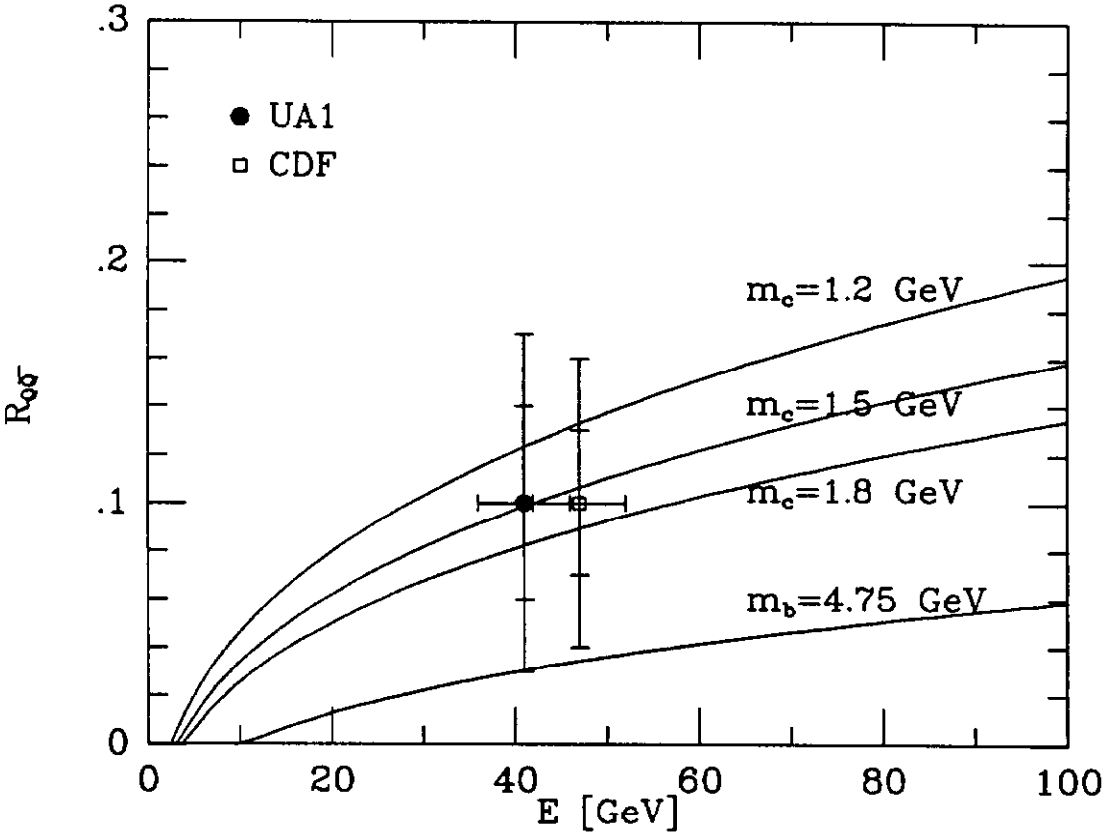

Figure 59: Heavy quarks in jets compared with UA1 and CDF data

relative rates of D and D^* production is also needed. For example, if all spin states are produced equally one would expect the charged D^* rate to be 75% of the total D production rate. The points in Fig. 59 need to be corrected for unobserved modes before they can be compared with the curves for the total $c\bar{c}$ pair rate.

References

1) J.D. Bjorken and S.D. Drell, 'Relativistic Quantum Fields', McGraw Hill, New York (1964).

2) C. Itzykson and J.B. Zuber, 'Quantum Field Theory', McGraw Hill, New York (1980).

3) F. Yndurain, 'Quantum Chromodynamics', Springer-Verlag (1983).

4) T. Muta, 'Foundations of Quantum Chromodynamics', World Scientific (1987).

5) G. Altarelli, *Phys. Rep.* **81** (1982) 1 .

6) A.H. Mueller, *Phys. Rep.* **73** (1981) 237 .

7) D.W. Duke and R.G. Roberts, *Phys. Rep.* **120** (1985) 275 .

8) E. Abers and B.W. Lee, *Phys. Rep.* **9** (1973) 1 .

9) L. Faddeev and V.N. Popov, *Phys. Lett.* **258** (1977) 377 .

10) R.K. Ellis, Proceedings of the 1987 Theoretical Advanced Study Institute in Elementary Particle Physics, edited by R. Slansky and G. West, (World Scientific).

11) G. t'Hooft and M.J.G. Veltman, Diagrammar, CERN Yellow Report 73-9, published in the proceedings of the summer school, 'Particle Interactions At Very High Energies, Part B', Louvain (1973).

12) J.C. Collins and W-K. Tung, *Nucl. Phys.* **B278** (1986) 934 .

13) F. Bloch and A. Nordsieck, *Phys. Rev.* **52** (1937) 54 .

14) T. Kinoshita, *J. Math. Phys.* **3** (1962) 650 ;
T.D. Lee and M. Nauenberg, *Phys. Rev.* **133B** (1964) 1549 .

15) S.G. Gorishny, A.L. Kataev and S.A. Larin, *Phys. Lett.* **212B** (1988) 238 .

16) R.N. Faustov *et al.*, Tata Institute preprint TIFR/TH/90-8 (1990);
S.G. Gorishny *et al.*, Tata Institute preprint TIFR/TH/90-9 (1990).

17) G. Grunberg, *Phys. Lett.* **95B** (1980) 70 .

18) P.M. Stevenson, *Nucl. Phys.* **B150** (1979) 357 .

19) G. D'Agostini, W. de Boer and G. Grindhammer, *Phys. Lett.* **B229** (1989) 160 .

20) G. Kramer, 'Theory of jets in electron - positron annihilation', Springer Tracts in Modern Physics, Berlin, (1984).

21) Z. Kunszt *et al.*, *Z* Physics at LEP1, CERN Yellow Report, 89-08 (1989), Vol. 1, page 373.

22) M.Z. Akrawy *et al.*, *Phys. Lett.* **235B** (1990) 389 .

23) B. Andersson *et al.*, *Phys. Rep.* **97** (1983) 33 .

24) Ya.L. Azimov *et al.*, *Phys. Lett.* **165B** (1985) 147 .

25) A. Bassetto *et al.*, *Nucl. Phys.* **B207** (1982) 189 .

26) Yu.L. Dokshitzer *et al.*, *Rev. Mod. Phys.* **60** (1988) 373 .

27) TPC Collaboration: H. Aihara *et al.*, *Phys. Rev.* **57** (1986) 945 .

28) B.R. Webber, *Ann. Rev. Nucl. Part. Sci.* **36** (1986) 253 .

29) SLAC-MIT collaboration: G. Miller et al., *Phys. Rev.* **D5** (1972) 528 .

30) BCDMS collaboration: A.C. Benvenuti et al., *Phys. Lett.* **223B** (1989) 485 .

31) R.P. Feynman, 'Photon Hadron Interactions', W.A. Benjamin, New York (1972).

32) G. Altarelli and G. Parisi, *Nucl. Phys.* **B126** (1977) 298 .

33) G. Curci, W. Furmanski and R. Petronzio, *Nucl. Phys.* **B175** (1980) 27 ; W. Furmanski and R. Petronzio, *Phys. Lett.* **97B** (1980) 437 .

34) EMC collaboration: J.J. Aubert et al., *Nucl. Phys.* **B259** (1985) 189 .

35) BCDMS collaboration: A.C. Benvenuti et al., *Phys. Lett.* **223B** (1989) 490 .

36) D.W. Duke and J.F. Owens, *Phys. Rev.* **D30** (1984) 49 .

37) A.D. Martin, R.G. Roberts and W.J. Stirling, *Phys. Rev.* **D37** (1988) 1161 , *Mod. Phys. Lett.* **A4** (1989) 1135 .

38) P.N. Harriman, A.D. Martin, R.G. Roberts and W.J. Stirling, preprint RAL-90-007 (1990), to be published in Physical Review D.

39) L.V. Gribov, E.M. Levin and M.G. Ryskin, *Phys. Rep.* **100** (1982) 1 .

40) J.C. Collins and D.E. Soper, *Ann. Rev. Nucl. Part. Sci.* **37** (1987) 383 .

41) R. Basu *et al.*, *Nucl. Phys.* **B244** (1984) 221 .

42) J. D. Jackson, 'Classical Electrodynamics', John Wiley (1962).

43) R. Doria, J. Frenkel and J.C. Taylor, *Nucl. Phys.* **B168** (1980) 93 .

44) S.D. Ellis, Z. Kunszt and D.E. Soper, *Phys. Rev. Lett.* **64** (1990) 2121 .

45) M. Mangano and S. Parke, FERMILAB–Pub–90/113–T and references therein.

46) F.A. Berends *et al.*, *Phys. Lett.* **103B** (1981) 124 .

47) R.K. Ellis, G. Marchesini and B.R. Webber, *Nucl. Phys.* **B286** (1987) 643 .

48) B. Combridge and C.J. Maxwell, *Nucl. Phys.* **B239** (1984) 429 .

49) B. Combridge and C.J. Maxwell, *Phys. Lett.* **151B** (1985) 299 ;
F. Halzen and P. Hoyer, *Phys. Lett.* **130B** (1983) 326 .

50) WA70 collaboration: M. Bonesini *et al.*, *Zeit. Phys.* **C38** (1988) 371 .

51) P. Aurenche *et al.*, *Nucl. Phys.* **B297** (1988) 661 .

52) J. Kubar-Andre and F.E. Paige, *Phys. Rev.* **D19** (1979) 221 ;
J. Kubar-Andre, M. Le Bellac, J.L. Meunier and G. Plaut, *Nucl. Phys.* **B175** (1980) 251 .

53) G. Altarelli, R.K. Ellis and G. Martinelli, *Nucl. Phys.* **B143** (1978) 521 ; *Nucl. Phys.* **B146** (1978) 544(e) ; *Nucl. Phys.* **B147** (1979) 461 .

54) E605 collaboration: C.N. Brown *et al.*, *Phys. Rev. Lett.* **63** (1989) 2637 .

55) I.R. Kenyon, *Rev. Mod. Phys.* **45** (1982) 1261 .

56) U. Amaldi *et al.*, *Phys. Rev.* **D36** (1987) 1385 ;
G. Costa *et al.*, *Nucl. Phys.* **B297** (1988) 24 ;
D. Haidt, preprint DESY 89/073 (1990).

57) UA2 collaboration: J. Alitti *et al.*, *Phys. Lett.* **241** (1990) 150 .

58) CDF collaboration: F.Abe *et al.*, preprint FERMILAB-PUB-90/162-E.

59) Mark II collaboration: G. Abrams *et al.*, *Phys. Rev. Lett.* **63** (1989) 2173 ;
ALEPH collaboration: D. Decamp *et al.*, *Phys. Lett.* **231B** (1989) 519 ; *ibid.* **235B** (1990) 399 ;
DELPHI collaboration: P. Aarnio *et al.*, *Phys. Lett.* **231B** (1990) 539 ;
L3 collaboration: B. Adeva *et al.*, *Phys. Lett.* **231B** (1989) 509 ; *ibid.* **237B** (1990) 136 ;
OPAL collaboration: M.Z. Akrawy *et al.*, *Phys. Lett.* **231B** (1989) 530 .

60) M. Peskin, Proceedings of the 17th SLAC summer institute on particle physics, SLAC-REPORT-361, p.71 (1989).

61) UA1 collaboration: C. Albajar *et al.*, *Zeit. Phys.* **C44** (1989) 15 .

62) UA2 collaboration: J. Alitti *et al.*, preprint CERN-EP/90-20 (1990).

63) CDF collaboration: F. Abe *et al.*, to be published in *Phys. Rev.* **D**.

64) T. Matsuura, S.C. van der Marck and W.L. van Neerven, *Phys. Lett.* **211B** (1988) 171 .

65) UA2 collaboration: R. Ansari *et al.*, *Phys. Lett.* **168B** (1987) 452 .

66) F. Abe *et al.*, *Phys. Rev. Lett.* **64** (1990) 147 ;
G. P. Yeh, FERMILAB-CONF-90/138-E, to be published in the proceedings of 'Les Rencontres de Physique de la Vallée d'Aoste', Editions Frontieres (1990), ed. M. Greco.

67) F. Halzen and K. Mursula, *Phys. Rev. Lett.* **51** (1983) 857 ;
K. Hikasa, *Phys. Rev.* **D29** (1984) 1939 .

68) CDF collaboration: F. Abe *et al.*, preprint FERMILAB-PUB-89/245-E (1990).

69) UA2 collaboration: R. Ansari *et al.*, *Phys. Lett.* **B186** (1987) 440 ; erratum *Phys. Lett.* **B190** (1987) 238 .

70) CDF collaboration: P. Hurst, Proceedings of the 8th Topical Workshop on Proton-Antiproton Collider Physics, Castiglione della Pescaia, Italy (1989).

71) P. Arnold and M. H. Reno, *Nucl. Phys.* **B319** (1989) 37 , *ibid.* **330** (1990) 284 (e);
R. Gonsalves, J. Pawlowski and C.-F. Wai, *Phys. Rev.* **D40** (1989) 2245 .

72) CDF collaboration: presented by T. Watts at the 15th APS Division of Particles and Fields General Meeting, Houston, January 1990.

73) UA2 collaboration: J. Ansari *et al.*, *Phys. Lett.* **215B** (1988) 175 .

74) P. Arnold, private communication.

75) F.A. Berends, W.T. Giele, H. Kuijf, R. Kleiss and W.J. Stirling, *Phys. Lett.* **224B** (1989) 237 .

76) F.A. Berends, W.T. Giele, H. Kuijf and B. Tausk, University of Leiden preprint (1990).

77) S. Glashow and E. Jenkins, *Phys. Lett.* **196B** (1987) 233 .

78) S. Glashow and S. Weinberg, *Phys. Rev.* **D15** (1977) 1958 .

79) H. Schröder, *Rep. Prog. Phys.* **52** (1989) 765 .

80) M. Gluck, J.F. Owens and E. Reya, *Phys. Rev.* **D17** (1978) 2324 ;
B. Combridge, *Nucl. Phys.* **151** (1979) 429 .

81) R.K. Ellis, *Strong Interactions and Gauge Theories,* edited by J. Tran Thanh Van, Editions Frontières, Gif-sur-Yvette, 1986, p. 339;
R.K. Ellis, Proceedings of the 17th SLAC summer institute on particle physics, SLAC-REPORT-361, p.45 (1989).

82) J.C. Collins, D.E. Soper and G. Sterman, *Nucl. Phys.* **B263** (1986) 37

83) S.J. Brodsky, J.C. Collins, S.D. Ellis, J.F. Gunion and A.H. Mueller, in *Proc. 1984 Summer Study on the Design and Utilization of the Superconducting Super Collider*, Fermilab, Batavia, Illinois, 1984, p. 227;
S.J. Brodsky, J.F. Gunion and D.E. Soper, *Phys. Rev.* **D36** (1987) 2710 .

84) P. Nason, S. Dawson and R.K. Ellis, *Nucl. Phys.* **B303** (1988) 607 .

85) W. Beenakker *et al.*, *Phys. Rev.* **D40** (1989) 54 .

86) G. Altarelli *et al.*, *Nucl. Phys.* **B308** (1988) 724 .

87) U. Gasparini, Proceedings of the XXIV Conference on High Energy Physics, Munich, August 1988.

88) R.K. Ellis and P. Nason, *Nucl. Phys.* **B312** (1989) 551 .

89) J.C. Anjos *et al.*, *Phys. Rev. Lett.* **62** (1989) 513 .

90) R. Forty, Proceedings of the XXIV Conference on High Energy Physics, Munich, August 1988.

91) S.P.K. Tavernier, *Rep. Prog. Phys.* **50** (1987) 1439 .

92) P. Nason, Proceedings of the XXIV Conference on High Energy Physics, Munich, August 1988.

93) BCF collaboration: L. Cifarelli *et al.*, *Nucl. Phys.* **Proc. Suppl. 1B** (1988) 55 .

94) C. Albajar *et al.*, *Zeit. Phys.* **C37** (1988) 505 ;
C. Albajar *et al.*, *Phys. Lett.* **B213** (1988) 405 .

95) WA78 collaboration: M.G. Catanesi *et al.*, *Phys. Lett.* **231B** (1989) 328 , *ibid.* **202B** (1988) 453 .

96) NA10 collaboration: P. Bordalo *et al.*, *Zeit. Phys.* **C39** (1988) 7 .

97) P. Nason, S. Dawson and R.K. Ellis, *Nucl. Phys.* **B327** (1990) 49 , *ibid.* **B335** (1990) 260 (e).

98) C. Bouchiat, J. Iliopoulos and P. Meyer, *Phys. Lett.* **38B** (1972) 519 ;
D.J. Gross and R. Jackiw, *Phys. Rev.* **D6** (1972) 477 .

99) S.L. Wu, Proceedings of the Lepton Photon Symposium, Hamburg, August 1987;
W. Bartel *et al.*, *Phys. Lett.* **146B** (1984) 437 .

100) H.E. Fisk and J. Slaughter in 'Physics at Fermilab in the 1990's', eds. D. Green and H. Lubatti, World Scientific, 1990.

101) A.H. Mueller and P. Nason, *Phys. Lett.* **157B** (1985) 226 .

102) A. Bassetto, M. Ciafaloni and G. Marchesini, *Phys. Rep.* **100** (1983) 201 and references therein.

103) M. Ikeda, Proceedings of the 8th topical workshop on proton antiproton collider physics, Castiglione della Pescaia (1989).

104) F. Abe *et al.*, *Phys. Rev. Lett.* **64** (1990) 348 .

105) J. Adler *et al.*, *Phys. Lett.* **208B** (1988) 152 ;
J. Adler *et al.*, *Phys. Rev. Lett.* **60** (1988) 89 .